DISS. ETH NO. 26793

The microphysics and dynamics of mixed-phase clouds in the Swiss Alps: insights from balloon-borne and remote sensing observations

A thesis submitted to attain the degree of

DOCTOR OF SCIENCES of ETH ZURICH

(Dr. sc. ETH Zurich)

presented by
FABIOLA RAMELLI
MSc in Environmental Sciences, ETH Zurich
born on 11 October 1991
citizen of Switzerland

accepted on the recommendation of
Prof. Dr. Ulrike Lohmann, examiner
Dr. Jan Henneberger, co-examiner
Prof. Dr. Susanne Crewell, co-examiner

2020

Abstract

Mountains can trigger the formation of orographic clouds or modify the structure of incoming cloud systems and thereby account for a large fraction of the Earth's annual precipitation. During winter, most of the precipitation-forming clouds are mixed-phase clouds (MPCs), which consist of a mixture of supercooled cloud droplets and ice crystals. Although the coexistence of liquid and ice is thermodynamically unstable, persistent MPCs have frequently been observed in mountain regions, where the local topography produces sufficiently large updrafts to provide a continuous source of condensate. Despite significant advances in the fundamental understanding of MPCs and orographic precipitation over the past decades, large uncertainties remain regarding ice initiation, the partitioning between the liquid and ice phase and the glaciation time in MPCs. This limits the ability to obtain accurate forecasts of precipitation formation and amounts in complex terrain. Innovative measurement strategies are required to improve our understanding of the numerous microphysical and dynamical processes in orographic MPCs and their convoluted interactions, which govern orographic precipitation.

The aim of this thesis is to improve the process understanding of orographic MPCs and precipitation through a multi-instrumental approach by combining observations from an extensive set of in situ and remote sensing instrumentation. Since the ability of aircrafts to fly in cloudy conditions in complex terrain is limited (e.g., in winding and narrow valleys) and cloud observations at mountain-tops are influenced by surface processes, a new measurement platform on a tethered balloon system (HoloBalloon) was developed to study boundary layer clouds in complex terrain. The major component of the measurement platform is a newly developed HOLographic Imager for Microscopic Objects (HOLIMO 3B), which was designed for balloon-borne measurements. HOLIMO 3B uses digital in-line holography to image an ensemble of cloud particles in the size range from small cloud droplets to precipitation-sized particles in a three-dimensional sample volume. Based on two-dimensional images, information about the phase-resolved particle size distribution and particle shape can be obtained. The velocity-independent sample volume of HOLIMO 3B makes it particularly well suited for balloon-borne applications, which have to deal with fluctuations in wind speed and direction. Additionally, the measurement platform is equipped with an optical particle counter, a 3D ultrasonic anemometer, and a temperature, a humidity and a pressure sensor.

The HoloBalloon platform was successfully deployed in different environments and atmospheric conditions. In winter 2018, the HoloBalloon platform demonstrated its feasibility by obtaining vertical profiles of microphysical and meteorological cloud properties up to 700 m above the surface in low stratus clouds over the Swiss Plateau. In winter 2019, the HoloBalloon platform was deployed in orographic clouds within the framework of the Role of Aerosols and CLouds

Enhanced by Topography on Snow (RACLETS) campaign, which took place in the Swiss Alps in the region around Davos.

A wide variety of orographic effects can enhance precipitation over complex terrain and influence its spatial distribution along the mountain barrier. In the present thesis, the complex interplay between orography, dynamics, microphysics and precipitation is explored on the basis of several case studies of the RACLETS campaign. The role of low-level blocking and shear-induced turbulence on the cloud microphysics and precipitation formation was investigated in an inner-Alpine valley. We suggest that aggregation, needle growth and secondary ice production occurred within the turbulent shear layer, which enhanced ice growth and precipitation formation. The amount of precipitation was determined by the strength of the cross-barrier flow and of the low-level blocking, as precipitation was only observed at the ground when the blocking was weakest and the altitude of the cloud base and shear layer were lowest. Additionally, a persistent low-level liquid cloud was observed by the HoloBalloon platform, when the low-level flow was forced to rise over a small-scale topographic feature in the mountain valley. This shallow low-level cloud did not generate significant precipitation by itself, but was found to "feed" on precipitation particles that formed at higher altitudes (i.e., in the seeder region of the cloud) and to produce conditions favorable for secondary ice production processes. Seeder regions were observed in connection with cloud top generating cells, within which enhanced ice formation and growth occurred. In the present thesis, we propose different mechanisms that potentially increase ice formation and growth within generating cells (convective overshooting, radiative cooling, droplet shattering) by considering the ground-based ice nucleating particle concentration and the ice crystal number concentration measured near cloud base. We found that increased ice formation and growth within the seeder region can induce the full glaciation of a MPC and suggest that secondary ice production may have been partly responsible for the elevated ice crystal number concentrations that have been previously observed in feeder clouds at mountain-top observatories.

The synergy of aerosol, cloud, dynamics and precipitation observations can improve our understanding of the microphysical pathways of precipitation formation in orographic MPC. These microphysical processes (e.g., secondary ice production, glaciation of MPC) and the dynamical response of the flow to the orography need to be represented accurately in atmospheric models in order to improve the reliability of precipitation forecasts in complex terrain.

Zusammenfassung

Gebirge können zur Bildung von orographischen Wolken führen sowie die Struktur von ankommenden Wolkensystemen beeinflussen und tragen damit zu einem Grossteil des jährlichen Niederschlages bei. Der meiste Niederschlag im Winter entsteht in sogenannten Mischwolken (MW), welche aus einer Mischung aus unterkühlten Wolkentröpfchen und Eiskristallen bestehen. Obwohl die Koexistenz von Flüssigwasser und Eis thermodynamisch instabil ist, beobachtet man langlebige MW häufig in Bergregionen, wo die lokale Topographie genügend hohe Aufwindgeschwindigkeiten produzieren kann um eine kontinuierliche Flüssigwasserzufuhr zu gewährleisten. Trotz bedeutender Fortschritte im Verständnis von MW und orographischem Niederschlag gibt es immer noch grosse Unsicherheiten bezüglich der Eisbildung, dem Anteil von unterkühlten Wolkentröpfchen sowie der Vereisung von MW. Innovative Messstrategien sind erforderlich für ein besseres Verständnis von den zahlreichen mikrophysikalischen und dynamischen Prozessen in orographischen MW sowie deren Interaktionen und damit einer verbesserten Niederschlagsprognose im Gebirge.

Das Ziel dieser Doktorarbeit ist es das Prozessverständnis von orographischen MW und Niederschlag mit Hilfe eines multisensorischen Ansatzes, der in situ- und Fernerkundungsmessungen kombiniert, zu verbessern. Angesichts der begrenzten Fähigkeit von Flugzeugmessungen in Wolken in komplexem Gebirge (z.B., in gewundenen und engen Tälern) und dem Einfluss von Bodenprozessen auf Wolkenmessungen (z.B. auf Bergstationen), wurde eine neue Messplattform auf einem Fesselballon entwickelt (HoloBalloon), um Grenzschichtwolken im komplexen Gelände zu untersuchen. Der Hauptbestandteil der Messplattform ist ein neu entwickeltes holographisches Messinstrument (HOLIMO 3B), welches für ballongestützte Anwendungen konzipiert wurde. HOLIMO 3B verwendet digitale in-line Holographie um ein Ensemble von Wolkenpartikeln bestehend aus kleinen Wolkentröpfchen bis zu grossen Niederschlagspartikeln in einem dreidimensionalen Volumen zu messen. Anhand von zweidimensionalen Bildern können Informationen zur phasenaufgelösten Partikelgrössenverteilung sowie zur Partikelform erhalten werden. Das Messvolumen von HOLIMO 3B ist unabhängig von der Anströmungsgeschwindigkeit und eignet sich daher sehr gut für ballongestützte Anwendungen, da auf einem Ballon Fluktuationen in der Windgeschwindigkeit und Windrichtung auftreten. Zusätzlich ist die Messplattform mit einem optischen Partikelzähler, einem 3D Ultraschallanemometer sowie mit Temperatur-, Feuchte- und Drucksensoren ausgestattet.

Die HoloBalloon Plattform wurde erfolgreich in verschiedenen Umgebungen und atmosphärischen Bedingungen eingesetzt. Im Winter 2018 hat die HoloBalloon Plattform erstmals ihre Funktionsfähigkeit in tiefen Stratuswolken über dem Schweizer Mittelland unter Beweis gestellt, indem Vertikalprofile von mikrophysikalischen und meteorologischen Wolkeneigenschaften bis

auf eine Höhe von 700 m über Boden gemessen wurden. Im Winter 2019 wurde die HoloBalloon Plattform in orographischen Wolken im Rahmen der RACLETS Messkampagne eingesetzt, welche in den Schweizer Alpen in der Region um Davos stattfand.
Eine Vielzahl an orographischen Prozessen können die Niederschlagsbildung in komplexem Gebirge verstärken und die räumliche Niederschlagsverteilung entlang der Gebirgskette beeinflussen. Das komplexe Zusammenspiel zwischen Orographie, Dynamik, Mikrophysik und Niederschlagsbildung wurde in dieser Doktorarbeit anhand von verschiedenen Fallstudien während der RACLETS Kampagne untersucht. Die Auswirkungen von blockierten Strömungen und Turbulenzen auf die Mikrophysik und Niederschlagsbildung wurde in einem inneralpinen Tal erforscht. Das Eiswachstum war innerhalb der turbulenten Scherschicht verstärkt aufgrund vermehrter Aggregation, Nadelwachstum und der Bildung von Sekundäreis. Die Niederschlagsmenge hing von der Stärke der Höhenströmung und der Gegenströmung in Bodennähe ab, da Niederschlag nur am Boden beobachtet wurde, wenn die Gegenströmung am schwächsten war und die Höhe der Wolkenbasis und der Scherschicht am tiefsten waren. Zudem wurde mit Hilfe der HoloBalloon Plattform eine langlebige Flüssigwasserschicht in Bodennähe beobachtet, welche durch das Anheben der bodennahen Strömung über eine kleinräumige topographische Struktur gebildet wurde. Diese tiefe Wolke konnte selbst keine erheblichen Niederschlagsmengen produzieren, konnte allerdings Wassertröpfchen zum Anfrieren an Niederschlagspartikeln liefern (Feeder-Region), welche in der höher gelegenen Wolkenschicht (Seeder-Region) gebildet wurden, sowie geeignete Bedingungen für die Bildung von Sekundäreis schaffen. Seeder-Regionen treten häufig in Verbindung mit eisbildenden Zellen (generating cells) in der Nähe der Wolkenoberkante auf, in welchen vermehrte Eisbildung und verstärktes Eiswachstum beobachtet wird. In dieser Doktorarbeit wurden verschiedene Prozesse, welche die Eisbildung und das Eiswachstum in den eisbildenden Zellen verstärken können (überschiessende Konvektion, Strahlungsabkühlung, Bildung von Sekundäreis durch Zersplitterung von Tröpfchen), mit Hilfe der Analyse von Eiskeimkonzentrationen und den Eiskristallkonzentrationen in der Nähe der Wolkenuntergrenze untersucht. Unsere Beobachtungen zeigen, dass verstärkte Eisbildung und Eiswachstum innerhalb der Seeder-Region zur Vereisung der MW führen kann und dass Sekundäreisprozesse möglicherweise zu den erhöhten Eiskristallkonzentrationen, welche regelmässig auf Bergstationen gemessen werden, beitragen.
Die Kombination von Aerosol-, Wolken-, Dynamik- und Niederschlagsmessungen helfen unser Verständnis von den niederschlagsbildenden Prozessen in orographischen MW zu verbessern. Diese mikrophysikalischen Prozesse (z.B. Bildung von Sekundäreis, Vereisung der MW) und der Einfluss von Gebirge auf die Strömung müssen möglichst genau in den atmosphärischen Modellen abgebildet werden, um die Niederschlagsprognosen im komplexen Gelände zu verbessern.

Contents

Chapter 1

Introduction

The close connection between precipitation and mountains dates back to ancient times. From far away, the ancient Greeks could see how towering mountains were triggering the formation of clouds or diverting incoming cloud systems, influencing the distribution of precipitation. One of the pioneers exploring the influence of mountains on weather and climate was Aristotle, who writes in *Meteorologica*:

> *For mountains and high places act like a thick sponge overhanging the earth and make the water drip through and run together in small quantities in many places. For they receive the great volume of rain water that falls ... and they cool the vapor as it rises and condense it again to water.*
>
> (Aristotle — 340 B.C.)

Nowadays, it is well known that mountains account for a large fraction of the annual precipitation, form an important water storage (e.g., glaciers) and represent a major fresh water supply for many rivers (e.g., Roe, 2005; Smith, 2019). While a solid understanding of orographic precipitation has been established over the last decades, many mechanisms responsible for orographic precipitation remain unresolved. In particular, the complex interactions between numerous processes spanning over a wide range of scales (e.g., dynamics, thermodynamics, microphysics, orography), make quantitative precipitation forecasting in complex terrain challenging. The ice phase was found to play a crucial role for precipitation formation, since more than 90 % of the precipitation in mid-latitudes originates from ice containing clouds (e.g., Mülmenstädt et al., 2015; Field and Heymsfield, 2015).

In addition, clouds play an important role for regulating the Earth's energy budget by reflecting solar shortwave radiation back into space (cooling) and by absorbing and re-emitting terrestrial longwave radiation (warming) (e.g., Fu and Liou, 1993; Liou, 2002). It depends on the cloud type and on the altitude, whether the cooling or warming effect is dominating. High, thin cirrus clouds have a warming effect on the climate system, whereas the cooling effect usually dominates for thick low- and mid-level clouds. Furthermore, the radiative impact of clouds strongly depends on the partitioning of the liquid and ice phase, as the radiative properties of cloud droplets and ice crystals differ significantly (e.g., Sun and Shine, 1994; Matus and L'Ecuyer,

2017). Ice clouds are optically thinner, due to the smaller refractive index of ice crystals and the larger particle size compared to liquid cloud droplets. Thus, the reflectivity of a pure water cloud can be 2 - 4 times larger than that of a pure ice cloud (Sun and Shine, 1994).
The warming climate adds an extra layer of complexity to the system. One of the largest sources of uncertainty in climate models is how clouds, or more specifically, the radiative impact of clouds and precipitation formation change in a warming climate (Boucher et al., 2013). Both factors strongly depend of the phase partitioning between the liquid and ice phase (e.g., Boucher et al., 2013). As temperature increases in a warming climate, a shift from the ice to the liquid phase could increase the opacity of clouds, resulting in a net cooling effect (e.g. Tan et al., 2016). On the other hand, precipitation is expected to intensify in a warming climate, increasing the risks of extreme precipitation events such as flash floods and landslides (e.g., Donat et al., 2016). However, these feedback mechanisms are highly uncertain and require further research. In particular, a comprehensive understanding of clouds and their phase partitioning in the present-day climate is essential to make projections on how the clouds and precipitation will change in a warming climate. The present thesis takes a step towards enhancing our understanding about clouds, focusing on the Alpine environment, which plays an important role in the hydrological cycle and is particularly vulnerable to changes in a warming climate.

1.1 The Swiss climate and typical weather conditions in the Alps

The Swiss climate is characterized by a complex microclimate, which is strongly influenced by the Alps as well as by the Atlantic Ocean. The predominant large-scale flow is from western/northwestern direction and thus brings moist ocean air towards Switzerland. With an average height of 3000 - 4000 m a.s.l., the Alps represent a barrier for incoming weather systems. If the moist large-scale flow encounters the Alps, the air mass is forced to ascend over the mountain barrier, which leads to adiabatic cooling and eventually to condensation of water vapor and thus to the formation of orographic clouds and precipitation. Several mechanisms have been proposed how the interplay between orography, dynamics and microphysics can enhance precipitation over complex terrain (see Section 1.3). Moreover, the Alps can alter and reorganize incoming weather systems and thus influence precipitation pattern.
In addition to their prominent role as a barrier for incoming weather systems, the Alps can also influence other climate regions such as the Swiss Plateau, which is bound by the Swiss Alps in the south and by the Jura mountains in the northwest. The Swiss Plateau is often covered by fog and low stratus clouds during the autumn and winter months (e.g., Bendix, 2002; Scherrer and Appenzeller, 2014). This local effect can be seen in the satellite picture in Figure 1.1, where the Swiss Plateau was completely covered by low stratus clouds, whereas other parts of Central Europe were practically cloudless. Most commonly, fog forms by radiative cooling along rivers and lakes during high pressure situations in the winter half year (e.g., Roach et al., 1976; Sampurno Bruijnzeel et al., 2006). Additionally, cold air can flow from the Alpine valleys and the Jura towards the Swiss Plateau, where the cold air can accumulate and form a cold air pool. If the air is sufficiently moist, further cooling of the air by emission of longwave radiation can cause

Figure 1.1: Satellite picture over Central Europe from 30 December 2016 taken by the Suomi NPP/VIIRS (taken from NASA Worldview), showing the presence of a low-level stratus cloud over the Swiss Plateau and the snow-capped Alps.

condensation and the formation of ground fog. Ground fog is often lifted up to higher altitudes due to surface heat fluxes, forming a continuous layer of low stratus clouds (often referred to as 'high fog' in German). Furthermore, low stratus clouds can form over the Swiss Plateau in connection with a Bise situation, when cold air from easterly to north-easterly direction is pushed under warm air (see also Chapter 2). In autumn and winter, the solar radiation absorbed by fog and low stratus clouds is often too small to dissipate the cloud layer. Thus, ground fog and stratus clouds can persist for several days, until a change in the synoptic weather pattern occurs.

Reliable forecasts of fog and low status clouds are particularly important for land transportation, aviation and photovoltaic energy production. However, current numerical weather prediction models have major issues in capturing the underlying physical processes and thus in predicting the formation and dissipation of fog and low stratus clouds. In the following, we will discuss the liquid-, mixed- and ice-phase processes in clouds in more detail.

1.2 Cloud microphysics

Clouds can consist of liquid cloud droplets (warm clouds), ice crystals (ice clouds) or a mixture of both (mixed-phase clouds). The cloud phase is strongly determined by the temperature and the physical processes. Pure liquid clouds occur at temperatures above 0 °C. Liquid cloud droplets can be supercooled down to a temperature of around -38 °C. Below -38 °C, supercooled cloud droplets freeze homogeneously (i.e., without the need of an ice nucleating particle). In the temperature range between 0 °C and -38 °C, mixed-phase clouds (MPCs) can exist (e.g., Pinto et al., 2001; Shupe et al., 2006). The coexistence of the ice and liquid phase is thermodynami-

cally unstable due to the lower saturation vapor pressure over ice compared to over liquid. In the following, we discuss the microphysical processes and interactions that determine the partitioning between the liquid and ice phase in MPCs.

Cloud droplets form through the activation of aerosol particles that can serve as cloud condensation nuclei (CCN). The CCN concentration depends on the ambient supersaturation and is generally higher over land (10^2 - $10^4\,\mathrm{cm}^{-3}$) than over ocean (10^1 - $10^3\,\mathrm{cm}^{-3}$) (Lohmann et al., 2016b). Cloud droplets grow initially by diffusion and condensation of water vapor. Condensational growth is too slow to be able to produce large precipitation-sized particles within 20 - 30 minutes. Thus, additional microphysical processes must be active that can produce large precipitation-sized particles more efficiently. The dominant precipitation formation process in warm clouds is growth of hydrometeors by collision-coalescence (Rogers and Yau, 1989), which involves the collision and subsequent coalescence of multiple cloud droplets. Collision-coalescence is initiated upon broadening of the cloud droplet size distribution, which can be achieved either by the presence of turbulence or giant CCN (Lohmann et al., 2016b).

Ice formation in MPCs occurs heterogeneously; i.e., it involves the presence of ice nucleating particles (INPs) (e.g., DeMott et al., 2010; Hoose and Möhler, 2012; Murray et al., 2012; Boose et al., 2016). INPs are less abundant in the atmosphere compared to CCN. INP concentrations are strongly temperature dependent and usually range between 0.1 and $10\,\mathrm{L}^{-1}$. Solid insoluble particles with a large surface area (e.g., mineral dust, biological particles) are the most common INPs (Kanji et al., 2017). Heterogeneous ice nucleation can occur by different nucleation pathways: (1) freezing can be initiated from a cloud droplet with an immersed INP (immersion freezing), (2) freezing can occur by condensation of water that subsequently freezes on an INP (condensation freezing), (3) freezing can be initiated upon collision of an INP with a supercooled cloud droplet (contact freezing) or (4) ice nucleation can occur by direct deposition of water vapor on an INP (deposition nucleation). More recent studies have proposed that freezing can be initiated within the pores of INPs (pore condensation and freezing), where liquid water condensation can occur below water saturation (Marcolli, 2014; David et al., 2019b). Moreover, ice crystals can originate from external sources such as from surface-based processes (e.g., blowing snow; Geerts et al., 2015; Beck et al., 2018 and hoar frost; Lloyd et al., 2015) or from aloft (seeder-feeder mechanism).

Newly formed ice crystals can grow by vapor deposition to a size of many tens of micrometers within a few minutes (Lohmann et al., 2016b). In contrast to condensational growth of cloud droplets, diffusional growth of ice crystals is more efficient in producing large precipitation-sized particles because higher supersaturations with respect to ice are reached. The ice crystal habit is strongly determined by the temperature of the environment (Magono and Lee, 1966; Bailey and Hallett, 2009). Plate-like ice habits dominate in the temperature range between 0 °C and -3 °C and between -10 °C and -22 °C. On the other hand, columnar ice crystals are the predominant ice habit at temperatures between -3 °C and -10 °C as well as at temperatures below -22 °C. Thus, the ice crystal habit can provide information about the growth history of ice particles and thus help to understand the microphysical processes active within clouds.

Multiple ice processes can occur in MPCs, which can enhance the growth of existing ice crystals or promote the formation of new ice crystals (see Figure 1.2). If the vapor pressure lies between

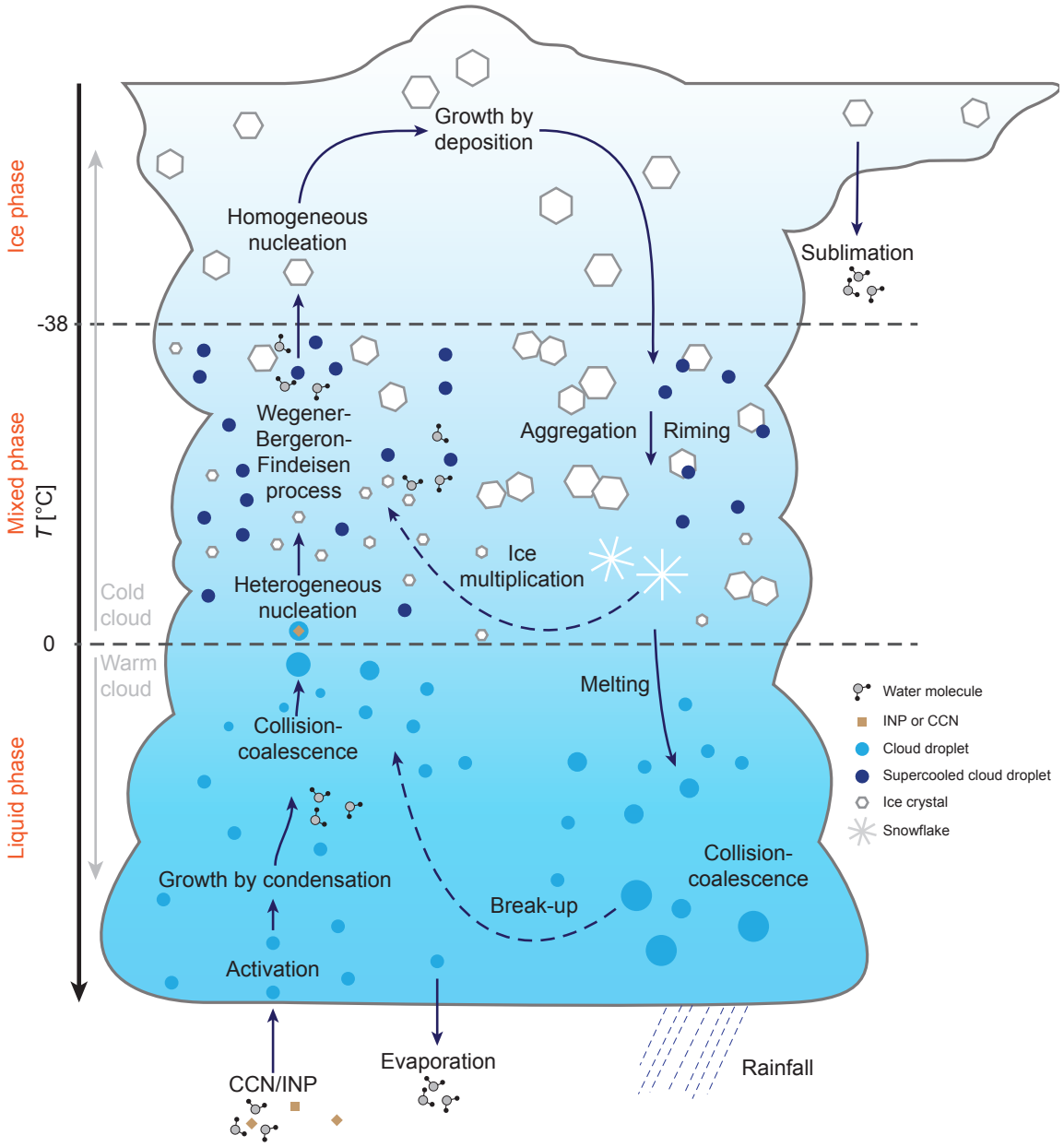

Figure 1.2: Microphysical processes occurring in a convective cloud including warm-, mixed- and ice-phase processes. Figure taken from Lohmann et al. (2016b).

ice and water saturation, then ice crystals grow rapidly at the expense of the surrounding cloud droplets due the lower saturation vapor pressure over ice (Korolev, 2007). This process is known as the Wegener-Bergeron-Findeisen (WBF) process (Wegener, 1911; Bergeron, 1935; Findeisen, 1938). The WBF process can lead to rapid glaciation and thus limits the lifetime of MPCs. For example, Korolev and Isaac (2003) showed that the WBF process can lead to glaciation within a few minutes or tens of minutes depending on the ice crystal size distribution, liquid water content, updraft velocity and temperature. Additionally, similarly as growth by collision-coalescence, multiple ice crystals can collide and clump together leading to the formation of aggregated snowflakes (aggregation). Aggregation is known to be most efficient at temperatures higher than -10 °C because of the presence of a thicker quasi-liquid layer, which enhances the stickiness of the ice particles (Lohmann et al., 2016b). Ice crystals can also collide with super-

cooled cloud droplets, which freeze upon contact leading to the formation of graupel (riming). The efficiency of riming is known to strongly depend on the cloud droplet size distribution and thus also on the CCN concentration. For example, Borys et al. (2003) and Saleeby et al. (2013) found that higher aerosol loadings reduce the mean droplet diameter and thus the riming efficiency in MPCs.

In addition, ice crystals can be produced by secondary ice production mechanisms. Numerous studies observed ice crystal number concentrations (ICNCs) that exceed observed INP concentrations by several orders of magnitude (e.g. Hobbs and Rangno, 1985; Cantrell and Heymsfield, 2005; Crosier et al., 2011; Crawford et al., 2012; Lloyd et al., 2015; Lohmann et al., 2016a; Lawson et al., 2017). One explanation for the discrepancy between the INP and ice crystal number concentrations are secondary ice production mechanisms. Several secondary ice production mechanisms have been proposed, however their physical basis and their potential contribution remain poorly understood (e.g. Field et al., 2017; Sullivan et al., 2017; Korolev et al., 2020). For example, mechanical ice fragmentation upon ice-ice collision can lead to the production of a large number of secondary ice particles (e.g., Vardiman, 1978; Takahashi et al., 1995). Turbulence can increase the number of collisions (Pinsky and Khain, 1998) and potentially enhance secondary ice production by collisional fragmentation. Furthermore, a few laboratory studies have suggested that ice fragmentation might also occur upon sublimation in subsaturated regions at or underneath cloud base (e.g., Oraltay and Hallett, 1989; Dong et al., 1994; Bacon et al., 1998). However, the contribution of this mechanism to secondary ice production remains unclear, since the ice fragments formed in the subsaturated environment need to be transported in an ice supersaturated environment in order to influence the cloud microphysics (Korolev et al., 2020). Another possible secondary ice production mechanism is ice splintering during riming. Ice splinters can be formed when a supercooled cloud droplet of an appropriate size ($> 25\,\mu m$ in diameter) collides and freezes upon contact with a rimed ice particle ($> 0.5\,mm$ in diameter) (e.g. Mossop, 1978; Lamb and Verlinde, 2011). This process is usually referred to as the Hallett-Mossop process (Hallett and Mossop, 1974) and is known to be active at temperatures between -3 °C and -8 °C. Furthermore, secondary ice can be produced upon freezing of drizzle-sized droplets (e.g., Langham and Mason, 1958; Mason and Maybank, 1960; Lauber et al., 2018). This mechanism is known as droplet shattering or droplet fragmentation and has been suggested to be active over a larger temperature range compared to the Hallett-Mossop process (down to temperatures of -20 °C) and to be strongly dependent on the cloud droplet size (Lauber et al., 2018). Droplet shattering could for example enhance secondary ice production immediately above the melting layer, because the recirculation of ice and liquid through the melting layer could lead to the formation of large droplets (Korolev et al., 2020). Additionally, droplet shattering might also be important in regions with strong updrafts near cloud top (e.g., in cloud top generating cells), where large updrafts can lead to the production of drizzle-sized droplets and enhance ice formation and growth (see Chapter 4). The proposed secondary ice production mechanisms can increase the ICNC by several orders of magnitude. However, further research is required to enhance the physical understanding of these mechanisms, to identify conditions favorable for secondary ice production and to quantify their potential contribution.

Despite all processes that contribute to the formation and growth of ice particles and thus favor

the glaciation of MPCs, persistent MPCs have been observed in the Arctic (e.g. Shupe et al., 2006; Morrison et al., 2012) and in mountain regions (e.g. Borys et al., 2003; Geerts et al., 2011; Lowenthal et al., 2011; Dorsi et al., 2015; Lloyd et al., 2015; Lohmann et al., 2016a; Beck, 2017; Lowenthal et al., 2019). According to Rauber and Tokay (1991), two prerequisites need to be fulfilled to sustain mixed-phase cloud regions. Firstly, the environment needs to be supersaturated with respect to liquid water, which can be achieved through turbulence and sufficiently large updrafts. Secondly, the condensate supply rate needs to exceed the diffusional growth rate of ice crystals. These prerequisites can be fulfilled in an environment with limited INPs (e.g., Arctic), in regions with small ice crystals and/or a low ICNC (e.g., at the cloud top) or in regions with large updrafts (e.g., mountain regions). In the Arctic, long-wave radiative cooling at cloud top was suggested as a major driver for the production of turbulence at the cloud top, which resupplies the cloud top layer with condensate (Morrison et al., 2012). In an INP-limited regime, the few ice crystals rapidly grow by vapor deposition and sediment out quickly. On the other hand, in regions with complex terrain, the steep orography can produce turbulence and high updrafts, providing a continuous source of condensate (e.g., Lohmann et al., 2016a). It is important to understand the physical processes that govern the phase partitioning in MPCs, because the delicate balance between the production of supercooled liquid (e.g., by orographic lifting, radiative cooling, turbulence) and the consumption of supercooled liquid by ice processes (e.g., WBF process, growth of ice particles by vapor deposition and collisional processes) determines precipitation formation and the lifetime of MPCs (e.g., Korolev et al., 2017). Additionally, orographic effects can enhance precipitation formation and influence the spatial distribution of precipitation in various ways, which will be discussed in the following section.

1.3 Orographic precipitation

The most traditional view of orographic precipitation includes an air flow that is forced to ascend over a mountain barrier in a stable stratified atmosphere, which leads to adiabatic cooling of the air and eventually to condensation and precipitation formation on the windward side (Figure 1.3.a). On the lee side of the mountain barrier, downward motion leads to adiabatic warming of the air and consequently to the evaporation of the cloud. However, numerous studies have shown that precipitation formation over and near mountains is much more complex (e.g., Roe, 2005; Rotunno and Houze, 2007; Houze Jr, 2012; Smith, 2019). The microphysical time scale of cloud particle growth determines how rapidly condensate is converted into precipitation (see Section 1.2). This, together with the spatial scale of the orography, determines where precipitation falls along the mountain barrier (Houze Jr, 2012). On the other hand, the condensation, growth and evaporation of cloud particles exchange latent heat with the ambient air, which can influence the static stability of the atmosphere and thus the air flow (e.g., Fraser et al., 1973; Jiang, 2003). Consequently, the amount and distribution of orographic precipitation is determined by a complex interplay between the height and shape of the orography, the dynamical response of the flow impinging on a mountain barrier, the microphysics of cloud particle growth and the thermodynamics of the flow (e.g., Houze Jr, 2012).

Numerous mechanisms have been identified by which mountains can influence the air flow and enhance orographic precipitation (see Figure 1.3). For example, if the air flow toward a moun-

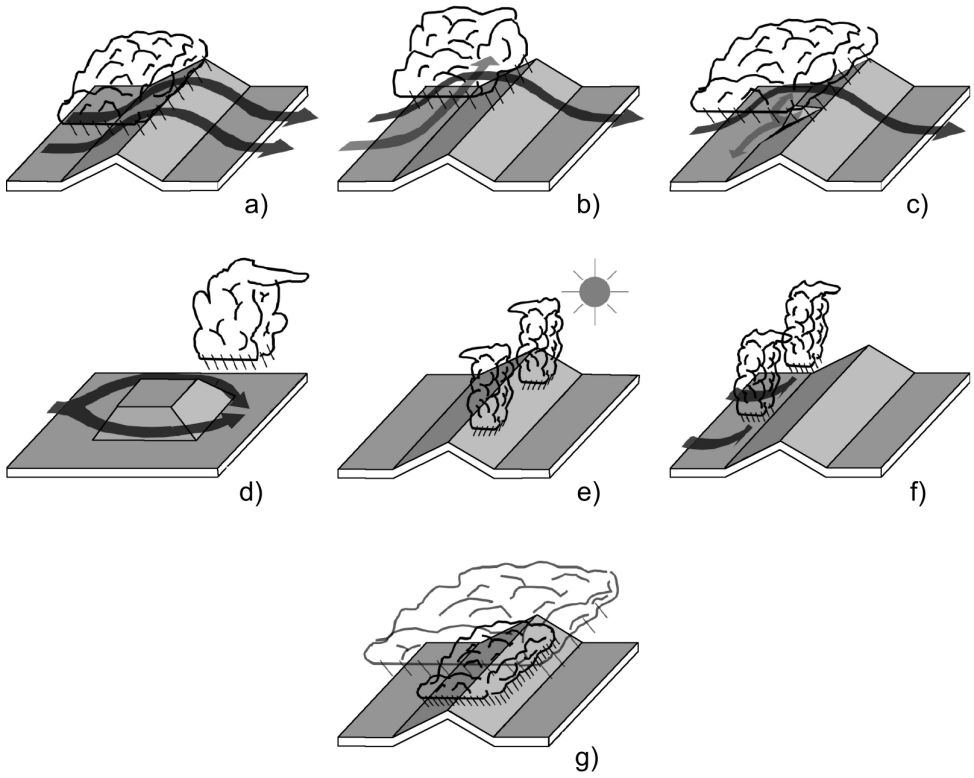

Figure 1.3: Schematic illustrations of different mechanisms of orographic precipitation: (a) stable upslope ascent, (b) partial blocking of the impinging air mass, (c) down-valley flow induced by evaporative cooling, (d) lee-side convergence, (e) convection triggered by solar heating, (f) convection owing to mechanical lifting above level of free convection, and (g) seeder-feeder mechanism. Figure taken from Roe (2005).

tain is not strong enough or the atmosphere is too stable, the low-level flow might be blocked and diverted around the mountain, because it cannot ascend over the mountain barrier (Figure 1.3.b). In the cases when the low-level flow is not diverted around the mountain, a stagnant blocked layer might build up in front of the mountain barrier, which extends the effective width of the mountain barrier and causes lifting further upstream (e.g., Rotunno and Ferretti, 2001; Jiang and Smith, 2003; Medina and Houze, 2003). The interface between the blocked layer and the stronger cross-barrier flow is often characterized by a shear layer, which can be a source of turbulent motion (e.g., Houze Jr and Medina, 2005; Medina et al., 2005; Medina et al., 2007). Shear-induced turbulence can produce pockets of locally enhanced liquid water content, which can increase growth of precipitation particles through riming. In addition, turbulent motion can increase collisions between cloud particles and thus growth by aggregation (see also Chapter 3). A further mechanism that can enhance orographic precipitation is the so-called seeder-feeder mechanism (Bergeron, 1965) (see Figure 1.3g). A pre-existing precipitating cloud (seeder cloud) is advected over a hill or a small mountain, whereas a shallow orographically-induced cap cloud (feeder cloud) forms above a small-scale topographic feature. The feeder cloud would not have generated significant precipitation by itself, because growth by condensation and collision-coalescence would not be able to form precipitation-sized particles within the time available. However, the low-level liquid cloud can "feed" on the precipitation particles that formed in the

seeder region of the cloud and thus enhance orographic precipitation through riming, collision-coalescence or depositional growth (e.g., Hill et al., 1981; Bader and Roach, 1977; see also Chapter 4).
Despite considerable efforts and progress in improving our understanding of MPCs and precipitation formation over the past decades, our understanding of the numerous interlinked cloud processes remains incomplete (Korolev et al., 2017). Moreover, mountains add an extra dimension to this unresolved challenge. Innovative measurement strategies and approaches are required to improve our understanding of MPCs and precipitation formation in complex terrain.

1.4 Cloud observations

Clouds can be observed by in situ and remote sensing instrumentation. In situ instruments can directly measure the cloud properties along the measurement path (e.g., along the flight track). However, these observations are too intermittent in time and space to obtain a thorough characterization of the cloud structure. On the other hand, remote sensing instrumentation can continuously measure the vertical cloud structure or provide a snapshot of the cloud by scanning planes or volumes, but rely on cloud retrieval algorithms (i.e., are based on assumptions regarding the cloud properties). Thus, the combination of in situ and remote sensing observations is favorable to obtain a comprehensive understanding of the cloud structure. In the following sections, we describe in situ instrumentation (Section 1.4.1) and remote sensing instrumentation (Section 1.4.2), which are relevant for this thesis or frequently applied in atmospheric science.

1.4.1 In situ observations

In situ observations of clouds have been performed with different measurement platforms (Figure 1.4). Ground-based weather stations and measurement towers can provide continuous measurements of clouds over several hours or days and are thus useful to study the temporal evolution of clouds (e.g. Borys et al., 2003; Lowenthal et al., 2011; Henneberger et al., 2013; Lloyd et al., 2015). However, ground-based measurements are limited to single point observations and can be influenced by surface-based processes (e.g. Lloyd et al., 2015; Geerts et al., 2015; Beck et al., 2018). Indeed, ICNCs of several hundreds to thousands per liter are frequently reported at mountain-top stations (e.g., Rogers and Vali, 1987; Lloyd et al., 2015; Lowenthal et al., 2019). On the other hand, aircraft can travel large distances and freely choose their flight path, which is useful to obtain a thorough characterization of the cloud structure. However, the high traveling velocity of aircraft ($100\,\mathrm{m\,s^{-1}}$) limits their spatial resolution to several hundred meters or a few kilometers, because a sufficiently large cloud volume needs to be sampled for robust statistics. Moreover, aircraft have minimum altitude constraints, which limits observations within the boundary layer in orographically complex terrain (e.g., in narrow mountain valleys).
To overcome the gap in observations within the planetary boundary layer between ground-based measurements and manned aircraft, cable car platforms (Beck et al., 2017) and tethered balloon systems (e.g. Siebert et al., 2003; Maletto et al., 2003; Lawson et al., 2011; Sikand et al., 2013; Canut et al., 2016) can be used. Both platform benefit from a lower aspiration speed ($10\,\mathrm{m\,s^{-1}}$) compared to aircraft ($100\,\mathrm{m\,s^{-1}}$), which is advantageous for obtaining high resolution

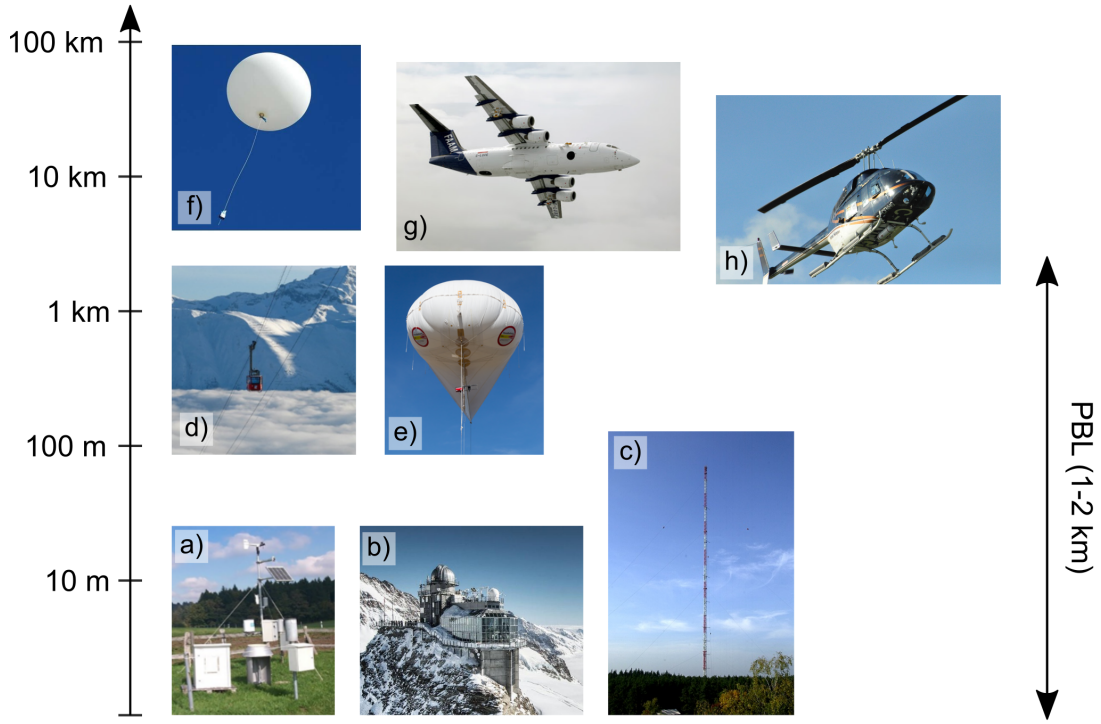

Figure 1.4: Overview of different measurement platforms that can be used to obtain in situ observations of clouds: a) weather stations, b) mountain-top stations, c) measurement towers, d) HoloGondel, e) HoloBalloon, f) radiosondes, g) aircrafts, h) helicopters. A picture of the newly developed HoloBalloon platform is shown in (e).

observations of clouds on a scale of a few meters. The locations of cable cars are limited to mountain regions, whereas the deployment of tethered balloon systems is more flexible in terms of the measurement location and can for example also be used to study ground fog or low stratus clouds above the lowlands. In this thesis, a new measurement platform on a tethered balloon system is developed to study boundary layer clouds in complex terrain and in densely populated regions. Due to fluctuations in the wind speed and direction towards an instrument that is installed on a tethered balloon system, the choice of the instrument is of particular importance. A large variety of instruments and measurement techniques exist to measure cloud microphysical properties (Baumgardner et al., 2011; Brenguier et al., 2013). Most of the instruments that measure the size distribution and shape of individual cloud particles are based on optical detection. Single-particle light scattering instruments (e.g. FSSP-100, Field et al., 2003; CDP, Lance et al., 2010; CAS, Baumgardner et al., 2001; CAS-DPOL, Glen and Brooks, 2013; SID1 and SID2, Ulanowski et al., 2013; Cotton et al., 2010) can measure cloud particles in the size range from 1 - 50 µm. These instruments are based on the principle of light scattering by single particles in a focused laser beam, whereby the intensity of the scattered light is proportional to the particle size. The particle size cannot be measured directly, but is based on assumptions about the particle shape, the refractive index and the orientation of the particles (e.g. Baumgardner et al., 2011; Brenguier et al., 2013).

As an alternative to the scattering technique, the image of a cloud particle can be captured. Single particle imaging techniques have the advantage that the particle size and shape can be measured directly and are not based on assumptions about the refractive index (Brenguier et al.,

2013). However, uncertainties in the sizing can occur for out-of-focus particles. Two different particle imaging techniques are applied: the first one scans a linear photodiode array (e.g., 2D-S, Lawson et al., 2006; 2D-C and 2D-P, Knollenberg, 1970, Knollenberg, 1981; CIP and PIP, Baumgardner et al., 2001; HVPS, Lawson and Cormack, 1995, Lawson et al., 1998) and the second one uses a two dimensional photodetector array (CPI, Lawson et al., 2001) to capture an image of the particles that pass through the sample volume.
The scattering and imaging probes presented above have a sample volume that depends upon particle size and air speed (e.g. Baumgardner and Korolev, 1997; Baumgardner et al., 2011; Brenguier et al., 2013). Thus, in order to account for fluctuations in wind speed and direction on a tethered balloon system, most of the cloud probes use an inlet to ensure a steady sampling velocity. However, the use of inlets can lead to size-dependent particle losses at the inlet and anisokinetic sampling effects (Baumgardner et al., 2011). One technique that overcomes this problem is digital in-line holography, which has a well-defined sample volume independent of particle size and air speed, making it favorable for measurements on a tethered balloon system. Digital in-line holography can measure the three-dimensional position, size and shape of each individual particle of an ensemble of cloud particles inside a three-dimensional sample volume. Besides the advantage of a well-defined sample volume, in-line holography is able (1) to measure cloud particles over a wide size range (6 µm - 2 mm) and thus to measure both small cloud droplets and large precipitation-sized particles, (2) to measure the spatial distribution of an ensemble of cloud particles within the sample volume (e.g. Beals et al., 2015), which enables studying small-scale processes such as entrainment or particle clustering and (3) to measure a large, coherent cloud volume (tens of cm^{-3}) without assumptions about the homogeneity of the cloud, since a snapshot of the cloud volume is captured (e.g. Baumgardner et al., 2011). The working principle of in-line holography is described in more detail in Chapter 2.
Since several years, digital in-line holography has been applied more extensively in atmospheric science and has provided insights into the microphysical structure of clouds. Digital holographic cloud imagers have been installed on ground-based measurement stations (e.g., Thompson, 1974; Kozikowska et al., 1984; Borrmann et al., 1993; Raupach et al., 2006; Henneberger et al., 2013; Schlenczek et al., 2017), aircraft (e.g, Conway et al., 1982; Fugal and Shaw, 2009; Beals et al., 2015; Glienke et al., 2017; Desai et al., 2019; Glienke et al., 2020) and cable cars (Beck et al., 2017). To our knowledge, this is the first time that a holographic cloud imager is deployed on a tethered balloon system.

1.4.2 Remote sensing observations

There are two types of remote sensing instrumentation - passive and active sensors. Passive remote sensing instruments (e.g., radiometers) measure radiation that is naturally emitted or scattered by atmospheric gases and cloud particles. On the other hand, active remote sensing instruments (e.g., radar, lidar) emit their own radiation and measure the radiation that is scattered back from the targets. In this section, we briefly summarize the basic principles of active and passive remote sensors, which are relevant for the present thesis.
RADAR (RAdio Detection and Ranging) is the most commonly used active sensor in atmospheric science. Radars emit electromagnetic waves in the radar frequency range (1 - 100 GHz) in a

specific direction (transmitted signal), which interact with an arbitrary target that lies along the beam of the radar, and measure the signal that is scattered back from the target (received signal). The run time of the pulse provides information about the distance of the target, since electromagnetic waves propagate at the speed of light. Furthermore, the received signal contains information about (1) the received power, from which the reflectivity of the target can be derived; (2) the Doppler shift in frequency, which is indicating the target's velocity along the radar beam (radial velocity); and (3) the polarization of the signal, from which information on target shape and orientation can be derived (Houze Jr, 2014). The following description of radar theory is based on Houze Jr (2014).

The power received by the antenna averaged over a time interval of 0.01-0.1 s is given by

$$\bar{P}_r = \frac{Z|K|^2}{r^2 C_R} \tag{1.1}$$

where Z is the radar reflectivity, $|K|^2$ is the square of the absolute value of the complex index of refraction and r is the distance between the scattering target and the radar (Houze Jr, 2014). The radar constant C_R is given by the following equation

$$C_R = \frac{64\lambda^2 r^2}{P_t G^2 \pi^2 V_{res}} \tag{1.2}$$

where λ is the wavelength, P_t is the transmitted power, G is the antenna gain and V_{res} is the resolution volume. While all parameters are known or can be measured directly, $|K|^2$ depends on the frequency and on the composition of the scatterers and is different for water and ice. Thus, the equivalent reflectivity factor Z_e is often used instead, where $|K|^2$ is set to 0.93 (value for liquid water):

$$Z_e = \frac{r^2 \bar{P}_r C_R}{0.93} \tag{1.3}$$

A $|K|^2$ value of 0.197 is usually used for ice particles. Thus, the Z_e value for liquid hydrometeors is a factor of 4.7 higher than for ice particles of the same size.

If the Rayleigh scattering criterion is met (i.e., size of the scattering object is much smaller than the wavelength of the electromagnetic wave), the radar reflectivity can also been obtained from the sixth moment of the size distribution of the cloud particles (Houze Jr, 2014):

$$Z = \int_0^\infty D^6 \, N(D) \, dD \tag{1.4}$$

where $N(D)$ is the particle size distribution and D is the particle diameter. Since Z is proportional to the sixth moment of the size distribution, the Z signal is strongly dominated by large particles. Therefore, Z is often expressed on a logarithmic scale with the units:

$$\mathrm{dBZ} = \mathrm{Z[dB]} = 10 \log_{10} \left(\frac{\mathrm{Z}}{\mathrm{mm}^6 \ \mathrm{m}^{-3}} \right) \tag{1.5}$$

Typical values of Z for various hydrometeors and precipitation types are summarized in Table 1.1.

In addition, useful information about the cloud properties can be obtained from radars that

Table 1.1: Typical values of Z for various hydrometeors and precipitation types (adapted from Lohmann et al., 2016b).

Scatterer	Z values
Cloud droplets	- 40 to -20 dBZ
Mixed-phase clouds	- 20 to -10 dBZ
Drizzle	- 20 to 0 dBZ
Very light rain or light snow	0 to 10 dBZ
Moderate rain and heavier snow	10 to 30 dBZ
Melting snow	30 to 45 dBZ
Moderate to heavy rain	30 to 60 dBZ
Hail	$>$ 60 dBZ

transmit and receive radiation polarized in several orientations (e.g., in vertical and horizontal direction). One parameter that can be calculated from the polarization signal is the linear depolarization ratio (LDR), which is a measure of how much a horizontally transmitted signal is depolarized (Houze Jr, 2014):

$$LDR = 10 \log_{10} \left(\frac{Z_{HV}}{Z_{HH}} \right) \tag{1.6}$$

where Z_{HV} indicates signals that are horizontally transmitted and vertically received and Z_{HH} signals that are horizontally transmitted and horizontally received. Hydrometeors only depolarize electromagnetic waves if they are aspherical. Therefore, a spherical cloud particle returns a signal that is purely horizontally polarized, resulting in a LDR of -∞. If a hydrometeor is aspherical, then the returned signal has both a horizontal and a vertical depolarization component, resulting in a $LDR >$ -∞. The LDR values do not exceed 0, because the cross-polar signal is generally smaller than the co-polar signal. Thus, the LDR can provide information about the shape of the cloud particles and the hydrometeor type. Typical LDR values of cloud particles range between -30 dB (e.g., drizzle) and -10 dB (e.g., needles) (e.g., Doviak and Zrnić, 1993; North et al., 2014). Moreover, the LDR is a good indicator of the melting layer, because the LDR values are enhanced for wet ice particles (-10 to -20 dB) due to the increased complex index of refraction (e.g., Houze Jr, 2014).

Besides the information about the cloud properties from the Z and the LDR signals, the Doppler shift of the frequency that occurs between the transmitted and received signal can provide information about the motions of the cloud particles and of the air. This phase shift occurs due to moving targets, which are detected by the cloud radar. From the phase shift ϕ_p and the wavelength λ of the cloud radar, the radial velocity V_R can be calculated (Houze Jr, 2014):

$$\frac{d\phi_p}{dt} = \frac{4\pi V_R}{\lambda} \tag{1.7}$$

The radial velocity V_R is the velocity of the target parallel to the direction of the beam. For vertically-pointing cloud radars, the Doppler velocity is composed of the fall velocity of the hydrometeors and the vertical wind component. If the Doppler velocity is directed away from the radar, this indicates regions with updraft conditions.

So far, we only considered interactions of the radar signal with single targets. However, numerous targets are usually present in the sample volume of the radar. Each of the individual

targets produces a Doppler shift in frequency according to its radial velocity, which leads to a distribution of Doppler radial velocities (i.e., Doppler spectrum). From the Doppler spectrum, the mean Doppler velocity (1st moment) and the width of the Doppler spectrum (2nd moment) can be derived (e.g., Kollias et al., 2007). The spectral width is the standard deviation of the Doppler spectrum. Small values indicate a narrow distribution, whereas higher spectral widths indicate a larger variability of the Doppler velocities within the sample volume. Possible reasons for a higher spectral width are turbulent motion and/or the presence of multiple particle populations with different fall speeds.
Another active remote sensor is the LIDAR (LIght Detection and Ranging). Lidars work with the same physical principles as radars, but transmit laser light (with wavelengths from ultraviolet to infrared radiation) instead of operating in the microwave range. Consequently, the lidar is sensitive to smaller particles (e.g., aerosols, non-precipitating clouds) and its signal gets attenuated by large cloud particles or deep cloud layers. Thus, lidars can be used to complement the information obtained from cloud radars by providing observations of thin cloud layers and aerosol layers within the atmosphere.
In contrast to active remote sensors, microwave radiometers detect the microwave radiation that is naturally emitted by atmospheric gases (e.g., water vapor, oxygen), cloud droplets and ice crystals. Several atmospheric gases have specific absorption bands in the microwave range, which can be used to derive information about the atmospheric properties. For example, measurements along the wing of the 22.235 GHz water vapor absorption line can be used to obtain the humidity profile of the atmosphere (Löhnert and Crewell, 2003). On the other hand, the absorption band of oxygen (51 - 58 GHz) can be used to observe the vertical temperature profile (Crewell and Lohnert, 2007). In addition, since microwave radiometers are usually equipped with multiple receiving channels, information about the liquid water path and the integrated water vapor can be obtained by measuring the emission of liquid water at two frequency channels - one close to the center of the water absorption band (e.g., 22 GHz) and one close to the edge of the absorption band (e.g., 31 GHz).

1.5 Motivation and objectives of this thesis

A complex interplay between numerous microphysical and dynamical processes on different temporal and spatial scales determine the life cycle of MPCs. Mountain ranges such as the Alps add further complexity to this multi-scale system, as orographic effects can influence the structure of MPCs and further enhance precipitation. This makes accurate precipitation forecasting in complex terrain challenging. Innovative measurement strategies are required to improve our understanding of the dynamics and microphysics of orographic MPCs and precipitation.
Due to limitations on the ability of aircraft to fly in cloudy conditions in complex terrain (e.g., narrow valleys) and the influence of surface processes at mountain-tops, a new measurement platform on a tethered balloon system (HoloBalloon) was developed in the framework of this thesis to study boundary layer clouds in complex terrain. The HoloBalloon platform merges for the first time the advantages of holography (well-defined sample volume, ability to observe the spatial distribution of an ensemble of cloud particles) and the benefits of a tethered balloon system (high-resolution measurements). However, as highlighted in Section 1.4, in situ observations

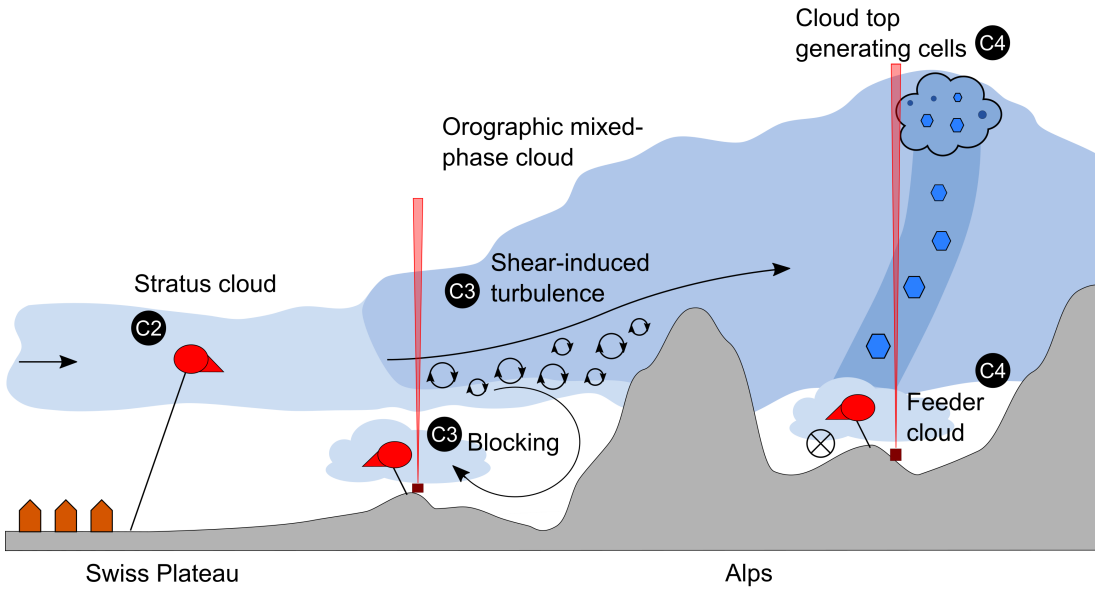

Figure 1.5: Overview of the observed microphysical features and processes that will be discussed in the present thesis. The chapters are indicated by C2, C3 and C4.

are limited in terms of temporal and spatial coverage and thus reinforce the complementary use of in situ and remote sensing instrumentation. In the present thesis, observations from a multi-dimensional set of instruments including remote sensing instrumentation, balloon-borne in situ observations and ground-based precipitation and aerosol measurements are analyzed to obtain a more comprehensive understanding of orographic MPCs and of the pathways of precipitation formation.

With the aim to extend the current knowledge and understanding of orographic MPCs and precipitation, the objectives of the present thesis are:

1. *To design and develop a new measurement platform for boundary layer clouds in complex terrain by exploiting the advantages of digital in-line holography and tethered balloon systems (HoloBalloon):* This includes the development of a new HOLographic Imager for Microscopic Objects (HOLIMO) for balloon-borne application and the characterization of the newly developed cloud imager (e.g., size calibration, optical resolution limit). The measurement platform is also equipped with auxiliary instruments to observe the meteorological cloud properties (see Chapter 2).

2. *To validate the HoloBalloon platform in low stratus clouds over the Swiss Plateau and to highlight its potential in studying boundary layer clouds:* The first observations with the HoloBalloon platform were obtained in a supercooled low stratus cloud over the Swiss Plateau. These observations are used to validate the newly developed measurement platform in terms of its ability to accurately measure cloud properties and meteorological parameters, to capture small-scale variations in the cloud properties (e.g., particle size distribution) and to obtain vertical profiles of the phase-resolved cloud properties on a meter scale. Based on this case study, the scale-dependent analysis strategies of the HoloBalloon

platform are demonstrated and its potential contribution to cloud research is discussed (see Chapter 2).

3. *To study the influence of orographic effects on the microphysics and precipitation formation in an Alpine environment using a multi-dimensional set of instruments:* An extensive field campaign was performed in the Swiss Alps to investigate the Role of Aerosols and CLouds Enhanced by Topography on Snow (RACLETS) by combining a multi-dimensional set of instruments. The interplay between orography, dynamics, microphysics and precipitation in orographic clouds is discussed on the basis of selected case studies. For example, the influence of low-level blocking and shear-induced turbulence on the cloud microphysics and precipitation formation in an inner-Alpine valley is investigated (Chapter 3). Additionally, the role of flow blocking for the formation of low-level feeder clouds is examined (Chapter 3).

4. *To investigate the microphysical pathways of precipitation formation in the seeder and feeder regions of orographic MPCs using an aerosol-cloud-precipitation perspective:* The RACLETS campaign was designed to observe the pathways of precipitation formation from an aerosol-cloud-precipitation perspective, which allows studying a wide range of processes from ice nucleation, to secondary ice production, to ice growth by vapor deposition and collisional processes, to fallout of precipitation-sized particles. Unique microphysical signatures contributing to precipitation formation were identified in the seeder regions (e.g., cloud top generating cells) and feeder regions (e.g., orographically-induced low-level feeder cloud) of mixed-phase clouds and discussed on the basis of a case study. The importance of cloud top generating cells for precipitation formation is investigated and potential mechanisms that enhance ice formation and growth within generating cells are proposed. Additionally, the role of secondary ice production within the low-level feeder cloud is examined (see Chapter 4).

5. The thesis ends with a summary and outlook in Chapter 5.

Chapter 2

Using a holographic imager on a tethered balloon system for microphysical observations of boundary layer clouds

F. Ramelli[1], A. Beck[1], J. Henneberger[1] and U. Lohmann[1]

[1] Department of Environmental System Sciences, Institute for Atmospheric and Climate Science, ETH Zurich, Switzerland

This work has been published in Atmospheric Measurement Techniques.
DOI: https://doi.org/10.5194/amt-13-925-2020

Abstract

Conventional techniques to measure boundary layer clouds such as research aircraft are unable to sample in orographically diverse or densely populated areas. In this paper, we present a newly developed measurement platform on a tethered balloon system (HoloBalloon) to measure in situ vertical profiles of microphysical and meteorological cloud properties up to 1 kilometer above ground. The main component of the HoloBalloon platform is a holographic imager, which uses digital in-line holography to image an ensemble of cloud particles in the size range from small cloud droplets to precipitation-sized particles in a three-dimensional volume. Based on a set of two-dimensional images, information about the phase-resolved particle size distribution, shape and spatial distribution can be obtained. The velocity-independent sample volume makes holographic imagers particularly well suited for measurements on a balloon. The unique combi-

nation of holography and balloon-borne measurements allows for observations with high spatial resolution, covering cloud structures from the kilometer down to the millimeter scale.
The potential of the measurement technique in studying boundary layer clouds is demonstrated on the basis of a case study. We present observations of a supercooled low stratus cloud during a Bise situation over the Swiss Plateau in February 2018. In situ microphysical profiles up to 700 m altitude above the ground were performed at temperatures down to -8 °C and wind speeds up to 15 $\mathrm{m\,s^{-1}}$. We were able to capture unique microphysical signatures in stratus clouds, in the form of inhomogeneities in the cloud droplet number concentration and in cloud droplet size, from the kilometer down to the meter scale.

2.1 Introduction

Boundary layer clouds play a key role in regulating the Earth's climate and controlling its weather systems and are important for many aspects of our daily life. First, low-level clouds are an important part of the Earth's radiation balance (Hartmann et al., 1992). For example, low stratus clouds cover an extensive area over ocean and land (Warren et al., 1986; Warren et al., 1988), can persist for several days (e.g., Bendix, 2002) and cool the surface in the annual mean (e.g., Randall et al., 1984). Second, low visibilities associated with fog can impact road, ship and aviation traffic, causing accidents, delays or cancellations (e.g. Fabbian et al., 2007; Bartok et al., 2012). The resulting economic losses are comparable to those caused by winter storms (Gultepe et al., 2007). Moreover, with the constantly increasing contribution of photovoltaic power, reliable forecasts of low-level cloud cover are of increasing importance for the renewable energy sector (Köhler et al., 2017).
However, current state-of-the-art numerical weather prediction (NWP) models have major issues in predicting the exact time and location of the formation and dissipation of low-level boundary layer clouds (e.g., Bergot et al., 2007; Müller et al., 2010; Steeneveld et al., 2015; Román-Cascón et al., 2016). This is due to an incomplete understanding and a poor representation of the numerous processes occurring in boundary layer clouds, spanning from the microscale to the synoptic scale. The life cycle of boundary layer clouds is a result of complex interactions among microphysical, thermodynamic, radiative, dynamic, aerosol and land surface processes. These processes are often not well parameterized in current operational NWP models, and the horizontal (Pagowski et al., 2004) and vertical (Tardif, 2007) resolution of these models is insufficient to cover the characteristic cloud scales. From an observational perspective, there is a need for additional comprehensive and high-quality observations of boundary layer clouds, especially of their vertical structure. Presently, a large fraction of the observations of boundary layer clouds are performed by satellites (e.g., Bendix, 2002; Bennartz, 2007; Cermak et al., 2009; van der Linden et al., 2015). Satellites have a continuous spatial coverage and are useful to obtain climatologies of the optical and microphysical properties of clouds (Bendix, 2002; Cermak et al., 2009). However, current satellite observations are typically too coarse to resolve scales below 250 m and have limitations in measuring cloud properties in the lowest kilometer of the planetary boundary layer (PBL) due to interference signals from the ground (e.g., Marchand et al., 2008; Liu et al., 2017). Thus, in situ measurements of boundary layer clouds are important to gain a better understanding of the microphysical pathways in clouds.

Commonly, microphysical in situ measurements within the PBL are performed using a variety of measurement platforms, such as research aircraft (e.g., Sassen et al., 1999; Verlinde et al., 2007), helicopters (e.g., Siebert et al., 2006), cable cars (e.g., Beck et al., 2017), tethered balloon systems (TBSs) (e.g., Siebert et al., 2003; Maletto et al., 2003; Lawson et al., 2011; Sikand et al., 2013; Canut et al., 2016) or launched balloon platforms (e.g., Creamean et al., 2018), each of which has its own advantages and disadvantages. For example, research aircraft can travel large distances and freely choose their flight path, but they have minimum altitude constraints, which limits observations within the lowest kilometer of the PBL. Moreover, due to high traveling speeds ($100\,\mathrm{m\,s^{-1}}$), aircraft measurements have limited spatial resolution and can be influenced by ice shattering (Korolev et al., 2011). Ice shattering occurs if an ice crystal impacts the instrument tips or an inlet prior to entering the detection volume, which can result in a large number of small ice particles being a measurement artifact. To investigate small-scale processes in clouds, measurement platforms with lower true air speed are advantageous. The aspiration speed on cable cars ($10\,\mathrm{m\,s^{-1}}$) is one order of magnitude lower than on aircrafts, which enables us to probe the cloud with a much higher spatial resolution (Beck et al., 2017). However, the locations of cable cars are limited to mountain areas. TBS can achieve an instrumental resolution similar to that of cable cars and are more flexible in terms of choosing the measurement location. Measurements with TBS can cover the full vertical extent of the PBL from the surface up to 1-2 kilometers. However, conventional, blimp-like TBSs are limited to wind speeds below $10\,\mathrm{m\,s^{-1}}$ due to the instability of the balloon at higher wind speeds (e.g., Lawson et al., 2011; Canut et al., 2016; Mazzola et al., 2016). Moreover, TBSs can be deployed further away from the ground, reducing the effects of surface-based processes such as blowing snow (Lloyd et al., 2015; Beck et al., 2018).

In this paper, we present a newly developed measurement platform for boundary layer clouds (HoloBalloon), consisting of a holographic cloud imager and a meteorological instrument package on a kytoon. Kytoons are a hybrid balloon-kite combination allowing stable flight at wind speeds up to $30\,\mathrm{m\,s^{-1}}$. The stability in high wind speeds makes kytoons a promising measurement platform for cloud research, especially in locations with strong wind conditions (e.g., mountain regions). Due to the low aspiration velocities of TBS, the choice of the instrument is of particular importance, since fluctuations in wind speed and direction could influence the measurements. Most cloud probes use an inlet to ensure a steady sampling velocity in fluctuating wind speeds (Baumgardner et al., 2011). However, the use of inlets increases measurement uncertainty, due to size-dependent particle losses at the inlet and non-isokinetic sampling effects. One technique that overcomes this problem is digital in-line holography, which provides a well-defined sample volume independent of particle size and aspiration velocity, making holographic cloud imagers particularly well suited for measurements on TBS. Digital in-line holography can simultaneously capture single particle information (position, size and shape) of an ensemble of cloud particles within a three-dimensional detection volume. Thus, it provides information of the phase-resolved particle size distribution (e.g., Beck et al., 2017), as well as the spatial distribution of an ensemble of cloud particles within a cloud volume on a millimeter scale (e.g., Beals et al., 2015). More detailed information about the working principle of a holographic imager will follow in Section 2.3.1. Digital holographic cloud imagers have been used in previous field

campaigns on ground-based (e.g., Thompson, 1974; Kozikowska et al., 1984; Borrmann et al., 1993; Raupach et al., 2006; Henneberger et al., 2013; Schlenczek et al., 2017), airborne (e.g., Conway et al., 1982; Fugal and Shaw, 2009; Beals et al., 2015; Glienke et al., 2017; Desai et al., 2019) and cable car (Beck et al., 2017) platforms, but have not yet been deployed on TBS.
The HoloBalloon platform merges the advantages of holography (well-defined sampling volume, spatial distribution of cloud particles) with the benefits of a TBS (high-resolution measurements) with the aim to observe the cloud structure on different scales. Information about the macroscopic cloud structure can be obtained from the vertical profiles up to 1 kilometer above the ground, and information about the cloud microstructure can be extracted from the cloud particle spatial distribution within a single hologram. The HoloBalloon platform was tested in boundary layer clouds over the Swiss Plateau. Here we present observations of a case study during a stratus cloud event. The cloud structure is analyzed on different scales, starting with the large-scale cloud structure of tens of kilometers and moving down to the cloud microstructure on the meter scale. A particular emphasis is placed on cloud inhomogeneities. Previous observations found inhomogeneities in cloud properties on scales of a few tens of meters (e.g., Korolev and Mazin, 1993; Garcıa-Garcıa et al., 2002; Gerber et al., 2005) or even on the submeter scale (e.g., Baker, 1992; Brenguier, 1993; Beals et al., 2015; Beck et al., 2017; Desai et al., 2019), which were attributed to different physical processes such as turbulent mixing or entrainment. These microphysical signatures can have important implications for the cloud structure. For example, on a millimeter scale, they can be of importance for particle growth by collision-coalescence and thus for the efficiency of precipitation formation. Inhomogeneities at scales of hundreds of meters and kilometers can be important for radiative heating and cooling. In this paper, we investigate inhomogeneities in the microphysical properties of stratus clouds and aim to understand the formation mechanisms of such inhomogeneities. Throughout this study, inhomogeneities are defined by the variability in the cloud droplet number concentration and cloud droplet size.
The first part of the paper introduces the HoloBalloon measurement platform (Section 2.2). The working principle and the setup of the newly developed holographic cloud imager is described in Section 2.3. Observations of a case study in stratus clouds obtained with the HoloBalloon platform are presented in Section 2.4. On the basis of these observations, the potential of the HoloBalloon platform in studying boundary layer clouds is discussed in Section 2.5.

2.2 Description of the HoloBalloon measurement platform

The HoloBalloon platform is designed to obtain vertical, in situ profiles of the microphysical and meteorological cloud properties of boundary layer clouds up to 1 kilometer above ground. Our TBS consists of a 175 m^3 kytoon (Desert Star, Allsopp Helikite, UK), a 1200 m long Dyneema cable and a gasoline winch to launch and recover the TBS (see Figure 2.1). The balloon has a net lift of 85 kg at sea level. Kytoons are a hybrid combination of a helium balloon and a kite, exploiting both for lift. The helium balloon creates static lift, while the kite creates aerodynamic lift in wind. The kite utilizes a long keel to provide stability in high-wind conditions. The maximum operational wind speed of our TBS is 25 $m\,s^{-1}$. So far, we operated the TBS in wind speeds of up to 15 $m\,s^{-1}$. A further advantage of the kite is that it ensures that the instrument

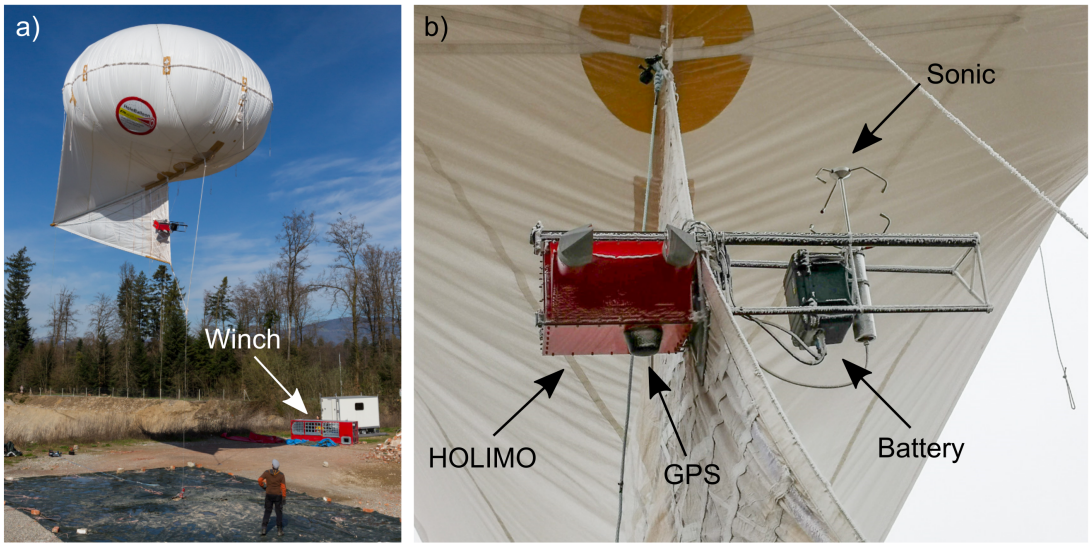

Figure 2.1: Experimental setup of the HoloBalloon platform consisting of a tethered balloon system (a) and the instrument package (b). The winch is visible in (a). The instrument package includes the holographic cloud imager HOLIMO 3B, a 3D sonic anemometer as well as a temperature and humidity sensor (not visible). The left picture has been taken by Pascal Halder (`naturphotos.ch`)

platform is oriented into the wind, allowing for the spatial distribution of cloud particles to be assessed.

The cable and winch are designed to withstand forces up to 4 tons, which can occur during high wind speed conditions ($> 15\,\mathrm{m\,s^{-1}}$). The 7 mm Dyneema cable has a length of 1200 m and a breaking strength of 8200 kg. At wind speeds larger than $5\,\mathrm{m\,s^{-1}}$, the TBS can have a flight angle of up to 45° due to the kytoon design, reducing the maximum flight height to 850 m. A system of three Platipus anchors is used to secure the balloon to the ground. The tethered balloon is launched and retrieved with a winch powered by a V8 Chevy engine (Skylaunch, UK). The winch has a line speed of $1\,\mathrm{m\,s^{-1}}$ forward and reverse, which allows a vertical profile of 500 m in 8 minutes.

The instrument package is installed at the keel of the HoloBalloon platform. The key component is the HOLographic Imager for Microscopic Objects (HOLIMO) (see Section 2.3) which can measure phase-resolved cloud properties. Additionally, the HoloBalloon platform is equipped with a meteorological instrument package (see Figure 2.1) consisting of a 3D sonic anemometer (Thies, 4.3830.20.340) and a heated temperature and humidity sensor (HygroMet4, Rotronic) in an actively ventilated radiation shield (RS24T, Rotronic). The platform is powered by a 1000 Wh battery, which allows for continuous operation of the instrument package for up to 5 hours. Data are temporally stored on a 4 TB solid-state drive and a mobile router enables remote access of the platform via a mobile data network connection (similar to Beck et al., 2017). The HoloBalloon instrument platform has a total weight of about 22 kg, consisting of the HOLIMO 3B instrument (13 kg), the meteorological instrumentation (5 kg) and the battery pack (4 kg).

To obtain reliable measurements of wind speed and direction, the motion of the balloon needs to be removed (e.g., Canut et al., 2016). Here we used a GPS antenna (TW3740, Tallysman) and

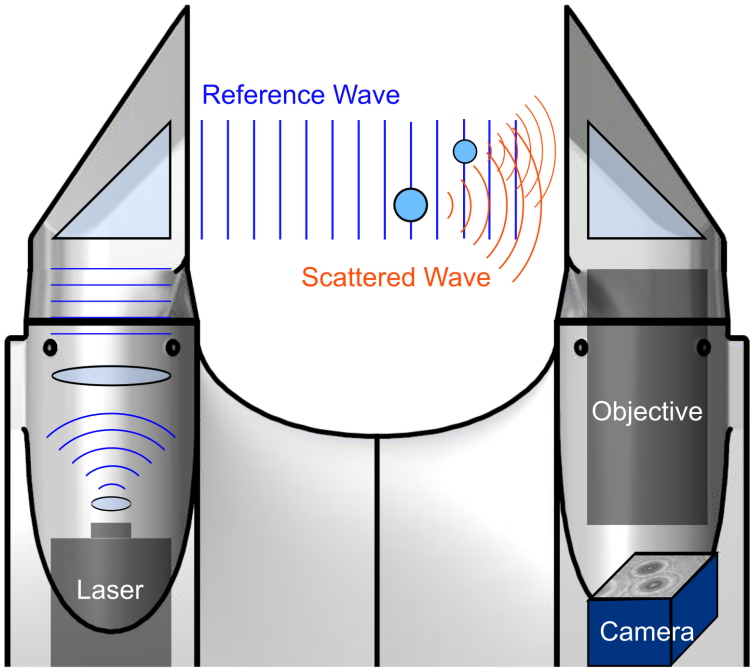

Figure 2.2: Schematic of the working principle of digital in-line holography. A collimated laser beam is scattered by two particles. The scattered waves interfere with the reference wave and form an interference pattern (i.e., a hologram) which is recorded by a digital camera.

an inertial navigation system (Ellipse2-N, SBG Systems) to measure the position, velocity and orientation of the instrument package. The GPS antenna and the inertial navigation system are fixed on the HOLIMO 3B instrument and are thus an integral part of the instrument package. We followed the procedure described in Elston et al. (2015) to convert the wind measurements from the inertial frame to the sonic anemometer frame and thus to correct for the motion of the balloon. The corrected wind measurements are presented and compared to other wind observations in Section 2.4.2.

2.3 HOLographic Imager for Microscopic Objects

The main component of the HoloBalloon instrument package is the holographic cloud imager HOLIMO 3B, which can image cloud particles between 6 µm and 2 mm within a three-dimensional detection volume. Despite its open-path configuration, HOLIMO 3B has a velocity-independent well-defined sample volume. This property makes HOLIMO 3B particularly well suited for application on a TBS due to fluctuating aspiration speeds towards a TBS.

2.3.1 Working principle of digital in-line holography

HOLIMO 3B works on the principle of digital in-line holography (Figure 2.2), which consists of a two-step process requiring a coherent light source and a digital camera. In the first step, the interference pattern of a reference wave (laser) and a scattered wave (the light scattered by a cloud particle in the sample volume) is recorded as a hologram. The second step involves a reconstruction process, in which the 2D shadowgraphs and 3D in-focus position of the particles

are extracted from the interference pattern, using the HoloSuite software package (Fugal et al., 2009; Schlenczek, 2018). The resulting 2D shadowgraphs can be classified as cloud droplets, ice crystals and artefacts based on a set of parameters using supervised machine learning (e.g., Fugal et al., 2009; Beck et al., 2017; Touloupas et al., 2019). In the present study, a set of around 7000 particles was classified manually, which served as a training data set on support vector machines. From the classification, the phase-resolved particle size distribution is computed. The particle diameter is calculated based on the number of pixels (see also Section 2.3.3) and the number concentration can be computed from the particle counts within the well-defined sample volume. Only particles that exceed a size of 2×2 pixels (6 µm) are considered. Moreover, because holography provides a snapshot of an ensemble of cloud particles, the spatial distribution of the cloud particles can be recovered from the interference pattern. Unlike light scattering instrumentation, no assumptions about the particle shape, orientation or refractive index are required, because an image of the cloud particles is recorded. The major disadvantage of holography is the high computational power associated with the reconstruction process and the data analysis. The working principle of digital in-line holography and HOLIMO has been described in more detail in Fugal et al. (2009), Henneberger et al. (2013) and Beck et al. (2017).

2.3.2 Instrument description

A series of holographic instruments have been developed in the Atmospheric Physics group at ETH Zurich in the last decade (Amsler et al., 2009; Henneberger et al., 2013; Beck et al., 2017). HOLIMO 3B consists of two main units: the control unit, which comprises the temperature control system and the control and data-acquisition computer, and the optical imaging unit, which is integrated in the two instrument towers. Like the previous version (HOLIMO 3G; Beck et al., 2017), HOLIMO 3B has an open-path configuration. In contrast to the previous versions, HOLIMO 3B uses a 355 nm laser and an improved optical system to enlarge the detection volume and improve the optical resolution of the instrument.

A schematic of the optical system of HOLIMO 3B is shown in Figure 2.2. The laser (FTSS355-Q4_1k, CryLaS, Germany) emits pulses with a wavelength of 355 nm, with a pulse width of 1.4 ns and a pulse energy of 42 µJ. The beam is attenuated by a neutral density filter and focused through a 10 µm diamond pinhole (Lenox Laser HP-3/8-DISC-DIM-10), which acts as a point light source. The diverging laser beam is expanded by a biconcave lens and collimated to a beam diameter of around 40 mm. After passing through a turning prism and a sapphire window, the collimated laser beam traverses the sample volume, before entering the imaging lens system in the opposite tower of the instrument. The bi-telecentric lens system (Correctal S5LPJ2755, TDL65/1.5 UV, Sill Optics, Germany) has a magnification of 1.5 and a numerical aperture of 0.13. The holograms are recorded with a 25 MP camera (hr25000MCX, SVS-Vistek, Germany) with 5120×5120 pixels, a pixel pitch of 4.5 µm and a maximum frame rate of 80 frames per second (fps). The quadratic cross-sectional area of the camera allows for more uniform illumination of the edges than a rectangular camera image, which was used in the previous versions. The optical resolution of the system was tested using a US Air Force resolution target (1951 USAF), which is placed at different positions inside the detection volume, following the procedure described in Spuler and Fugal (2011) and Beck et al. (2017). The optical system described achieves

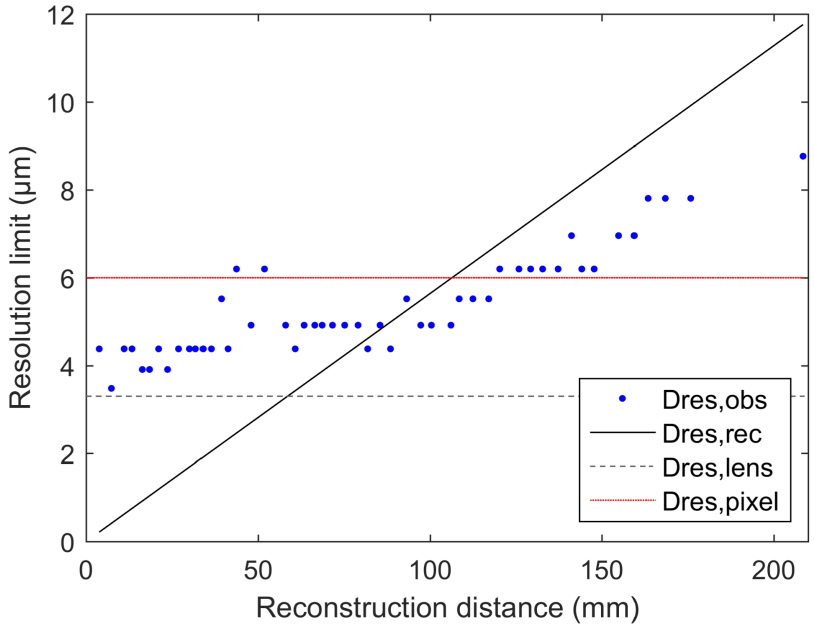

Figure 2.3: Optical resolution measurements of the HOLIMO 3B instrument as a function of the reconstruction distance. The blue dots represent the resolutions measured with a US Air Force resolution target 1951 USAF ($D_{res,obs}$). The three lines indicate theoretical resolution limits due to the pixel size ($D_{res,pixel}$, red solid line), the optical limitation of the lens system ($D_{res,lens}$, gray dashed line) and the optical setup of the instrument ($D_{res,rec}$, black solid line). The strongest resolution limit constraint determines the optical resolution of the instrument at a specific reconstruction distance. More information about the theoretical resolution constraints for holographic systems can be found in Henneberger et al. (2013) and Beck et al. (2017).

a resolution ($D_{res,obs}$) of 6 µm within the first 110 mm of the reconstruction distance (see Figure 2.3). This is consistent with the theoretical resolution limit of the pixel size ($D_{res,pixel}$). For reconstruction distances larger than 110 mm, the resolution limit decreases and is determined by the resolution limit from the diffraction aspects of in-line holography ($D_{res,rec}$). In general, the measured optical resolutions are in good agreement with the theoretical resolution constraints. Particles within the first 10 mm and close to the image border (< 0.2 mm from image edges) are not included in the analysis due to flow distortion effects from the towers and edge effects. With an effective cross-sectional area of 15 mm $\times$ 15 mm and an effective depth of 100 mm, this results in a sample volume of 22.5 cm^3 and a maximum sample volume rate of 1800 $cm^3 s^{-1}$ (with 80 fps).

2.3.3 Size calibration of HOLIMO 3B

Accurate sizing of cloud particles is important to obtain reliable measurements of cloud properties such as water content and size distributions. For holographic instruments, the sizing algorithm should be precise and accurate over a large particle size range (6 µm - 1 cm) and applicable for the entire detection volume. The sizing of the particles strongly depends on an amplitude threshold value that separates particle pixels from background pixels. From the number of particle pixels, the area-equivalent diameter is derived. In the standard HoloSuite version, a uniform amplitude threshold is used for particle detection and particle sizing. However, a uni-

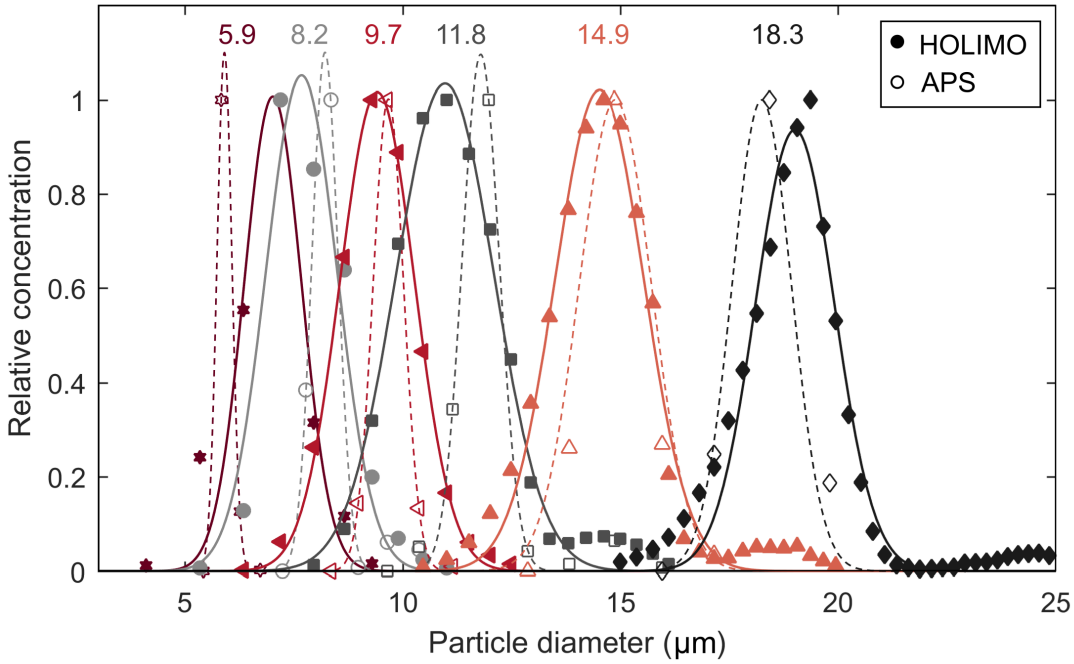

Figure 2.4: Size distributions from calibration experiments of the HOLIMO 3B instrument. The symbols show the normalized particle concentration measured by HOLIMO 3B (filled) and the APS (unfilled) instrument. The lines indicate the Gaussian distributions fitted to the HOLIMO 3B data (solid) and APS data (dashed). The numbers represent the mean diameter of the APS size distribution.

form amplitude threshold leads to unsatisfying results for particle sizing due to a decreasing signal-to-noise ratio with increasing reconstruction distance z in the large detection volume of HOLIMO 3B. This has the effect that the amplitude image of the particles becomes less distinct with larger z distances and thus the observed particle size decreases with increasing z distance. To overcome this issue and to ensure a uniform sizing of the particles over the entire detection volume, Beck (2017) introduced a new method by normalizing the in-focus particle image. In the normalization step, the darkest particle pixel is set to 0 (black), the mean of the background pixels is set to 1 (white) and the rest of the pixels are scaled relatively. This results in a more uniform signal-to-noise ratio and allows the application of a uniform amplitude threshold. The amplitude threshold can be used as a tuning parameter to calibrate the sizing algorithm of the HoloSuite software for the HOLIMO 3B instrument.

The sizing algorithm was calibrated using a vibrating orifice aerosol generator (VOAG model 3450, TSI, Minnesota, USA) for particle generation and an aerodynamic particle sizer (APS model 3321, TSI, Minnesota, USA) for particle sizing. Particles with diameters between 5 µm and 18 µm were generated by the VOAG using a liquid oil-water solution. The generated particles were introduced into a 120 mm × 1000 mm cylindrical tube and measured by the HOLIMO 3B instrument and an APS that were installed at the end of the tube. The APS covers the size range between 1 µm and 20 µm and is used as a reference measurement. The amplitude threshold was used as a tuning parameter to fit the HOLIMO 3B measurements to the APS measurements. An amplitude threshold of 0.47 was found to fit the APS data best (smallest sum of squared errors).

Table 2.1: Results of the size calibration experiments of HOLIMO 3B and an APS. The mean diameter and the standard deviation are derived from a Gaussian fit to the normalized size distribution.

	Particle diameter (µm)					
HOLIMO	7.02 ± 0.93	7.68 ± 1.15	9.41 ± 1.21	10.97 ± 1.59	14.52 ± 1.45	19.01 ± 1.28
APS	5.91 ± 0.24	8.21 ± 0.42	9.67 ± 0.50	11.79 ± 0.60	14.88 ± 1.18	18.25 ± 0.96

The size distributions of the calibration experiments are shown in Figure 2.4 and are summarized in Table 2.1.

The size distributions of the HOLIMO 3B and APS instruments were normalized to their maxima and a Gaussian distribution was fitted to the data. The results of the HOLIMO 3B instrument agree with the mean diameter of the APS within instrumental uncertainty. In general, a trend towards an underestimation of the particle diameter compared to the APS is observed, except for the calibration measurements at the measurement limits of HOLIMO 3B (6 µm) and the APS (18 µm). The overestimation of the particle diameter by HOLIMO 3B for 6 µm particles may be due to the optical resolution limit of the HOLIMO 3B instrument. While HOLIMO 3B can only detect particles larger than 6 µm, the APS can detect particles down to a diameter of 1 µm. On the other hand, the overestimation of the particle diameter at 18 µm could be caused by a bias of the APS instrument, which has an upper detection limit of 20 µm. Thus, particles in the second peak at 23 µm are not detected by the APS (see Figure 2.4). To conclude, no correction to the sizing algorithm was made, because all size measurements agree within the square root of the pixel size ($\sqrt{3.01\ \mu\text{m}} = 1.73\,\mu\text{m}$).

2.4 Case study - supercooled low stratus clouds

As a case study, we present observations of a supercooled low stratus cloud event (also referred to as high fog) during a Bise situation over the Swiss Plateau, obtained on 24 February 2018 between 08 UTC and 10 UTC. Bise is a typical weather situation in Switzerland during winter (Wanner and Furger, 1990). The case study focuses on nine vertical profiles of microphysical and meteorological cloud properties measured by the HoloBalloon platform. The analysis starts with an overview of the synoptic weather situation and the large-scale cloud structure and moves towards smaller scales, providing information about the cloud microstructure.

The Swiss Plateau, which lies between the Jura mountains and the Swiss Alps, is often covered by fog or low stratus clouds during fall and winter due to its geographic location. A satellite-based climatology of fog and low stratus cloud coverage over the Swiss Plateau during high-pressure situations in winter is shown in Figure 2.5. In regions along rivers and lakes, a fog frequency of up to 90 % is observed. Most commonly, fog forms by radiative cooling during clear nights. Additionally, cold air flows from the alpine valleys and the Jura towards the Swiss Plateau, where the cold air can accumulate. This cooling of the air can cause condensation and the formation of ground fog. However, the case study presented here was connected to a Bise situation; a cold, dry east / north-east wind. During Bise, cold air is advected and pushed under warm air, leading to the formation of a strong temperature inversion. The cold air in the lower layer cannot easily escape the Swiss Plateau because it is bound by the Jura mountains and the Swiss Alps. If the

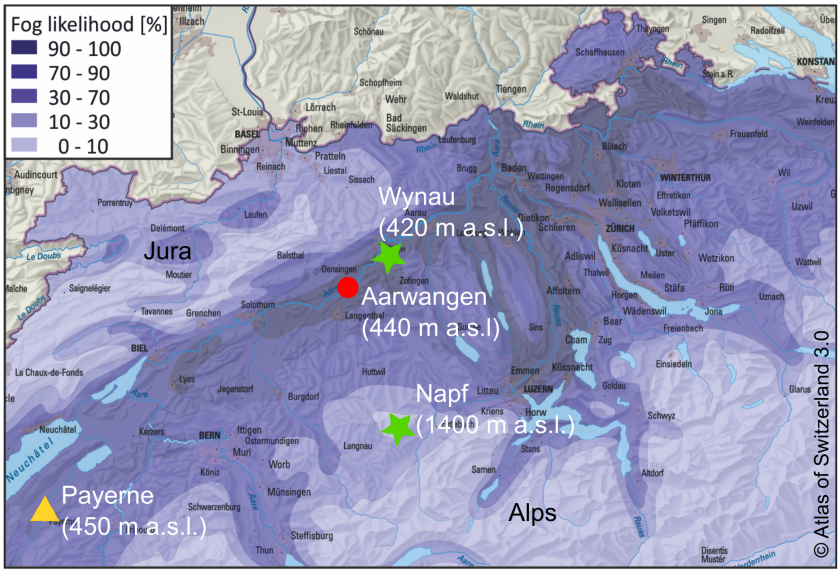

Figure 2.5: Map of the fog frequency during winter (adapted from the 'Atlas of Switzerland 3.0', 2010, `https://www.atlasderschweiz.ch/`, last access: 24 January 2020) and of the measurement locations. The climatology of fog is based on satellite images. The field locations include the measurement site in Aarwangen from which HoloBalloon was launched (red circle), ground-based weather stations from MeteoSwiss providing measurements of meteorological parameters (green stars) and the field site in Payerne from which radiosondes are launched twice a day (yellow triangle).

air is sufficiently moist, condensation sets in and fog or low stratus clouds can develop. The top of the cloud layer is defined by the height of the temperature inversion. The solar radiation reaching the boundary layer is often too weak to dissipate the fog layer in fall and winter. Thus, ground fog or stratus clouds can persist for several days, until a change in the synoptic weather pattern occurs.

2.4.1 Measurement location and data analysis

The measurements with the HoloBalloon platform were performed in Aarwangen (47°14' N, 7°45' E) in the Swiss Plateau 40 km northeast of Bern (Figure 2.5). The field site is located at a gravel station next to the Aare river at an altitude of 440 m a.s.l. and is surrounded by grassland and forests. The balloon measurements were performed in a temporarily closed air space of 2 km in diameter, which was activated on measurement days. The maximum flight height allowed was 700 m above ground because of air traffic regulations. The experimental setup of the HoloBalloon platform is shown in Figure 2.1.

The measurements taken on the HoloBalloon platform were complemented and validated by observations of surrounding MeteoSwiss weather stations and radiosondes (see Figure 2.5). The weather stations are located within a radius of 30 km from Aarwangen and cover altitudes between 420 m a.s.l. and 1400 m a.s.l. Radiosondes are launched twice a day (00 UTC and 12 UTC) from Payerne, which is located 80 km southwest of Aarwangen. We used the radiosondes to determine the inversion and cloud top height, because we were not able to measure the whole cloud layer due to the air traffic restrictions on flight height.

A total of nine vertical profiles measured with the HoloBalloon platform were analyzed in this

Table 2.2: Summary of the start and end time of the nine vertical profiles observed with the HoloBalloon platform.

Profile number	Profile type	Start time (UTC)	End time (UTC)
1	ascending	08:01	08:10
2	descending	08:11	08:23
3	ascending	08:24	08:34
4	descending	08:35	08:45
5	ascending	08:46	08:58
6	descending	08:59	09:11
7	ascending	09:12	09:22
8	descending	09:23	09:37
9	ascending	09:38	09:57

case study, with an average of 800 holograms (~ 5 L sampled volume) or 600'000 cloud particles per profile. The battery of the instrument package was empty after profile 9; thus no observations were available afterwards. Each profile had a duration of 10-15 minutes. With a mean horizontal wind speed of $10\,\mathrm{m\,s^{-1}}$, this results in a horizontal resolution of around 6-9 kilometers. The start and end times of the individual profiles are summarized in Table 2.2. At least 10 holograms were grouped together to obtain better counting statistics. This results in a vertical resolution of 5 m. Only data points with a liquid water content (LWC) larger than $0.01\,\mathrm{gm^{-3}}$ (definition for cloud base) are considered in the analysis. Cloud particles smaller than 25 µm were classified into the three categories of cloud droplets, ice crystals and artifacts using support vector machines (see Section 2.3.1), whereas particles larger than 25 µm were classified manually (visual classification). Only particles within a reconstruction distance between 20 mm and 50 mm were included in the analysis. A smaller detection volume than described in Section 2.3.2 was chosen due to the mean droplet size being close to the instrumental resolution limit and noise in the holograms.

2.4.2 Meteorological situation

Figure 2.6 shows vertical profiles of the meteorological parameters during the measurement period. The meteorological conditions during the 2-hour measurement period were relatively stable. The temperature profile was characterized by a strong temperature inversion, which was located at around 1450 m a.s.l. The temperature varied between -1 °C at the surface and -8.9 °C at the inversion base. The height of the temperature inversion defines the top of the cloud layer. The relative humidity increased from the ground up to 850 m a.s.l., where it remained constant up to the inversion. We assumed that this constant relative humidity interval indicates conditions of water saturation and thus marks the extent of the cloud layer. No relative humidity values above 95 % were observed by the HoloBalloon platform. This can be explained by the challenges of measuring relative humidity at in-cloud conditions (e.g., Korolev and Mazin, 2003; Korolev and Isaac, 2006). Wind speeds between $6.7\,\mathrm{m\,s^{-1}}$ and $8.6\,\mathrm{m\,s^{-1}}$ were observed in Wynau with wind gusts up to $10.6\,\mathrm{m\,s^{-1}}$. The wind speed in Aarwangen increased in the first 200 m above the ground from $7\,\mathrm{m\,s^{-1}}$ to $10\,\mathrm{m\,s^{-1}}$. As it can be seen from the radiosondes, the wind speed was relatively constant up to the inversion layer. The prevailing wind direction was northeast with

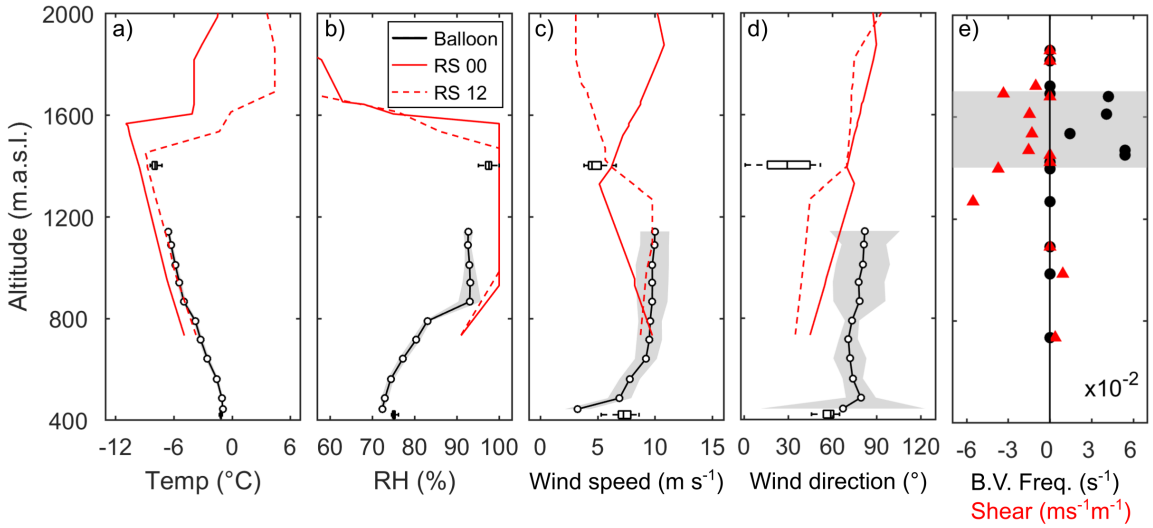

Figure 2.6: Vertical profiles of the meteorological parameters (a-d). The HoloBalloon measurements are averaged over nine profiles and an altitude interval of 75 m. The black dots indicate the mean and the shaded area the standard deviation of the data. The vertical profiles of two radiosonde ascents (00 UTC (solid) and 12 UTC (dashed)) are shown by the red lines. The box plots represent the data from MeteoSwiss weather stations (Wynau (420 m a.s.l.), Napf (1400 m a.s.l.)). In each box, the central line indicates the median and the left and right edges of the box mark the 25th and 75th percentiles, respectively. The whiskers extend to the minimum and maximum of the data not considered as outliers. Panel (e) shows the vertical profile of the Brunt-Väisälä frequency ($N = \sqrt{\frac{g}{\theta}\frac{\delta\theta}{\delta z}}$) and the wind shear ($s = \frac{\delta v}{\delta z}$) calculated from the radiosonde ascent at 12 UTC. The shaded area in Figure 2.6e indicates regions with a positive Brunt-Väisälä frequency.

a slight turn towards east with increasing altitude. At the inversion, a change in the horizontal wind speed and direction with height (vertical wind shear) occurs. In this region, a positive Brunt-Väisälä frequency N is observed (Figure 2.6.e). These conditions are favorable for the development of boundary layer waves and Kelvin-Helmholtz instability (see Section 2.4.4).

2.4.3 Microphysical cloud structure

Figure 2.7 shows the mean vertical profiles of the microphysical cloud properties averaged over nine profiles. The mean cloud droplet number concentration (CDNC) increases from 10 cm^{-3} at the cloud base (920 m) to 150 cm^{-3} at 1100 m (Figure 2.7a). The mean liquid water content (LWC) ranges between 0.01 gm^{-3} and 0.08 gm^{-3} and on average approaches an adiabatic profile (Figure 2.7b). The mean cloud droplet diameter increases from 9 µm to 9.5 µm between the cloud base and 1000 m and stays constant above (Figure 2.7c). The observed CDNC of 150 cm^{-3}, LWC of 0.08 gm^{-3} and mean cloud droplet diameter of 9.5 µm are in the observed range for fog and continental stratus clouds (Lohmann et al., 2016b), but rather at the lower end of the range. Despite the supercooled conditions, only a few ice crystals were observed ($< 1\,L^{-1}$).

The increase in CDNC with increasing height is in contrast to the theory of an adiabatic cloud profile and might be explained by different factors. An adiabatic cloud model assumes that cloud droplets activate at the cloud base and grow in size with increasing altitude. Thus, CDNC is expected to remain constant with height after the maximum supersaturation is reached. There

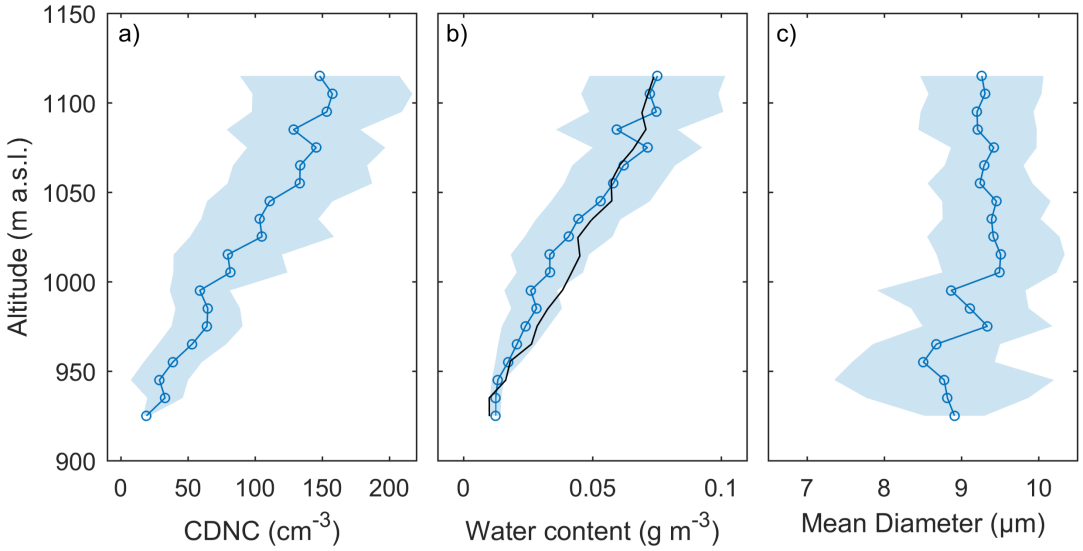

Figure 2.7: Mean vertical profiles of the cloud droplet number concentration (a), liquid water content (b) and mean cloud droplet diameter (c) averaged over the nine profiles measured with the HoloBalloon platform. The data are averaged over an altitude interval of 10 m. The shaded area represents the standard deviation. The black line in b) shows the adiabatic LWC profile w_{l_ad}, which is obtained as follows: i) calculate the saturation vapor pressure e_s at the cloud base, ii) use the pressure at the cloud base to determine the saturation mixing ratio $w_s(T,p) = \frac{\epsilon e_s(T)}{p - e_s}$, iii) calculate $w_t = w_s + w_l$ at the cloud base assuming $w_l = 0.01\,\mathrm{g\,kg^{-1}}$ and assuming constant w_t with height (adiabatic), and iv) calculate w_s at all height levels, determine w_l and multiply w_l by local dry air density to obtain w_{l_ad}.

are several possibilities why this theoretical concept is not applicable for the case study presented here. Firstly, HOLIMO 3B does not detect cloud droplets smaller than 6 µm. This can lead to an underestimation in CDNC, especially at cloud base where the droplets are smallest. Secondly, an adiabatic cloud model assumes a constant updraft, but fluctuations in the updraft speed or turbulence could generate supersaturated conditions and activate cloud droplets at higher altitudes than cloud base. Thirdly, the increase in CDNC with height could be driven by radiative cooling at the cloud top by producing either supersaturation or instabilities and thus turbulence within the cloud layer. On the other hand, a database of stratus clouds (Miles et al., 2000) showed that the CDNC in continental clouds was more variable with height than in marine clouds where CDNC was determined near cloud base. Therefore, it is unclear whether the observed increase in CDNC is a measurement artifact or a real feature of the observed cloud. Regardless, we recommend that future balloon-borne measurements of clouds include instruments capable of measuring even the smallest cloud particles.

2.4.4 Inhomogeneities in the microphysical cloud properties of stratus clouds

Upon further analysis, we investigate cloud inhomogeneities in stratus clouds on different scales and discuss potential physical processes, which could influence these cloud signatures. In the present study, cloud inhomogeneities are defined by the variability in the CDNC. Therefore, we introduce the term CDNC anomaly ($\mathrm{CDNC}'_{\mathrm{h}}$), which describes the variability of the CDNC

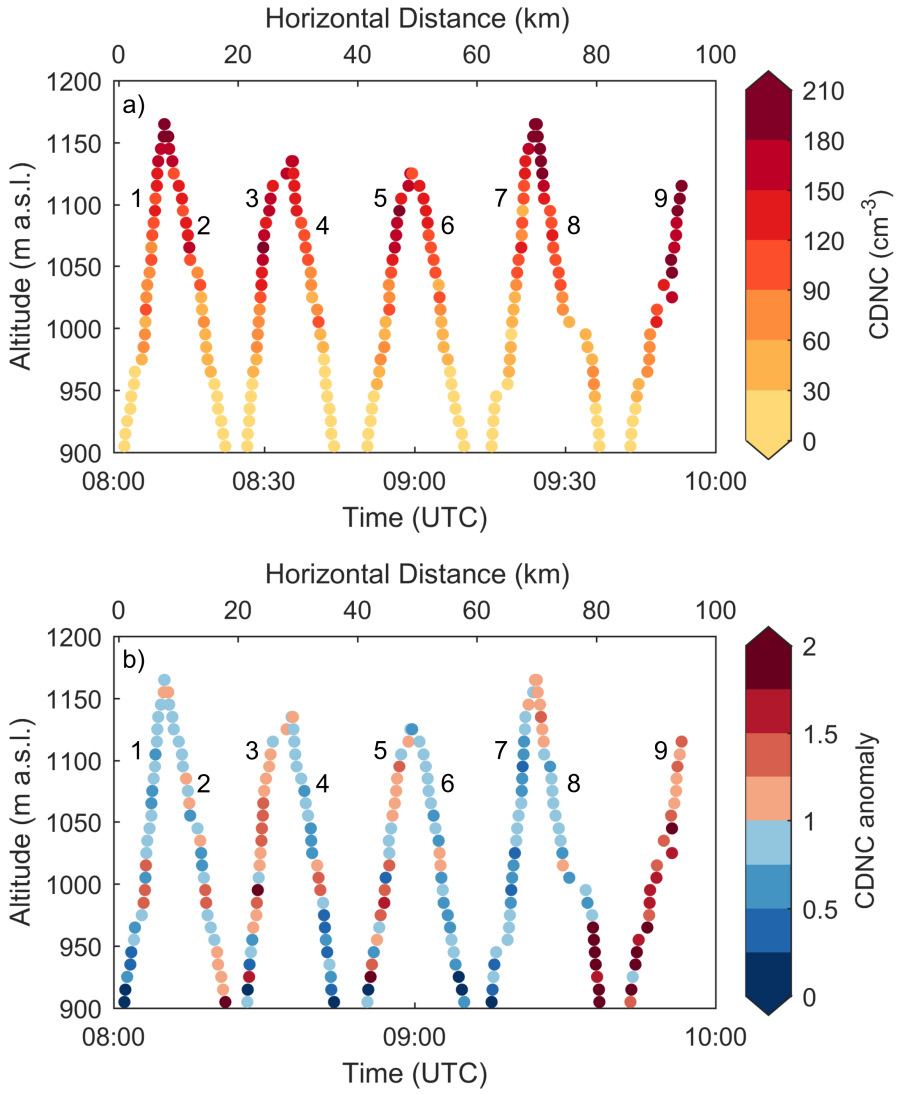

Figure 2.8: Height-temporal evolution of the CDNC (a) and the CDNC anomaly ($CDNC_h^a$, b) (see text for explanation of anomaly). The data points are averaged over an altitude interval of 10 m. The upper x-axis shows the horizontal distance s of the cloud, assuming a mean wind speed v of 10 m s^{-1} over time t ($s = v \cdot t$). The numbers represent the profile number according to Table 2.2.

over a given height interval h. The $CDNC_h^a$ is calculated by dividing the CDNC observed in the height interval h ($CDNC_h$) by the mean CDNC in that height interval averaged over the nine profiles ($\overline{CDNC_h}$) (i.e. $CDNC_h^a = CDNC_h / \overline{CDNC_h}$). As Korolev and Mazin (1993), we define areas with $CDNC_h^a < 0.5$ as regions of decreased CDNC and areas with $CDNC_h^a > 1.5$ as regions of increased CDNC.

The height-temporal evolution of the CDNC and $CDNC_h^a$ is shown in Figure 2.8. $CDNC_h^a$ reveals areas of increased and decreased CDNC (Figure 2.8b). For example, profile 7 shows regions of decreased CDNC, whereas profile 9 shows regions of increased CDNC compared to the mean profile. The CDNC at 1100 m in profile 9 (200 cm^{-3}) is more than a factor of 3 higher than in profile 7 (60 cm^{-3}). From a single profile perspective, all profiles show alternating regions of higher and lower CDNC. It is likely that the observed variations in CDNC exceed statistical variations and are the result of different physical processes.

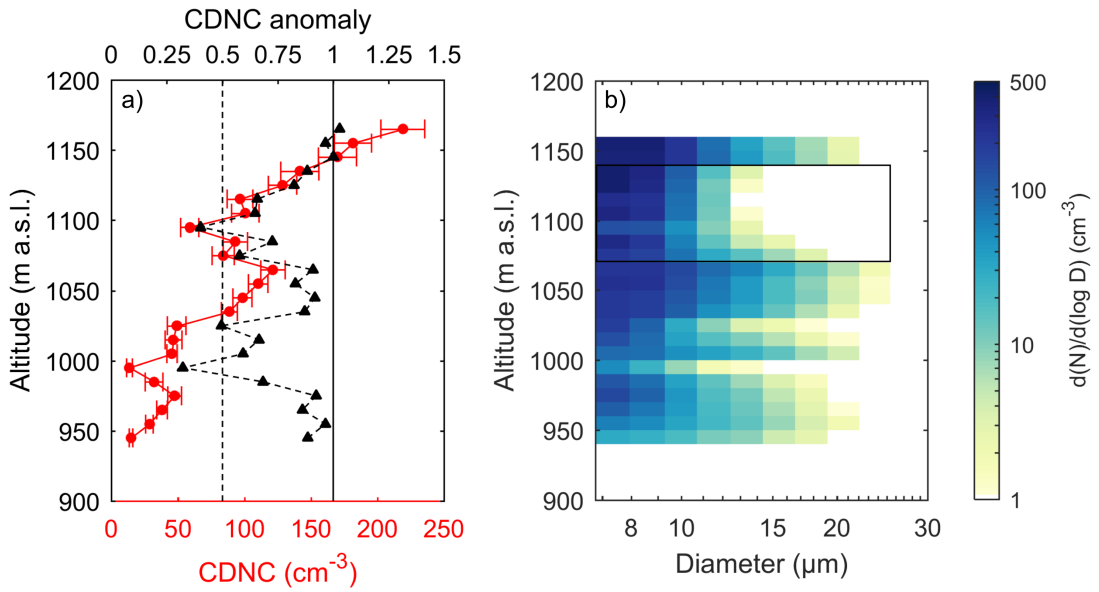

Figure 2.9: Vertical profile of CDNC (in red) and CDNC anomaly (in black, $CDNC_h^a$) (a) and number size distribution (b) of profile 7. To the left of the dashed vertical line in panel (a), $CDNC_h^a$ is less than 0.5. The data are averaged over a 10 m interval. The black rectangle in panel (b) shows the region of decreased CDNC (discussed in text).

The variability in CDNC on a scale of several kilometers might be explained by the presence of boundary layer waves. Boundary layer waves can cause entrainment of dry air into the cloud (Mellado, 2017) and could affect the cloud structure (e.g., Bergot, 2013). As discussed for example by Wanner and Furger (1990), strengthening or weakening of the Bise due to dynamic effects could induce oscillations within the cold air and lead to the formation of boundary layer waves at the cloud top. The presence of wind shear and a positive Brunt-Väisälä frequency ($N = 0.04\,s^{-1}$) at the inversion (see Figure 2.6e) represent favorable conditions for the formation of Kelvin-Helmholtz instability and boundary layer waves. However, in order to further test this hypothesis, microphysical observations up to cloud top and an extended set of auxiliary measurements (e.g., three-dimensional wind field, turbulence) over a time period of several hours would be necessary.

Inhomogeneities in CDNC on a meter scale can be the result of different processes, depending on their location within the cloud. We will discuss these cloud inhomogeneities based on profile 7, because it has $CDNC_h^a$ below 1 almost everywhere (see Figure 2.8b). Profile 7 shows a gradual increase in cloud droplet size and number concentration with height until a sudden decrease in particle concentration and cloud droplet size occurs between 1070 m and 1130 m (Figure 2.9b). In this region, CDNC is less than half of the average CDNC ($CDNC_h^a < 0.5$, Figure 2.9a). In addition, the cloud droplet spectrum shows an increase in small droplets and an absence of cloud droplets larger than 14 µm. Korolev and Mazin (1993) propose several mechanisms for the formation of cloud inhomogeneities on a meter scale such as (i) entrainment, (ii) variability of the condensation level and (iii) evaporation in descending motions. Considering the location of our region of decreased CDNC (300-400 m from cloud top, 200 m from cloud base), we assume that this $CDNC_h^a$ below 1 is most likely formed by evaporation in descending motions. The temperature inside a descending air parcel increases due to adiabatic compression and heating,

and in response cloud droplets, evaporate leading to regions of decreased CDNC. However, more sophisticated analyses of turbulence and microphysical observations up to cloud top are required to further investigate these cloud inhomogeneities and the corresponding physical processes, which is beyond the scope of this study.

2.5 Discussion

2.5.1 Validation of the HoloBalloon platform and further improvements

The HoloBalloon platform was successfully deployed in various meteorological conditions. In situ profiles up to 700 m altitude above the ground were obtained, limited by air traffic restrictions in the maximum altitude. Unfortunately, because of this limitation in the maximum altitude, we were not able to penetrate the whole cloud layer and perform measurements at the cloud top. The platform was deployed at temperatures down to -8 °C. Despite the supercooled conditions, we observed only a few ice crystals ($<1\,\mathrm{L}^{-1}$). Even though parts of the balloon and of the cable were covered in ice, this did not affect our measurements and the flight performance. However, based on our experience, we recommend covering the balloon with a tarp at night to prevent accumulation of snow and water on the balloon. We flew the TBS in wind speeds up to $15\,\mathrm{m\,s}^{-1}$. The TBS was stable in these high wind conditions, but the ground handling became challenging at wind speeds above $10\,\mathrm{m\,s}^{-1}$, especially in the presence of wind gusts.

For setting up and operating the HoloBalloon platform, several aspects need to be considered. Firstly, a closed air space was required to perform cloud measurements with a TBS. The process of obtaining a closed air space was closely coordinated with the aviation safety authority. In areas with dense air traffic, such as the Swiss Plateau, it can be difficult to find a suitable location. Secondly, a large, reasonably flat surface area ($\sim$20 m$\times$40 m) is required to prepare and launch the TBS. No major obstacles (e.g., trees, power lines) should be within a radius of around 60 m of the launching site and it should be possible to insert an anchor into the ground. The system set up takes approximately 3 days and requires two to three trained persons for operation. A third person can especially be helpful during difficult wind conditions.

HoloBalloon was able to measure temperature, relative humidity and wind profiles in boundary layer clouds. In general, the measurements agreed well with the observations from the MeteoSwiss weather stations and the radiosondes (see Figure 2.6). The temperature sensor showed a delayed response to changes in the ambient temperature (not shown), similarly to what was observed by Beck et al. (2017) on the cable car platform HoloGondel. To overcome this issue, the temperature was calculated from the virtual temperature of the 3D sonic anemometer, assuming water saturation in the cloud. It is well known that it is difficult to measure relative humidity in clouds (e.g., Korolev and Mazin, 2003; Korolev and Isaac, 2006). The relative humidity measured by the HoloBalloon platform in clouds ranged between 93 % and 98 %. We assumed in-cloud conditions when the relative humidity remained constant with height. Wind speed and direction measurements of the 3D sonic anemometer were corrected for the motion of the balloon. As described in Section 2.2, this was done using the output from an inertial navigation system and a GPS antenna following the procedure described in Elston et al. (2015). The corrected horizontal wind speed and wind direction measurements agreed well with the

radiosonde observations. Vertical wind speed and turbulence measurements were not considered in this study, because we cannot exclude an influence from the balloon on the turbulence measurements, as the instrument package was installed on the keel below the balloon (Figure 2.1). For future field campaigns, we will install the instrument package 20-30 m below the balloon in order to minimize potential influences from the balloon and to also analyze turbulence data of the 3D sonic anemometer. The feasibility of a hanging mount was already successfully tested in the field in the fall of 2019.

The vertical profiles of the microphysical measurement showed no systematic difference between ascending and descending profiles (see Figure 2.8b), suggesting that the balloon was not significantly influencing the microphysical measurements themselves. With a mean horizontal wind speed of $10\,\mathrm{m\,s^{-1}}$ and a cable speed of $1\,\mathrm{m\,s^{-1}}$, the horizontal wind speed is by a factor 10 larger than the cable speed. This, in combination with a flight angle of up to 45° (due to the kytoon design), minimizes shading effects and further supports the assumption that a 'pristine' cloud volume is measured.

Generally, the measured size distributions during the present case study showed the maximum number concentration close to the resolution limit of HOLIMO 3B. This demonstrates the limits of the instrument in measuring small cloud particles ($< 6\,\mu\mathrm{m}$). This bias can lead to an underestimation of CDNC, especially close to cloud base or in fog or clouds with a small mean cloud droplet diameter. For future field campaigns, we will equip the HoloBalloon platform with an optical particle counter in order to cover the entire cloud droplet size distribution.

2.5.2 Using the HoloBalloon platform to study boundary layer clouds

The potential of the HoloBalloon platform in studying boundary layer clouds is summarized in a conceptual picture (Figure 2.10), which is described with the help of the presented case study. Based on the research questions, different analysis strategies can be applied. Firstly, by analyzing a series of vertical profiles, the HoloBalloon platform can investigate the temporal and spatial evolution of cloud properties on a kilometer scale (Figure 2.10, top row). A vertical profile of 500 m can be accomplished within 8 minutes. Thus, a vertical profile can be obtained faster than with an aircraft. Secondly, individual profiles obtained with the HoloBalloon platform can provide information about the vertical cloud structure (Figure 2.10, middle row). With a sample rate of up to 80 fps and an aspiration speed on the order of $10\,\mathrm{m\,s^{-1}}$, the HoloBalloon platform can provide high-resolution measurements on the meter scale. We found that stratus clouds can exhibit complex dynamic structures with microphysical signatures on different scales (Section 2.4.4). For example, we observed a large variability in the CDNC and cloud droplet size within the stratus cloud. More sophisticated analyses of numerous cloud cases are required to further investigate cloud inhomogeneities and their physical implications. However, no generalization was possible in this study.

Furthermore, the analysis of individual holograms, or more specifically the analysis of the spatial distribution of an ensemble of cloud particles in the sample volume (Figure 2.10, bottom row), allows the study of small-scale processes and particle-particle interactions. For example, a spatial distribution analysis can provide insights into the physical nature of the interface between cloudy and ambient air and thus can be used to study entrainment and turbulent mixing at the

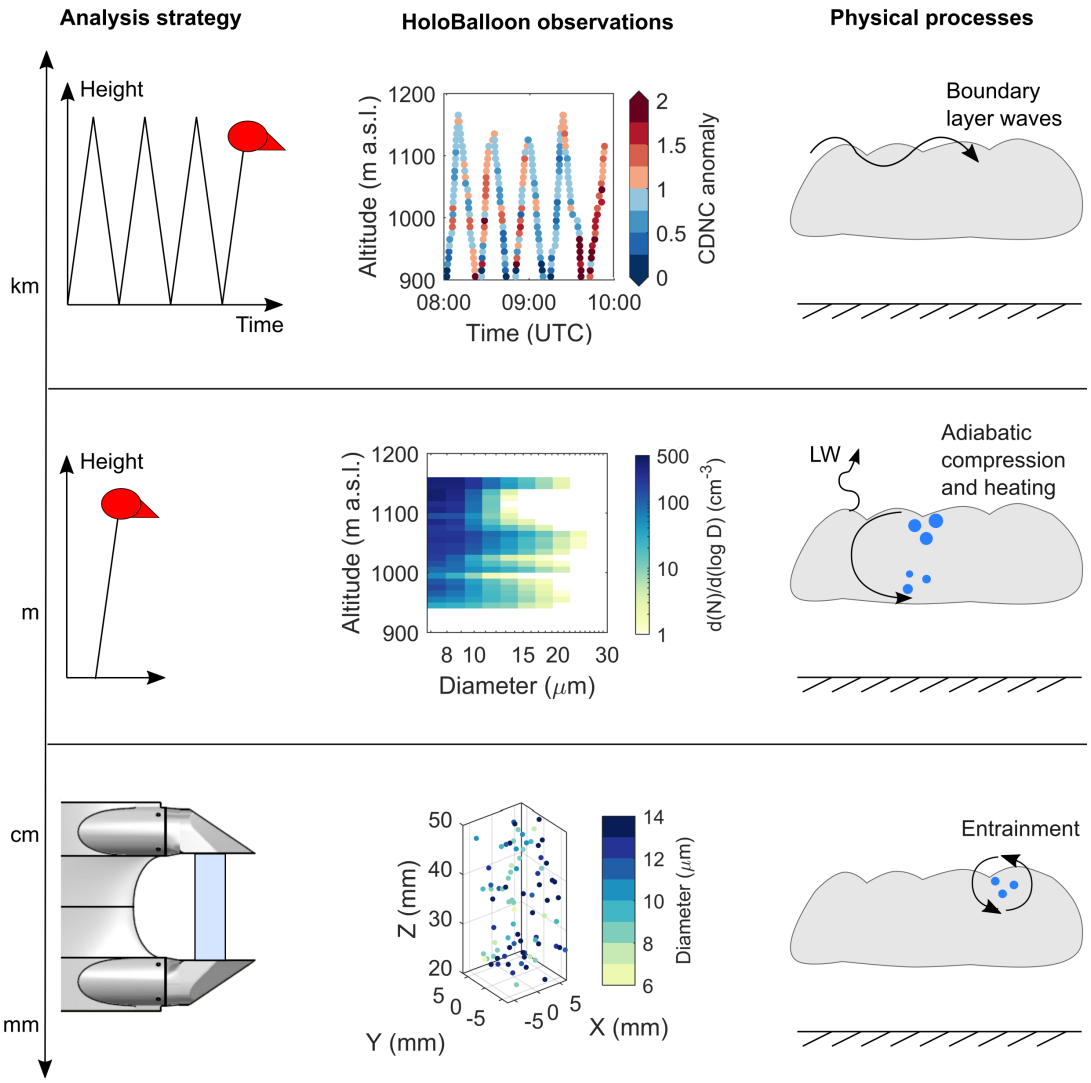

Figure 2.10: Conceptual picture describing the potential of the HoloBalloon platform in studying boundary layer clouds. It shows the scale-dependent analysis strategy (left), exemplary HoloBalloon observations of the presented case study (center) and possible physical processes that can be studied with the HoloBalloon platform (right). The scale-dependent analysis strategies include the analysis of a series of vertical profiles (top), a single vertical profile (middle) and a single hologram (bottom).

cloud top. However, a quantitative analysis of the spatial distribution (e.g., Larsen and Shaw, 2018; Larsen et al., 2018) is required to assess these small-scale processes, which is beyond the scope of this study. Future work will focus on the spatial distribution of cloud particles.

The HoloBalloon platform can be used to study processes over a wide range of scales from the kilometer down to the millimeter scale. However, the present case study also revealed some limitations of the HoloBalloon platform. For example, the vertical profiles are limited by the cable length (1200 m) or air traffic regulations regarding the maximum flight height (700 m) and it can only observe the cloud properties along the measurement path. In order to obtain a more comprehensive understanding of boundary layer clouds, a multidimensional set of instruments would be necessary. For example, the HoloBalloon measurements could be complemented by remote sensing instruments (e.g., cloud radar), which can provide continuous information of the large-scale cloud structure. Moreover, a wind profiler could be used to characterize the three-

dimensional wind field and to identify dynamical patterns such as boundary layer waves. Such a multi-scale approach could help to improve the microphysical and dynamical understanding of boundary layer clouds in future field campaigns.

2.6 Conclusions

In this study, we have introduced the newly developed measurement platform HoloBalloon and have shown its ability and potential in studying boundary layer clouds. Here, we presented in situ observations of a supercooled low stratus cloud during a Bise event over the Swiss Plateau in February 2018. Our main findings are summarized as follows:

- HoloBalloon merges the advantages of holography with the benefits of a TBSs. Unlike other single particles measurement techniques, holographic cloud imagers have a well-defined sample volume independent of particle size and air speed despite fluctuating aspiration speeds on a TBS. The low aspiration speed on the TBS in combination with the high acquisition rate of HOLIMO 3B allows for measurements with high spatial resolution.
- The HoloBalloon platform was successfully deployed at temperatures down to -8 °C and wind speeds up to $15\,\mathrm{m\,s^{-1}}$. While conventional blimp-like TBS are limited to wind speeds below $10\,\mathrm{m\,s^{-1}}$, kytoons are designed for wind speeds up to $25\,\mathrm{m\,s^{-1}}$, making them an interesting measurement platform for atmospheric research.
- HoloBalloon was able to reliably measure in situ vertical profiles of the microphysical cloud properties and meteorological parameters up to 700 m above ground. The meteorological measurements agreed well with observations from radiosondes and weather stations, and the observed cloud properties were within the expected range for fog and stratus clouds. Cloud particles between 6 µm and 24 µm and CDNC up to $200\,\mathrm{cm^{-3}}$ were observed with HOLIMO 3B.
- HoloBalloon was able to capture cloud inhomogeneities on different scales. For example, we observed a large variability in the CDNC and mean cloud droplet diameter from a kilometer down to a meter scale. We hypothesize that boundary layer waves and droplet evaporation in a descending air parcel might have influenced the cloud structure. However, further analyses are required to investigate these hypotheses. Moreover, HOLIMO 3B is capable of measuring the spatial distribution of an ensemble of cloud particles on a millimeter scale (e.g., Beals et al., 2015; Beck et al., 2017). This outstanding feature of holography allows studying processes on the particle scale such as entrainment, turbulent mixing or cloud particle growth.
- For future balloon-borne cloud measurements we recommend installing the instrument package 20 - 30 m below the balloon to reduce potential influences from the balloon on the cloud and turbulence measurements. In addition, we recommend that instruments covering the entire cloud particle spectrum are installed to accurately capture cloud activation and entrainment.

Data availability

Pre-processed data are available for download at `https://doi.org/10.5281/zenodo.3608035`. The raw hologram data are available from the authors on request.

Acknowledgments

The authors would like to thank Jörg Wieder for his assistance during the size calibration experiments and Julie Pasquier for the analysis of the resolution measurement. We also thank Hannes Wydler and Michael Rösch for their technical support in designing the HoloBalloon platform. The authors also thank the Kieswerk Risi and the Gemeinde Aarwangen for their excellent support during the field campaign. We would also like to thank the Federal Office of Civil Aviation (FOCA) for their assistance in getting the flight permit. The meteorological measurements were provided by the Swiss Federal Office of Meteorology and Climatology MeteoSwiss.

Financial support

This research has been supported by the ETH Scientific Equipment Program (grant no. 0-43034-17).

Chapter 3

Influence of low-level blocking and turbulence on the microphysics of a mixed-phase cloud in an inner-Alpine valley

F. Ramelli[1], J. Henneberger[1], R. O. David[2], A. Lauber[1], J. T. Paquier[1], J. Wieder[1], J. Bühl[3], P. Seifert[3], R. Engelmann[3], M. Hervo[4] and U. Lohmann[1]

[1] Department of Environmental System Sciences, Institute for Atmospheric and Climate Science, ETH Zurich, Zurich, Switzerland
[2] Department of Geosciences, University of Oslo, Norway
[3] Leibniz Institute for Tropospheric Research, Leipzig, Germany
[4] Federal Office of Meteorology and Climatology MeteoSwiss, Payerne, Switzerland

This manuscript is in review for Atmospheric Chemistry and Physics.
DOI: https://doi.org/10.5194/acp-2020-774

Abstract

Previous studies that investigated orographic precipitation have primarily focused on isolated mountain barriers. Here we investigate the influence of low-level blocking and shear-induced turbulence on the cloud microphysics and precipitation formation in a complex inner-Alpine valley. The analysis focuses on a mid-level cloud in a post-frontal environment, by combining observations from an extensive set of instruments including ground-based remote sensing instrumentation, in situ instrumentation on a tethered balloon system and ground-based precipitation measurements.

During this event, the boundary layer was characterized by a blocked low-level flow and a turbulent shear layer, which separated the blocked layer near the surface from the stronger cross-barrier flow aloft. Cloud radar observations indicate changes in the microphysical cloud properties within the turbulent shear layer including enhanced linear depolarization ratio (i.e., change in particle shape) and increased radar reflectivity (i.e., enhanced ice growth). Based on the ice particle habits observed at the surface, we suggest that needle growth and aggregation occurred within the turbulent layer and that collisions of fragile ice crystals (e.g., dendrites, needles) might have contributed to secondary ice production.
Additionally, in situ instrumentation on the tethered balloon system observed the presence of a low-level feeder cloud above a small-scale topographic feature, which dissipated when the low-level flow turned from a blocked to an unblocked state. Our observations indicate that the low-level blocking (due to the downstream mountain barrier) caused the low-level flow to ascend the leeward slope of the local topography in the valley, thus producing a low-level feeder cloud. Although the feeder cloud did not enhance precipitation in the present case, we propose that local flow effects such as low-level blocking can induce the formation of feeder clouds in mountain valleys and on the leeward slope of foothills upstream of the main mountain barrier, where they can act to enhance orographic precipitation through the seeder-feeder mechanism.

3.1 Introduction

Mountains can alter and reorganize incoming weather systems or force air masses to lift and thus produce a large proportion of the Earth's annual precipitation (Roe, 2005). Besides the total amount of precipitation, also its spatial distribution across the mountain range becomes of increasing importance for public warning (e.g., avalanche, flash flood), water resources, hydropower production and winter tourism (Stoelinga et al., 2013). In addition to orographic lifting and the subsequent production of condensate, additional processes are required to efficiently form precipitation-sized particles within the lifetime of the cloud as it crosses the mountain barrier (e.g., Smith, 1979; Frei and Schär, 1998; Roe, 2005; Houze Jr, 2012; Smith, 2019). As such, an extensive knowledge of these physical processes and the interplay between dynamics, microphysics and orography is essential to understand precipitation formation over complex terrain.
Numerous mechanisms have been identified to affect the air flow and enhance orographic precipitation (e.g., Borys et al., 2003; Rotunno and Houze, 2007; Lowenthal et al., 2011; Houze Jr, 2012; Medina and Houze Jr, 2015; Kirshbaum et al., 2018; Smith, 2019). For example, if the air flow impinging on a mountain barrier is sufficiently weak, or the mountain barrier is too high or the atmosphere is stably stratified, the low-level flow might be blocked or diverted around the mountain. As a consequence, a stagnant blocked layer can form in front of the mountain barrier, which extends the effective width of the mountain barrier and causes lifting further upstream (e.g. Rotunno and Ferretti, 2001; Medina and Houze, 2003; Jiang and Smith, 2003). Additionally, a layer of strong shear is usually present at the interface between the blocked layer and the strong cross-barrier flow aloft, which can be the source of turbulent motions. This shear-induced turbulent layer can enhance orographic precipitation (e.g. Houze Jr and Medina, 2005; Medina et al., 2005; Medina et al., 2007) and will be the focus of the present study.
Besides the dynamical response of the air flow to the orography, a wide range of microphysical

interactions can occur between cloud droplets, ice crystals and water vapor. For example, individual ice crystals can grow by vapor deposition, can collide and stick together with other ice crystals (aggregation) or can collide with supercooled cloud droplets that freeze upon contact (riming) (e.g. Pruppacher and Klett, 1980; Lohmann et al., 2016b). Turbulence and updrafts can accelerate ice growth by riming and aggregation and thus precipitation fallout, by sustaining the production of supercooled liquid water (Rauber and Tokay, 1991) and by increasing the collision efficiencies between cloud particles (Pinsky et al., 2016a). Furthermore, enhanced ice-ice collisions can promote mechanical break-up of ice crystals and lead to the production of a large number of small secondary ice particles (e.g., Vardiman, 1978; Yano et al., 2016).

In the present study, we investigate the influence of low-level blocking and shear-induced turbulence on the microphysics and precipitation formation of a mixed-phase cloud in an inner-Alpine valley. Previous studies found that flow blocking and shear-induced turbulence can facilitate rapid ice growth and ultimately enhance orographic precipitation (e.g., Marwitz, 1983; Overland and Bond, 1995; Yu and Smull, 2000; Hogan et al., 2002; Neiman et al., 2002; Neiman et al., 2004; Houze Jr and Medina, 2005; Loescher et al., 2006; Olson et al., 2007; Olson and Colle, 2009; Geerts et al., 2011; Medina and Houze Jr, 2015; Grazioli et al., 2015; Aikins et al., 2016). For example, turbulent updraft cells were observed over the Oregon Cascade Mountains in regions where the wind shear exceeded $10\,\mathrm{m\,s^{-1}\,km^{-1}}$ (Houze Jr and Medina, 2005). Houze Jr and Medina (2005) suggested that these turbulent updraft cells can enhance ice growth through riming and aggregation. Both mechanisms can lead to rapid conversion of condensate to precipitation-sized particles. More recent studies confirmed the findings by Houze Jr and Medina (2005) that turbulent updraft cells enhance ice growth and precipitation (e.g., Medina and Houze Jr, 2015; Geerts et al., 2011; Aikins et al., 2016). However, Geerts et al. (2011) could not draw any conclusions regarding the dominant ice growth processes, due to restrictions in the aircraft flight level. On the other hand, Aikins et al. (2016) proposed depositional growth and aggregation as the dominant ice growth mechanisms for their study rather than riming due to the low amounts of liquid water observed in the shear layer. Thus, the dominant growth process within shear-induced turbulent layers depends on the environmental conditions such as temperature, updraft velocity and the ice crystal size distribution.

The present work builds on the previous studies that investigated the implications of shear-induced turbulence on the cloud microphysics and precipitation formation and extends the analysis to a more complex terrain. While previous observational studies have mainly focused on the effect of an isolated mountain barrier, we will investigate the role of shear-induced turbulence in an inner-Alpine valley near Davos, Switzerland. The region around Davos, or more generally the Alpine region, is characterized by complex terrain with narrow valleys and multiple mountain barriers, which can cause complex interactions between numerous mechanisms on different scales. This complexity has already been recognized during the Mesoscale Alpine Programme (MAP) (e.g., Rotunno and Houze, 2007). In an environment with a series of parallel mountain ridges, a superposition of upstream and downstream effects can occur. In the present study, we attempt to investigate whether a 'simple' conceptual mechanism as described in Houze Jr and Medina (2005) can also be observed in a complex environment that is embedded between two mountain ridges and which is likely influenced by upstream and downstream ef-

fects. In addition, we extend the analysis to lower altitudes, which were inaccessible in previous studies due to limits in the flight levels, by using a tethered balloon system. The balloon-borne profiles can provide information on the microphysical cloud properties in the lowest part of the boundary layer. These questions are addressed in a case study on 7 March 2019, which was observed in a post-frontal air mass during the Role of Aerosols and CLouds Enhanced by Topography on Snow campaign (RACLETS). The multi-instrument analysis is based on (1) wind profiler and wind lidar measurements, (2) observations of a Ka-band polarimetric cloud radar, a Raman lidar and a microwave radiometer, (3) in situ microphysical measurements on a tethered balloon system and (4) ground-based precipitation measurements.
The main measurement locations and instruments are briefly described in Section 3.2. An overview of the synoptic weather situation and the case study is given in Section 3.3. Section 3.4 presents the influence of low-level blocking and shear-induced turbulence on the cloud microphysics and precipitation formation. The findings are discussed in a larger context and presented in a conceptual model in Section 3.5. A summary of the main findings is given in Section 3.6.

3.2 Measurement location and instruments

The RACLETS campaign took place from 8 February 2019 to 28 March 2019 in the region around Davos in the Swiss Alps. The main objective of the campaign was to investigate the pathways of precipitation formation in orographic clouds, covering the entire aerosol-cloud-precipitation-snow distribution process chain, in order to improve our understanding of orographic precipitation. The overall goal of the RACLETS campaign was to use the gained process understanding of orographic clouds to improve regional precipitation forecast in complex terrain. For this purpose, a multi-dimensional set of instruments and measurements was deployed to provide a comprehensive dataset of orographic clouds.

3.2.1 Measurement location

A map of the instrument setup and the relevant measurement locations is shown in Figure 3.1. Davos is located in the Swiss Alps in the eastern part of Switzerland. The Alpine massif is oriented in a southwest-northeast direction and has a mean height of around 3000 m a.s.l. or 2400 m above the surrounding lowlands. The Alps represent a barrier for incoming weather systems, which predominantly approach the measurement location in Davos from northwest or south. During the presented case study, the weather system came from south-western direction and thus followed approximately the direction of the Davos valley. Weather systems approaching Davos from the south are influenced by topography to a larger extent, because the main ridge of the Alps is located south of Davos (indicated by B1 in Fig. 3.1b).
The main measurement locations consist of two mountain-top stations (Weissfluhjoch 2700 m, Gotschnagrat 2300 m), and three valley stations (Wolfgang 1630 m, Laret 1500 m, Klosters 1200 m), which are located within a distance of 10 kilometers (see Fig. 3.1a). The region around Klosters and Davos is characterized by complex topography. The Klosters valley is oriented from northwest to southeast and the elevation gradually increases from the lowlands (500 m) to 1200 m. In contrast, the Davos valley is oriented in a northeast-southwest direction.

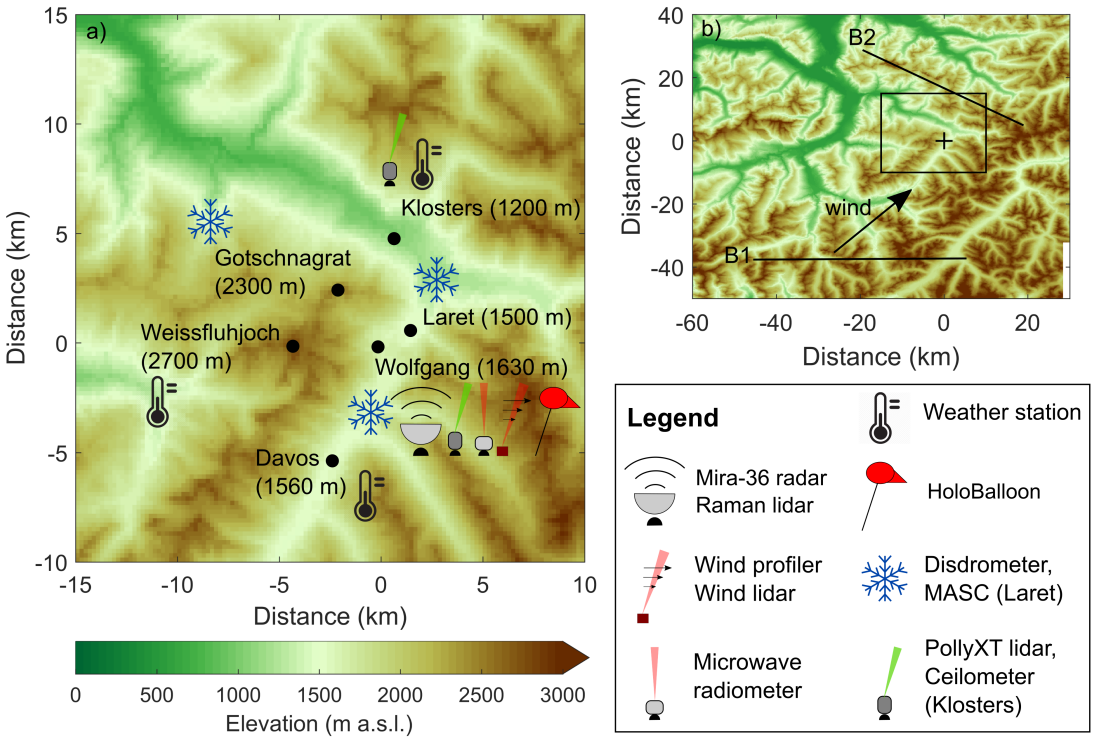

Figure 3.1: Overview of the measurement location and setup. The geographical location of Davos (black cross) and the surrounding topography is shown in (b). The large-scale wind direction during the event is shown by the black arrow and the relevant mountain barriers are indicated by B1 (upstream mountain barrier) and B2 (downstream mountain barrier). An enlarged section of the measurement sites (black rectangle in b) and the instrument setup are shown in panel (a). The elevation data was obtained from the digital height model DHM25 of the Federal Office of Topography swisstopo: https://shop.swisstopo.admin.ch/de/products/height_models/dhm25200, last access: 9 March 2020.

The height rapidly increases from Klosters (1200 m) towards Wolfgang (1630 m), before it slowly decreases on the way to Davos (1560 m). In the following, we will briefly describe the relevant instruments, which have been used in the present study.

3.2.2 Instrument setup

A set of ground-based remote sensing and in situ instruments was installed at Wolfgang to study the microphysical cloud structure (Fig. 3.1a). A vertically-pointing Ka-band cloud radar Mira-36 (METEK GmbH, Germany, Melchionna et al., 2008; Görsdorf et al., 2015; Löhnert et al., 2015) provided vertical profiles of radar reflectivity factor, Doppler velocity, Doppler spectra, spectral width and linear depolarization ratio (LDR) with a vertical resolution of 31.17 m and a temporal resolution of 10 s. A PollyXT Raman and depolarization lidar (e.g., Engelmann et al., 2016) was deployed to study the aerosol and cloud properties. Moreover, a 14-channel microwave radiometer (HATPRO, Radiometer Physics GmbH, Germany; Rose et al., 2005) provided information about the vertical temperature and humidity profiles as well as the column integrated water vapor content (IWV) and liquid water path (LWP). In situ observations of the low-level microphysical cloud structure were obtained with a tethered balloon system

(HoloBalloon; Ramelli et al., 2020). The main component of the measurement platform is the HOLographic cloud Imager for Microscopic Objects (HOLIMO), which can image cloud particles in the size range of 6 µm to 2 mm (Henneberger et al., 2013; Beck et al., 2017; Ramelli et al., 2020). It provides information about the phase-resolved number concentration, water content, size distribution and particle shape. Additionally, a ceilometer (CL31, Vaisala, US) was installed at Klosters, which was used to identify the height of the cloud base (Fig. 3.1a).
Observations of the three-dimensional wind fields were obtained with a radar wind profiler (LAP-3000 Wind profiler, Vaisala, US) and a wind lidar (Windcube 100S, Leosphere, France) at Wolfgang (Fig. 3.1a). The wind profiler had a temporal resolution of 5 min and a vertical resolution of 200 m, whereas the wind lidar provided wind measurements with a higher vertical resolution of 50 m. The wind lidar operated at an elevation angle of 75°. Additionally, Range Height Indicator scans (RHI) were performed every 30 minutes in four different azimuth directions (0°, 70°, 180° and 250°).
Precipitation was measured using a set of different ground-based precipitation instruments. Three Particle Size Velocity (Parsivel) disdrometers (OTT Parsivel2, OTT HydroMet, Germany; Tokay et al., 2014) were installed at Wolfgang (1630 m), Laret (1500 m) and Gotschnagrat (2300 m), respectively (see Fig. 3.1a). Parsivel disdrometers can measure the size and the fall velocity of hydrometeors falling through the sample volume independently. The particle size is estimated from the signal attenuation, whereas the particle fall velocity is estimated from the duration of the measured signal. Precipitation particles in the size range between 0.2 mm and 25 mm can be measured by the disdrometer with a temporal resolution of 30 s. Additionally, a Multi-Angle Snowflake Camera (MASC) at Laret took photographs of hydrometeors from three different angles and measured their fall velocity simultaneously (Garrett et al., 2012). The MASC is sensitive to particles in the size range of 100 µm and 10 cm. Lastly, a snow drift station was installed at Gotschnagrat, which provided information about the snow redistribution at the ground and the low-level wind field (Walter et al., 2020).

3.3 Description of the case study

The weather situation on 7 March 2019 was characterized by a low-pressure system that moved from the North Sea towards Scandinavia and brought a cold front towards Switzerland (Fig. 4.2a). Ahead of the cold front, a 15 hPa pressure gradient between the south and north side of the Alps produced a strong foehn event with wind gusts of up to 130 $\mathrm{km\,h^{-1}}$. The cold front crossed Switzerland from the southwest in the morning and ended the pronounced foehn situation. Based on observations, rainfall of up to 50 mm was produced on the southern side of the Alps during the passage of the cold front (not shown). Moist southwesterly flow in the post-frontal air mass led to light showers on the south side of the Alps due to orographic lifting. Some spillover precipitation was observed on the lee side of the Alps and reached the measurement locations in Davos. The presented case study was measured in the post-frontal air mass between 16 UTC and 20 UTC.
The temperature at Davos (1600 m) was around 0 °C during the entire observational period, whereas the temperature at Weissfluhjoch (2700 m) decreased from -4.5 °C to -6 °C between 16 UTC and 20 UTC. Due to the lack of a sounding in the Davos area during the measurement

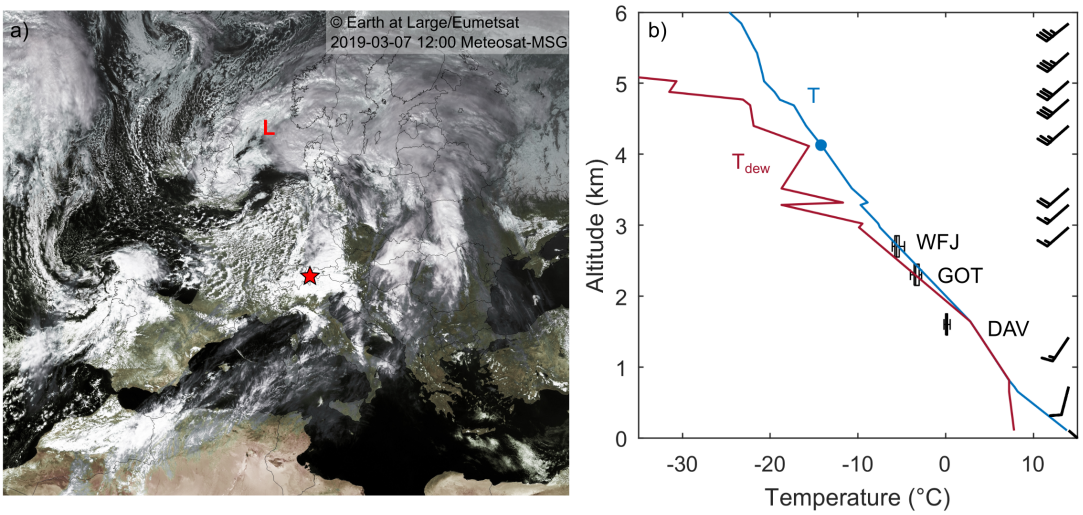

Figure 3.2: Overview of the synoptic weather situation on 7 March 2019 showing a satellite picture over Europe (a) and the temperature profile of a radiosonde ascent (b). The satellite picture was taken by the Meteosat at 12 UTC (Eumetsat). The radiosonde was launched from Milan (12 UTC; `http://meteocentre.com/radiosonde/`; last access: 16 March 2020) and shows the temperature (blue) and dew point temperature (red) profiles. The boxplots in (b) show the temperature measured at Davos (DAV, 1600 m), Gotschnagrat (GOT, 2300 m) and Weissfluhjoch (WFJ, 2700 m) during the measuement period. The cloud top temperature (-14 °C) and height (4000 m; estimated from cloud radar observations averaged between 17 UTC and 18.30 UTC) are indicated by the blue dot. The wind barbs are shown on the right side.

period, the vertical temperature profile of a radiosonde ascent from Milan (Italy; at 12 UTC) is shown instead (Fig. 4.2b). The sounding in Milan is assumed to be representative of the upper air situation in Davos, as the air flow was from the southwest. In addition, the temperatures measured at Gotschnagrat and Weissfluhjoch were in good agreement with the temperature profile of the radiosonde (within 1 - 2 K), whereas the temperature observed in Davos was slightly colder. A cloud top temperature of around -14 °C was estimated from the observed temperature profile.

An overview of the microphysical cloud structure is shown in Figures 3.3 and 3.4. The cloud radar observations indicate the presence of a mid-level cloud with a cloud top at around 4000 m. The highest reflectivities (> 5 dBZ) were observed between 2500 m and 3500 m (Fig. 3.3a). The reflectivity decreased below 2500 m, indicating the presence of a sublimation layer. The Doppler velocity showed mainly regions with negative Doppler velocity (Fig. 3.3b). Positive Doppler velocities (i.e., updrafts) were only observed after 18 UTC near cloud top and after 19 UTC near the ground. Additionally, several regions of enhanced spectral width were observed (Fig. 3.3c). High values in the spectral width signal can be the result of enhanced turbulence and/or indicate the presence of multiple particle populations with different fall speeds (e.g., Shupe et al., 2004; Shupe et al., 2006). The linear depolarization ratio (LDR) ranged between -32 dB and -22 dB (Fig. 3.3d) and provides information about the shape of the cloud particles. A perfectly spherical particle (e.g., small cloud droplet) has no depolarization and thus an LDR of $-\infty$ dB, whereas a particle with a high aspect ratio has a LDR close to 0 dB. Furthermore, the LDR of a specific hydrometeor type depends on the elevation angle. Since a vertically-pointing cloud

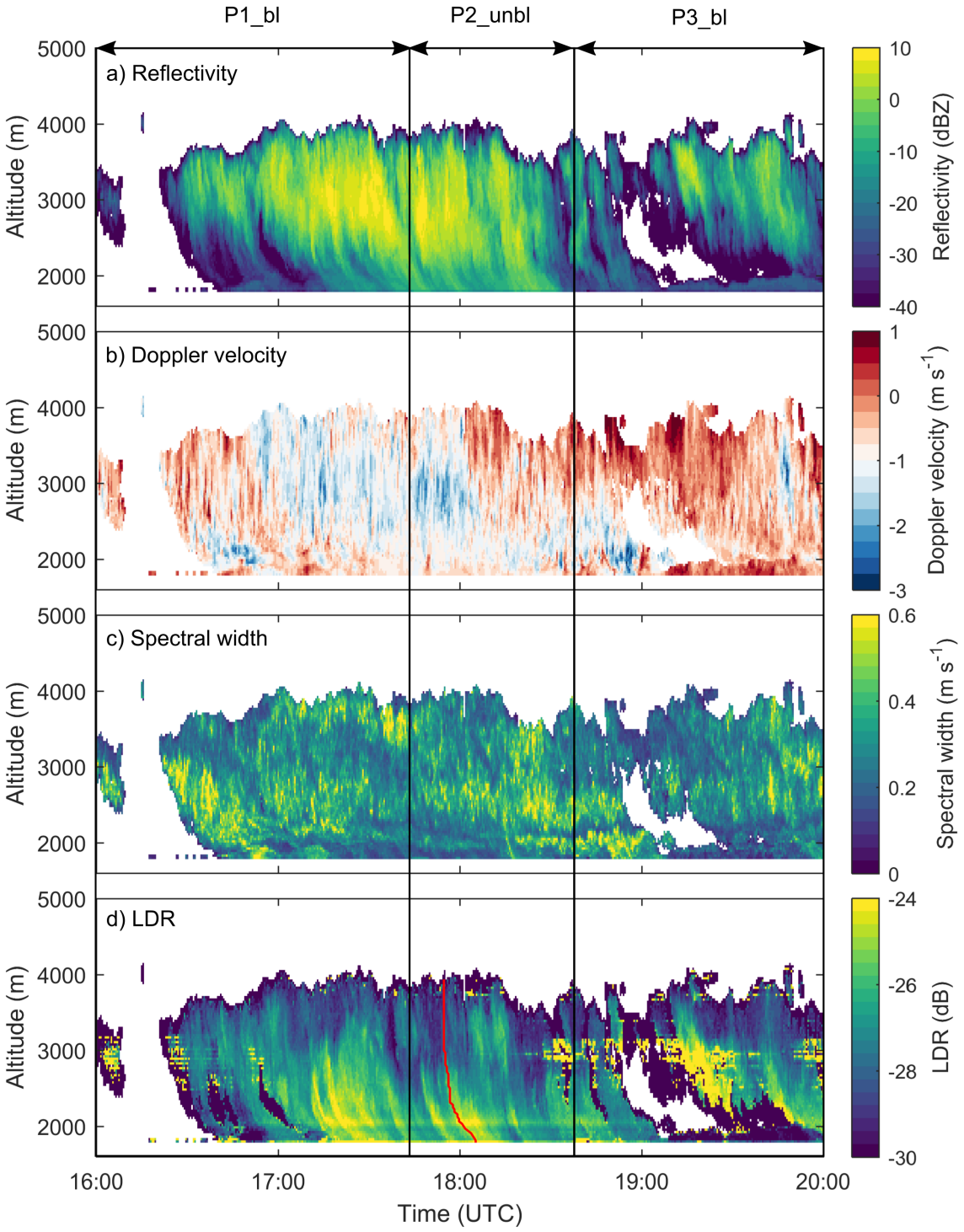

Figure 3.3: Cloud radar observations of the radar reflectivity (a), Doppler velocity (b), spectral width (c) and linear depolarization ratio (d) measured on 7 March 2019. Note that the colorbar in (b) is centered at -1 m s^{-1} to approximately account for the hydrometeor fall speed. The red line in panel (d) indicates the track of the 18 UTC LDR-fallstreak, which was investigated in Fig. 3.10. The measurement period is divided into three periods, where P1_bl and P3_bl indicate blocked low-level flow and P2_unbl indicates unblocked low-level flow (see Sect. 3.4.1 for more details).

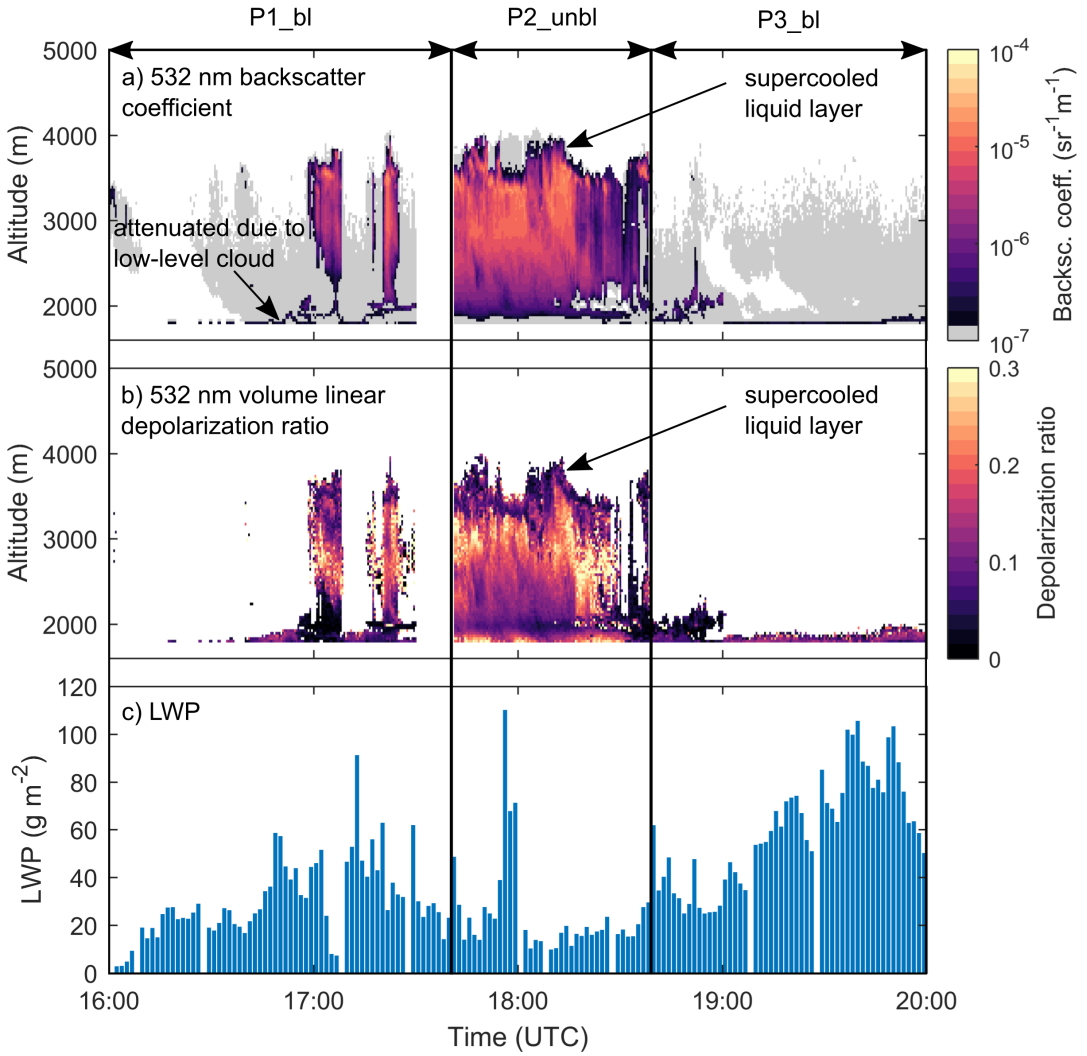

Figure 3.4: Observations of the lidar attenuated backscatter coefficient (a), the lidar linear depolarization ratio (b) and the liquid water path measured by the microwave radiometer (c). The measurement period is divided into three periods, where P1_bl and P3_bl indicate blocked low-level flow and P2_unbl indicates unblocked low-level flow (see Sect. 3.4.1 for more details).

radar was used in this study, the observed LDR signal can only differentiate between isometric particles (e.g., droplets, plates, dendrites) and prolate particles (e.g., needles, columns). The LDR signal was enhanced locally in some fallstreaks at altitudes below 3000 m, which is indicative of a change in the particle shape. The band of enhanced LDR at 2100 m, which was visible during the entire measurement period, shows the effects of ground clutter (i.e., echos received from objects on the ground or sidelobes reflected from nearby mountains).

The lidar signal was mainly attenuated due to the presence of a low-level liquid cloud (Fig. 3.4). When the low-level liquid cloud dissipated (17:45 - 18:40 UTC), the lidar signal indicated the presence of an embedded liquid layer at an altitude of around 3500 m. This can be seen by the enhanced attenuated backscatter signal (Fig. 3.4a) and the low lidar depolarization ratio (Fig. 3.4b). The measured LWP was generally below 100 g m^{-2} (Fig. 3.4c).

The case study was divided into three periods: Period P1_bl (16:00 UTC - 17:45 UTC) and period P3_bl (18:40 UTC - 20:00 UTC) were characterized by blocked low-level flow and the pres-

ence of a low-level liquid cloud at around 2000 m, whereas the low-level blocking weakened and the low-level cloud dissipated during period P2_unbl (17:45 UTC - 18:40 UTC). In the following, we characterize the dynamics of the flow during the measurement period (Section 3.4.1). In a second step, we investigate the influence of shear-induced turbulence on the cloud microphysics and precipitation formation (Section 3.4.2). Lastly, the role of the low-level blocking for the formation of a low-level feeder cloud is discussed in Section 3.4.3.

3.4 Results

3.4.1 Low-level flow blocking triggering wind shear and turbulence

The horizontal wind fields were measured with a radar wind profiler and a wind lidar at Wolfgang (Fig. 3.5). Both wind profiler and wind lidar data are shown, as the wind lidar was attenuated during most of P1_bl and P3_bl due to the presence of a low-level liquid cloud (Section 3.4.3). The wind speed measured by the wind profiler increased from around $4\,\mathrm{m\,s^{-1}}$ at 2200 m up to $18\,\mathrm{m\,s^{-1}}$ at 3500 m (Fig. 3.5a). The wind lidar revealed a second layer of increased wind speed between 2500 m and 3000 m (Fig. 3.5b), which was not captured by the wind profiler due to its lower resolution. The layer of increased wind speed lowered between 17:00 UTC and 18:30 UTC, suggesting stronger cross-barrier flow. The large-scale wind direction was from the southwest. Only in the lowest 100 m of the boundary layer, a flow from the northeast was observed by the wind lidar.

The counterflow at low levels with respect to the large-scale flow as well as the low wind speed close to the surface are indicative of blocked low-level flow (e.g., Houze Jr and Medina, 2005). More specifically, the low-level flow at Wolfgang might have been too weak to ascend over the mountain barrier located downstream of Wolfgang (B2 in Fig. 3.1b) and might have generated a counterflow when it impinges on the mountain barrier. To test this hypothesis and to study the observed pattern in the low-level wind field in more detail, wind measurements from different valley and mountain-top weather stations around Davos and Klosters were analyzed (Fig. 3.6). Several valley stations (Davos, Davos Seehornwald, Wolfgang, Klosters Gatschiefer) observed the presence of a counterflow (i.e., wind from northeastern direction), indicative of blocked low-level flow. The wind pattern at Klosters Madrisa, which is located immediately below the mountain barrier B2, was more diverse, showing large variations in the prevailing wind direction. The mountain-top stations (Weissfluhjoch, Gotschnagrat, Klosters Sant Jaggem) observed wind from the south and southwestern direction in accordance with the large-scale wind direction. Therefore, the observed wind pattern at the different locations support the hypothesis of a blocked low-level flow. It is important to note that a counterflow was only observed during P1_bl and P3_bl at the valley stations in Davos (Davos, Davos Seehornwald, Wolfgang), indicating that the low-level flow changed from a blocked (P1_bl, P3_bl) to an unblocked (P2_unbl) state during the event (see also Fig. 3.7 for the temporal evolution at Wolfgang). The flow at Klosters Gatschiefer was still blocked during P2_unbl, suggesting that the blocking became weaker and moved closer to the mountain barrier located downstream.

From a theoretical perspective, the Froude number can be used to estimate whether a flow that encounters a mountain barrier can pass over the mountain barrier or not (Smith, 1979; Durran,

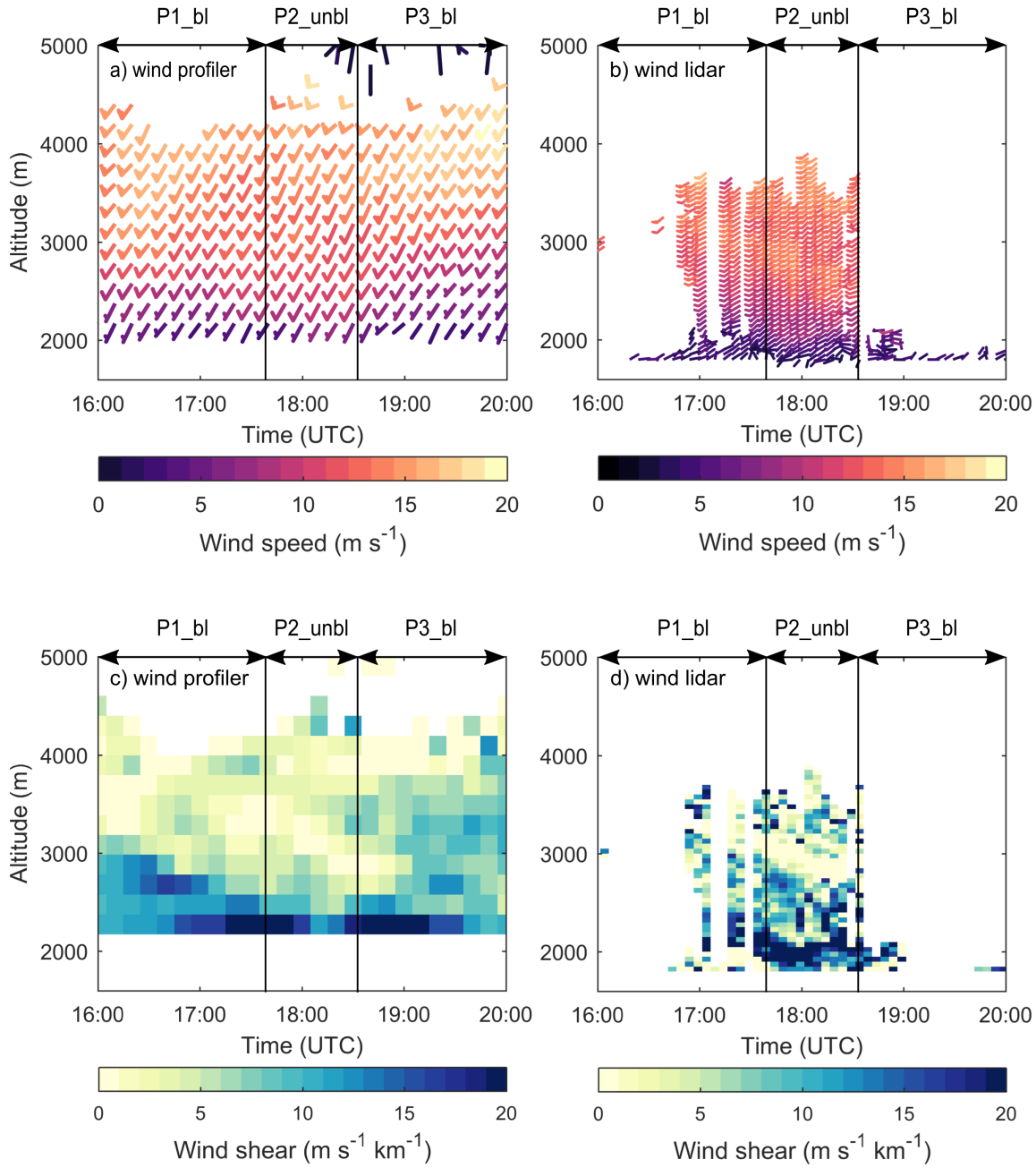

Figure 3.5: Vertical profiles of wind speed and direction (a, b) and wind shear (c, d) measured by the radar wind profiler (left) and wind lidar (right). The vertical wind shear was calculated from the wind observations, considering changes in the scalar wind speed between two adjacent height levels.

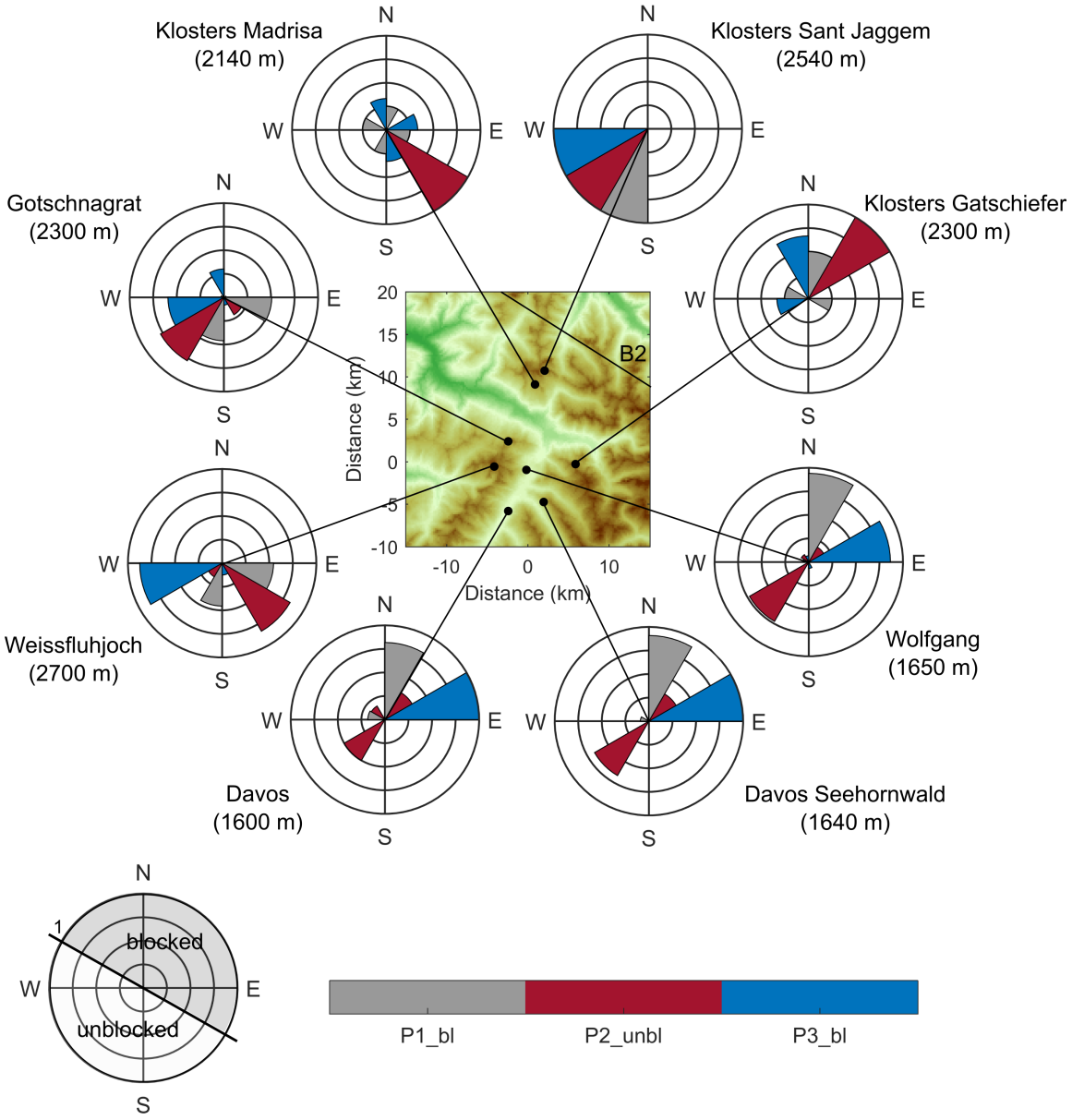

Figure 3.6: Wind observations at different weather stations around Davos and Klosters, indicating the wind direction observed during the time periods P1_bl (gray), P2_unbl (red) and P3_bl (blue). The wind directions in the different periods were normalized and binned in sectors of 90° (NE, SE, SW, NW). Each line indicates 25%. The example wind rose on the bottom left indicates the wind directions during a blocked (gray) / unblocked (white) low-level flow in the Davos valley. The wind observations at the weather stations in Davos had a temporal resolution of 10 min, whereas the stations around Klosters had a temporal resolution of 30 min. The measurements at Wolfgang were obtained from the wind lidar observations at an altitude of 1800 m and the measurements at Gotschnagrat from a 3D ultrasonic anemometer that was an integral part of the snow drift station.

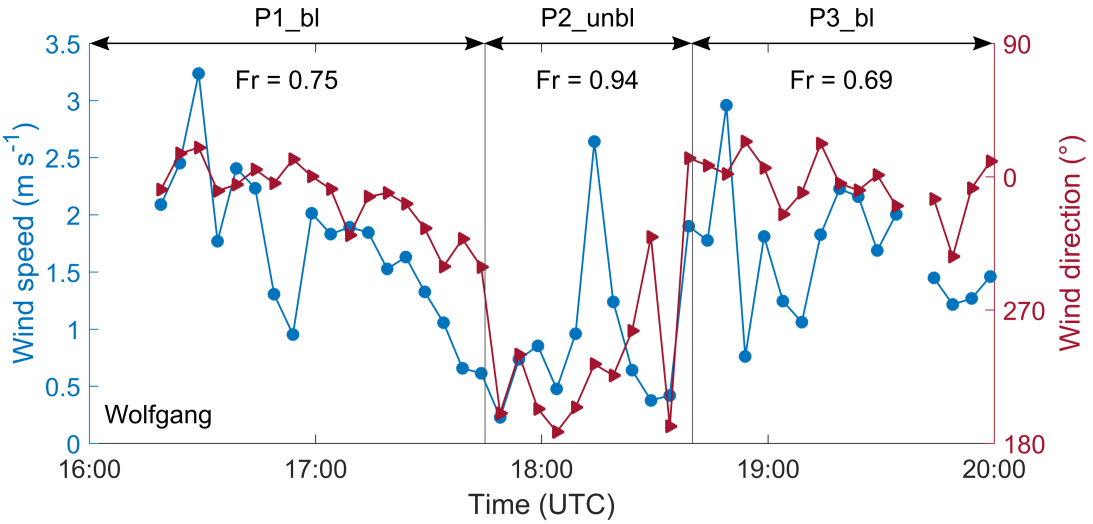

Figure 3.7: Temporal evolution of the wind speed (blue) and wind direction in azimuth degrees (red) at Wolfgang obtained from the wind lidar measurements at an altitude of 1800 m. The Froude numbers for the different periods are indicated at the top (see Appendix 3.A for calculations).

1990; Rotunno and Houze, 2007; Houze Jr, 2012). The Froude number Fr is given by the following equation:

$$Fr = \frac{U}{hN} \tag{3.1}$$

where U is the wind speed perpendicular to the mountain barrier, h is the height of the mountain barrier and N is the Brunt-Väisälä frequency (Colle et al., 2013). The Froude number was below 1 for all periods (see Appendix 3.A), indicating that the low-level flow was blocked. The Froude number increased from 0.75 during P1_bl to 0.94 during P2_unbl (Fig. 3.7), suggesting that the blocking became weaker during P2_unbl. We will refer to period P2_unbl as unblocked flow, as no counterflow was observed during this period at Wolfgang (Fig. 3.7), even though it can be seen that the flow at low levels was still slowed down and the Froude number was slightly below 1. Thus, period P2_unbl could also be regarded as a weaker blocking.

The wind profiler and wind lidar indicated the presence of a layer of strong vertical wind shear ($> 10\,\mathrm{m\,s^{-1}\,km^{-1}}$), which separated the blocked layer from the stronger cross-barrier flow (Fig. 3.5c, d). The shear layer descended from 3000 m to 2000 m between 16 UTC and 18 UTC (Fig. 3.5c) in accordance with the weaker blocking and stronger cross-barrier flow. As the cross-barrier flow weakened and the strength of the low-level blocking increased again at around 18:30 UTC, the shear layer ascended (Fig. 3.5c). Thus, the height of the shear layer is determined by a delicate balance of upstream (e.g., blocking) and downstream (e.g., cross-barrier flow) effects, as Wolfgang is located in an inner-Alpine valley and surrounded by multiple mountain barriers. Regardless of the formation mechanism, wind shear can be a source of turbulence and can have important implications for cloud microphysics. Houze Jr and Medina (2005) defined a critical threshold of $10\,\mathrm{m\,s^{-1}\,km^{-1}}$ for the formation of shear-induced turbulent cells. The observed wind shear ($10\text{-}20\,\mathrm{m\,s^{-1}\,km^{-1}}$) was above this threshold value in the entire shear layer, suggesting that turbulent cells were embedded within the shear layer. In the following section, we will characterize the microphysical cloud structure and investigate the influence of shear-induced turbulence on the cloud microphysics and precipitation formation.

3.4.2 Influence of shear-induced turbulence on the cloud microphysics

Contour frequency by altitude diagrams (CFADs) are a useful tool for analyzing the magnitude and the vertical frequency distribution of cloud properties (e.g., Yuter and Houze Jr, 1995). CFADs of the cloud radar reflectivity (a, b), spectral width (c, d) and LDR (e, f) are shown in Figure 3.8 averaged over sub-periods of P1_bl (left) and P2_unbl (right). A strong increase in the radar reflectivity was observed near cloud top (Fig. 3.8a, b), indicative for ice formation and growth between 4000 m and 3500 m. Since the region of rapid increase in radar reflectivity was coincident with the height of the supercooled liquid layer measured by the Raman lidar (L in Fig. 3.8a, b), it is likely that this supercooled liquid layer played an important role for ice nucleation and initial ice growth. The cloud particles continued growing below 3500 m until they reached a sublimation layer, which was identified by the layer of decreasing radar reflectivity and also used as definition for cloud base. The cloud base lowered between P1_bl and P2_unbl (Fig. 3.9), likely as a consequence of the stronger cross-barrier flow and the subsequent lowering of the shear layer. Consequently, the extent of the sublimation layer decreased between P1_bl (800 m) and P2_unbl (400 m) (Fig. 3.8a, b), which enabled the hydrometeors to reach the surface prior to complete sublimation (Fig. 3.9). The highest radar reflectivities were observed within the upper part of the turbulent shear layer (marked with S_1 and S_2 in Fig. 3.8), suggesting that turbulence created updrafts high enough for exceeding ice saturation and thereby enhanced ice growth. The turbulent kinetic energy (TKE) measured by a 3D ultrasonic anemometer at Gotschnagrat (2300 m) increased from $0.1\,m^2\,s^{-2}$ to $0.4\,m^2\,s^{-2}$ between P1_bl and P2_unbl as the shear layer lowered (Fig. 3.9). The CFADs of the spectral width (Fig. 3.8c, d) show two local maxima embedded within the shear layer (at 2500 m and at 2000 m), indicating the presence of a broad hydrometeor size distribution within those regions, which can arise from enhanced turbulence. Additionally, an increase in the LDR was observed within the shear layer (Fig. 3.8e, f), which is indicative of a change in the hydrometeor shape. Thus, (1) the spatial coincidence of the shear layer and the maximum reflectivity (Fig. 3.9), (2) the temporal coincidence of the precipitation and the lowering of the shear layer and cloud base (Fig. 3.9) and (3) the moderate to strong correlations between dynamics, microphysics and precipitation parameters (Appendix 3.B) suggest that the processes active within the turbulent shear layer enhanced ice growth and precipitation formation.

To further explore the microphysics within the turbulent shear layer, the Doppler spectra of the radar reflectivity and LDR along the 18 UTC fallstreak (Fig. 3.10; highlighted by red line in Fig. 3.3d) and the surface-based hydrometeor particles observations (Fig. 3.11) were analyzed. As mentioned in Section 3.3, the LDR can provide information about the shape of cloud particles. A LDR of around -28 dB was observed near cloud top (Fig. 3.10b), which is characteristic for oblate particles such as dendrites and plates (e.g., Myagkov et al., 2016; Bühl et al., 2016). This is in agreement with the ice habit expected to form at a cloud top temperature of -14 °C (Magono and Lee, 1966; Bailey and Hallett, 2009) and with the ice particles observed by the MASC at the surface (Fig. 3.11a). Since a rather constant LDR was observed between 4000 m and 3000 m (Fig. 3.10b), we assume that the ice crystals grew in size by vapor deposition without changing their habit. Below 3000 m, the LDR increased up to -20 dB within the fallstreak (Fig. 3.10b). Interestingly, the increase in the LDR was collocated with the region of maximum radar

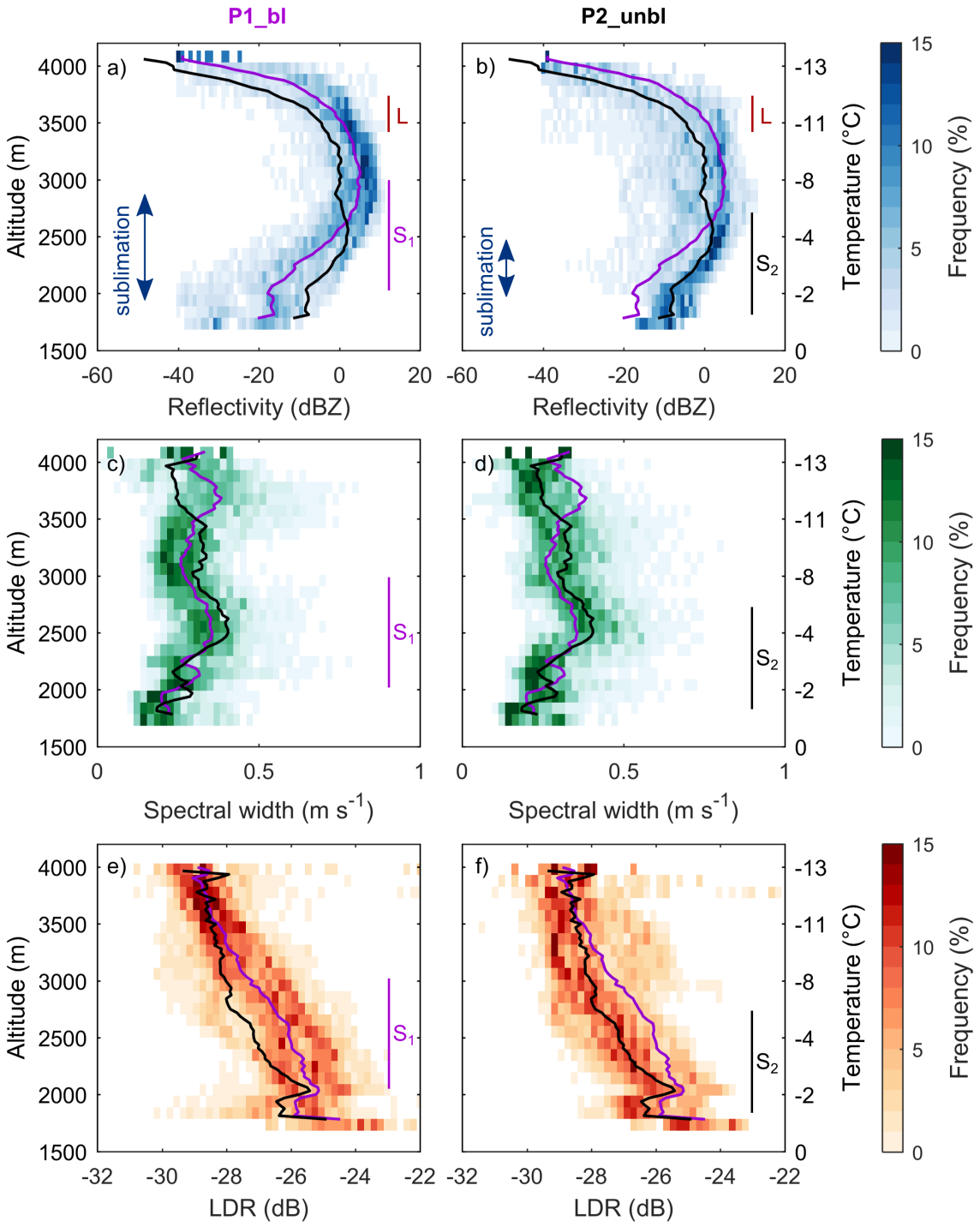

Figure 3.8: CFADs of the radar reflectivity (a, b), spectral width (c, d) and linear depolarization ratio (e, f) averaged over sub-periods of P1_bl (left, 17 UTC - 17:45 UTC) and P2_unbl (right, 17:45 UTC - 18:30 UTC). The following bin sizes were applied: (1) radar reflectivity from -40 dBZ to 20 dBZ in 1 dBZ intervals, (2) spectral width from 0 m s^{-1} to 0.8 m s^{-1} in 0.02 m s^{-1} intervals and (3) LDR from -32 dB to -22 dB in 0.2 dB intervals. A height interval of 100 m was used for all radar properties. The solid lines represent the mean vertical profile of P1_bl (purple) and P2_unbl (black). The temperature profile measured by the radiosonde is shown on the right y-axis. The extent of the shear layer (S_1, S_2, from wind profiler), the supercooled liquid layer (L, from cloud lidar) and the sublimation layer (blue arrow, from cloud radar) are indicated.

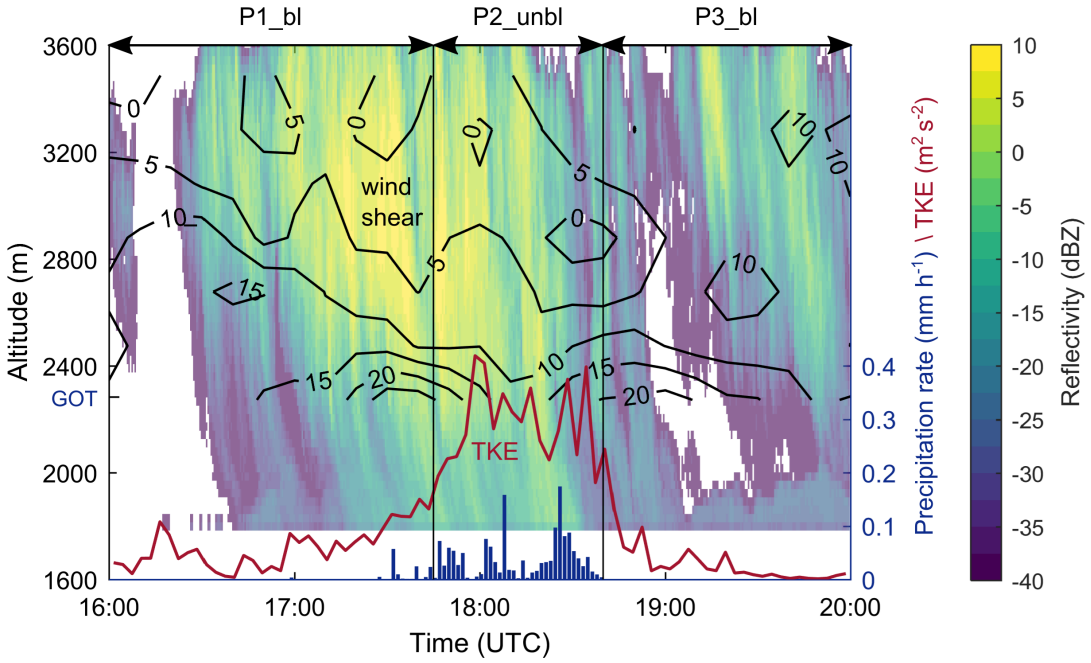

Figure 3.9: Temporal and spatial evolution of the vertical wind shear (in $\mathrm{m\,s^{-1}\,km^{-1}}$, black contour lines), the radar reflectivity (colorfill), the TKE (red line) and the precipitation rate (blue bars). The wind shear was calculated from the wind profiler observations (Fig. 3.5). The precipitation rate was measured with a disdrometer at Wolfgang (1630 m) and the TKE was measured with a 3D ultrasonic anemometer at Gotschnagrat (2300 m). Correlation coefficients between the different parameters (shear layer, radar reflectivity, precipitation) were calculated in Appendix 3.B and indicated moderate to strong correlations significant at the 5 % level.

reflectivity (2900 m; Fig. 3.10a). The spatial coincidence between maximum radar reflectivity, shear layer and increase in LDR was also observed for other fallstreaks (Fig. 3.3d), suggesting that the turbulent shear layer did not only enhance ice growth but also contributed to a change in the cloud particle shape. An increase in the LDR can be explained by the presence of needles, columns and/or irregular ice particles. Here we propose different mechanisms, which could have contributed to an increase in the observed LDR signal. Firstly, the temperature between 3000 m and 2500 m ranged from -8 °C to -4 °C and was thus in the temperature regime of column/needle growth. Thus, needles might have grown on the existing ice particles while they fell through that cloud layer. Indeed, the ice particles observed by the HoloBalloon platform near the ground show indications of needle-like structures (e.g., at 17:50 UTC; Fig. 3.11b). If fragile ice crystals such as dendrites or needle-like structures collide with large ice particles within the turbulent shear layer, small ice fragments might break off and lead to the production of secondary ice particles upon collision (e.g., Vardiman, 1978; Yano et al., 2016). For example, the ice particles measured by HOLIMO at 17:45 UTC could be a dendritic arm that broke off upon collision. Small secondary ice particles could then rapidly grow by vapor deposition in the water-saturated environment into column-like particles, which are characterized by a higher LDR. However, the analysis of the Doppler spectra showed no evidence of multiple spectral peaks (i.e., the presence of multiple particle populations with different fall speed), which would support the occurrence of secondary ice production. Lastly, turbulence can also increase the generation of large ice particles (e.g., Pinsky and Khain, 1998), for example, when multiple ice crystals

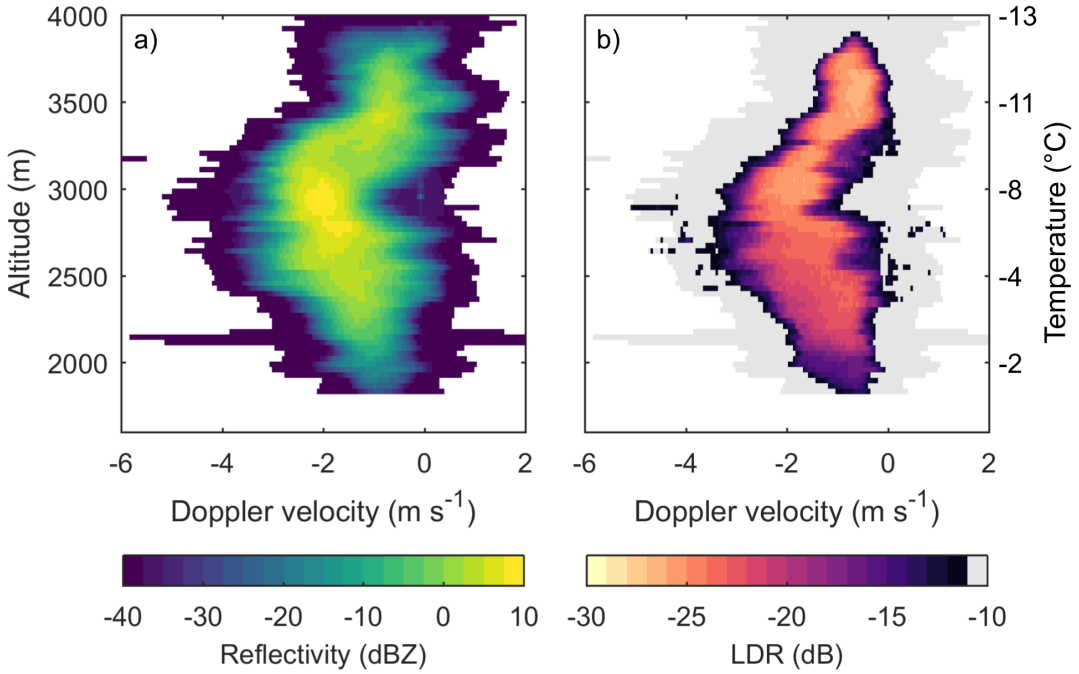

Figure 3.10: Vertical profile of the radar reflectivity (a) and LDR (b) Doppler spectra along the LDR-fallstreak at 18 UTC averaged over 1 min (see red line in Fig. 3.3d). The temperature profile measured by the radiosonde is shown on the right y-axis.

collide and stick together (aggregation). Aggregation is most efficient at temperatures higher than -10 °C, because of the higher sticking efficiency due to the presence of a thicker quasi-liquid layer at warmer temperatures (e.g., Lohmann et al., 2016b). Thus, if the aggregated particles that formed in the turbulent shear layer were irregular, this could explain the increased LDR. Indeed, the MASC indicated the presence of large irregular aggregates between 17:40 UTC and 18:40 UTC (Fig. 3.11a). For a more sophisticated analysis, a larger number of particles would be necessary, but due to the moderate precipitation rate at Wolfgang and Laret, only a limited amount of ice and snow particles was observed. However, in general, the in situ and surface observations of ice particles support the radar-based assumptions above, in that (1) dendrites formed near the cloud top and (2) aggregation and needle growth occurred within the turbulent shear layer. It remains unclear whether mechanical break-up in ice-ice collisions contributed to the formation of secondary ice particles.

3.4.3 Flow blocking as a driver for the formation of low-level feeder clouds

In the last part of this study, we focus on the lower part of the boundary layer and investigate the role of low-level blocking for the formation of a low-level feeder cloud. The low-level cloud structure was observed with the measurement platform HoloBalloon. Vertical profiles of the in situ cloud properties are shown in Figure 3.12. The cloud droplet number concentration (CDNC) showed a rather inhomogeneous cloud structure during P1_bl. Cloud swaths with a CDNC of up to 100 cm^{-3} alternated with "cloud-free" regions with low CDNC (Fig. 3.12a). The mean cloud droplet diameter ranged between 10 µm and 17 µm (Fig. 3.12b) and was generally larger when the CDNC was low. No vertical profiles were performed between 17:50 UTC and

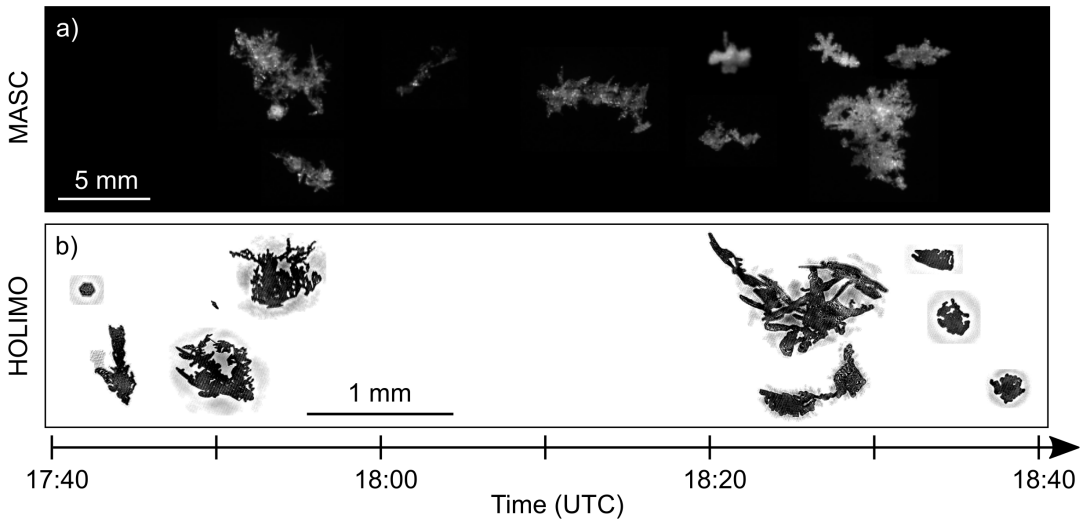

Figure 3.11: Photographs of ice crystals and snow particles, which have been taken with the MASC (a) and HOLIMO (b). No observations of HOLIMO were available between 17:50 UTC and 18:20 UTC. Please note the different size scale of the particles observed by the MASC and HOLIMO.

18:20 UTC, because the low-level cloud dissipated during this time period. This is also visible from the cloud lidar signal, which was not attenuated during P2_unbl in the lower part (see Fig. 3.12 and Fig. 3.4a). A second low-level cloud formed during P3_bl. This cloud had a more homogeneous structure with a CDNC in the range between 60 cm^{-3} and 120 cm^{-3}. The mean cloud droplet diameter steadily increased from 10 µm to 16 µm. A low-level cloud was also observed by the cloud base observations of the ceilometer located in Klosters (not shown).

The interesting observation was that the low-level cloud dissipated during P2_unbl, when the low-level flow turned from a blocked to an unblocked state, pointing to the importance of the blocking situation in forming and sustaining the low-level liquid cloud. We suggest that an overturning cell formed as a consequence of the low-level flow impinging on the mountain barrier located downstream of Wolfgang (as shown in Fig. 3.13a), which generated a low-level counterflow from Klosters towards Davos. Several weather stations near Davos confirm that a counterflow was present during P1_bl and P3_bl (Fig. 3.6). Since Wolfgang is located on a small-scale topographic feature (400 m), the low-level flow was forced to rise from Klosters (1200 m) to Wolfgang (1630 m) over the local topography and thereby acted as an updraft source, which led to the formation of a low-level feeder cloud. Indeed, the cloud radar indicated the presence of updrafts below 2000 m (i.e., positive Doppler velocities) after 19 UTC (Fig. 3.3b). When the blocking weakened, the low-level cloud at Wolfgang dissipated because of the missing upward motion to sustain the production of liquid water.

This observation points to the importance of localized flow effects that interact with the topography in producing low-level feeder clouds over small-scale topographic features. Feeder clouds can enhance orographic precipitation through the seeder-feeder mechanism (Bergeron, 1965; Bader and Roach, 1977; Hill et al., 1981), by providing an environment where hydrometeors that formed aloft (i.e., in the seeder region) can "feed" on the low-level liquid layer and enhance precipitation by riming and depositional growth. The seeder-feeder mechanism was for example visible in the cloud radar observations between 19 UTC and 20 UTC (Fig. 3.3a). In

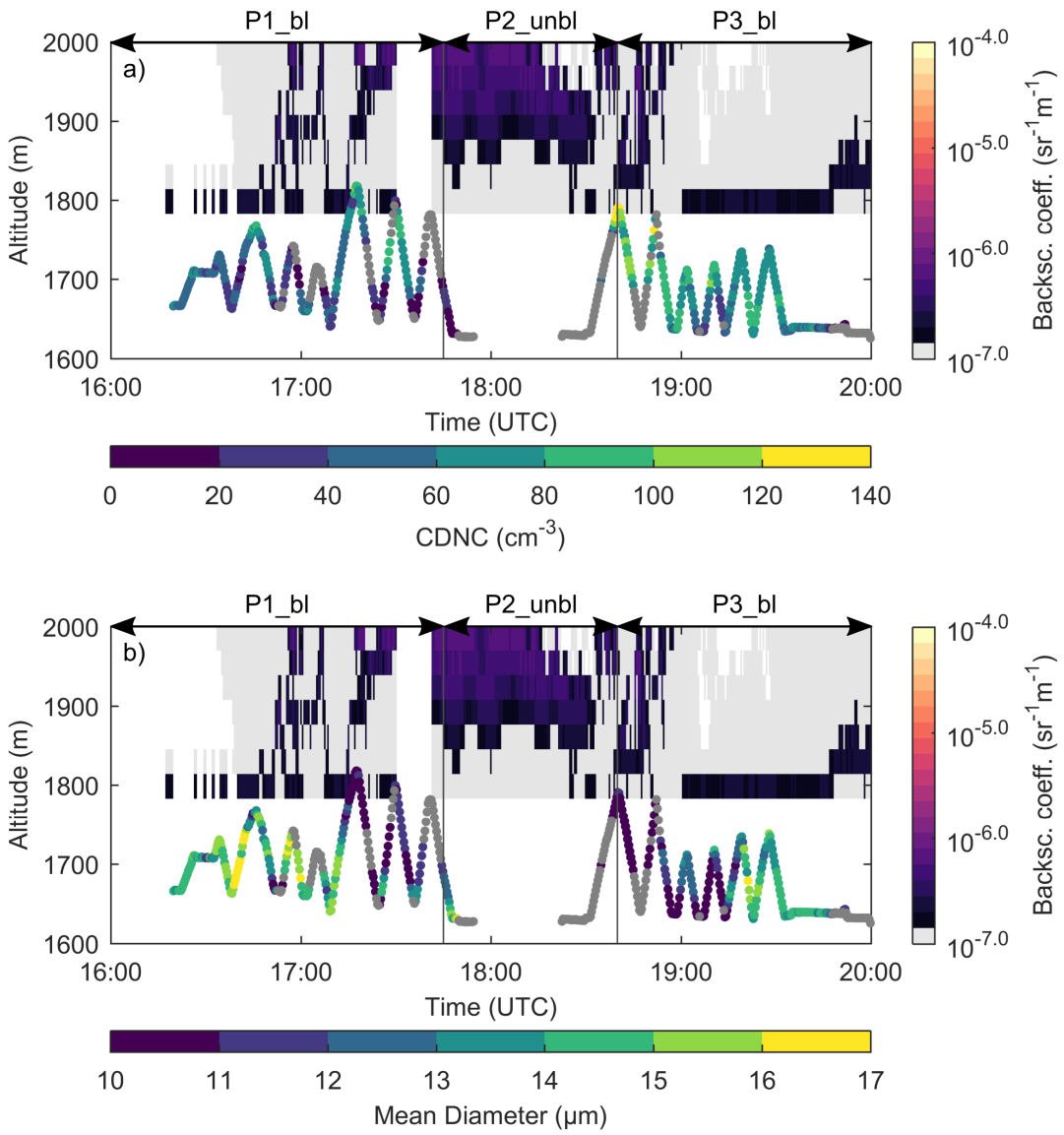

Figure 3.12: Vertical profiles of the CDNC (a) and mean droplet diameter (b) measured with the HoloBalloon platform. The lidar attenuated backscatter coefficient in the lowest levels is shown in the background. Data points with a liquid water content below 0.01 g m^{-3} are indicated by gray dots. No measurements were obtained between 17:50 UTC and 18:20 UTC.

the present case study, this low-level feeder cloud did not play a role for precipitation enhancement, as a significant fraction of the hydrometeor mass sublimated before reaching the feeder cloud and precipitation was highest when the flow was unblocked. However, we propose that local flow effects such as low-level blocking can also induce the formation of feeder clouds in other mountain valleys and in hilly regions and suggest that the extent of this effect depends on the strength of the blocking, the thermodynamics of the atmosphere and the altitude of the small-scale topographic feature that is located upstream of the mountain barrier.

3.5 Discussion

The microphysical evolution of the mixed-phase cloud in the inner-Alpine valley was determined by a complex interplay between orography, dynamics and microphysics. A conceptual overview of the observed cloud is shown in Figure 3.13 (a: blocked state; b: unblocked state). Primary ice nucleation was suggested to occur close to the cloud top in the embedded supercooled liquid cloud layer. Based on the cloud top temperature and cloud radar and hydrometeor observations, dendrites and hexagonal plates were assumed to form, which could rapidly grow by vapor deposition. The ice particles encountered a turbulent shear layer while falling through the cloud, within which changes in the microphysical cloud properties were observed including enhanced radar reflectivity (i.e., increased ice growth) and LDR (i.e., change in particle shape). This suggests that the turbulent shear layer influenced the cloud microphysics.

Previous studies identified flow blocking and shear-induced turbulence as a microphysical pathway for enhancing snow growth and precipitation (e.g., Marwitz, 1983; Overland and Bond, 1995; Yu and Smull, 2000; Hogan et al., 2002; Neiman et al., 2002; Neiman et al., 2004; Houze Jr and Medina, 2005; Loescher et al., 2006; Olson et al., 2007; Olson and Colle, 2009; Geerts et al., 2011; Medina and Houze Jr, 2015; Grazioli et al., 2015; Aikins et al., 2016). Different microphysical processes have been proposed to occur in the turbulent layer, such as enhanced growth by riming due to pockets of higher liquid water content (e.g., Houze Jr and Medina, 2005; Medina and Houze Jr, 2015 Grazioli et al., 2015) or enhanced growth by aggregation due to increased collisions between hydrometeors (e.g., Geerts et al., 2011; Aikins et al., 2016). Based on the cloud radar observations and the ground-based snow particle measurements, we suggest that depositional growth and aggregation were the dominant ice growth mechanisms in the present case study. Riming was assumed to play only a minor role, due to the low LWP ($< 100\,\mathrm{g\,m^{-2}}$) observed by the microwave radiometer (Fig. 3.4c). Furthermore, the hydrometeors observed at the surface appeared primarily unrimed and indicated the presence of aggregates, dendrites and irregular ice particles (Fig. 3.11).

Furthermore, an increase in the LDR (>-25 dB; i.e., column-like ice particles) was observed within the shear layer (Fig. 3.10b and Fig. 3.3d), which is indicative for a change in the hydrometeor shape. Based on the prevailing temperature near cloud base (from -8 °C to -5 °C) and the ice particle habits observed at the surface (Fig. 3.11), we suggest that needle growth occurred on the existing ice particles within the turbulent shear layer. Previous laboratory studies have observed needle growth at temperatures of -5 °C slightly below liquid water saturation (Knight, 2012). Thus, if fragile ice crystals such as dendrites or ice particles with needle-like structures collide with large ice particles, small ice fragments can break off and lead to the production of secondary ice particles (e.g. Vardiman, 1978; Yano et al., 2016). Previous studies have observed a large number of small ice particles within turbulent shear layers, which were likely generated through secondary ice production mechanisms (e.g., Hogan et al., 2002; Grazioli et al., 2015). For example, Hogan et al. (2002) observed high concentrations of small ice particles (100 - $1000\,\mathrm{L^{-1}}$) in and above a region of embedded convection, which were likely produced through the Hallett-Mossop mechanism during riming. Since the fall velocity of small ice particles is low, these secondary ice particles were found to recirculate in the updrafts/turbulent region and to feed the regions above the shear layer with ice crystals (Hogan et al., 2002; Grazi-

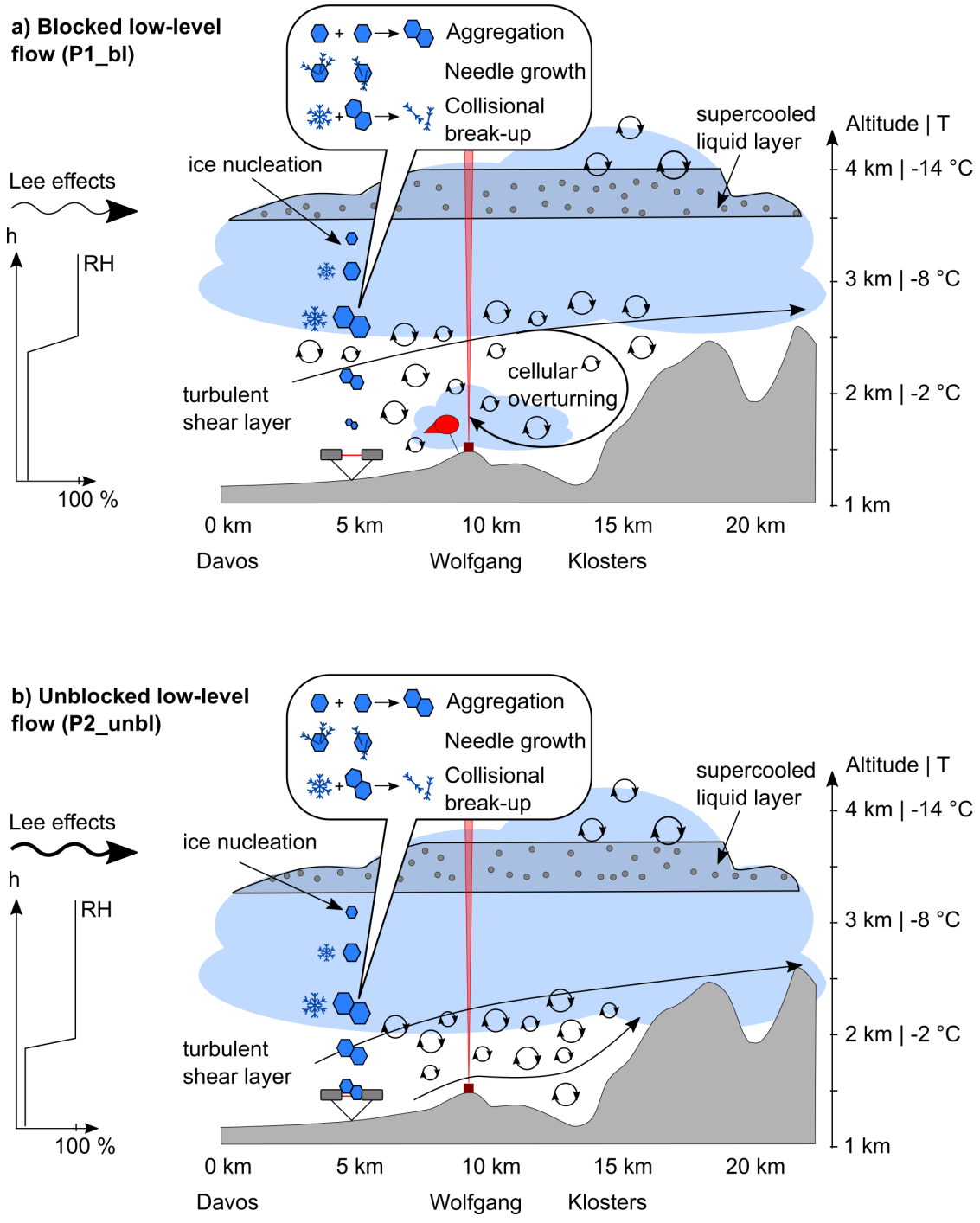

Figure 3.13: Conceptual overview of the dynamical and microphysical processes observed in the cloud during a low-level blocked flow (a) and unblocked flow (b).

oli et al., 2015), where they could continue growing to precipitation-sized particles and act as a seed to trigger secondary ice production. The Hallett-Mossop process was likely not occurring in the present case study due to the lack of supercooled liquid water in the turbulent shear layer. Rather collisional ice multiplication of fragile ice crystals (i.e., needles, dendrites) may have been responsible for the increase in the LDR and in the radar reflectivity within the turbulent shear layer. Additionally, a few laboratory-based studies suggested that ice fragmentation upon sublimation can lead to the production of secondary ice particles (e.g., Oraltay and Hallett, 1989; Dong et al., 1994; Bacon et al., 1998). However, secondary ice particles that formed within a subsaturated environment need to be transported to an ice supersaturated environment to influence the cloud microphysics (Korolev et al., 2020). In order to further investigate the role of secondary ice production in the turbulent shear layer, in situ observations of the cloud properties would be useful. Unfortunately, the tethered balloon system was limited to lower altitudes and could not sample the cloud properties within the upper part of the shear layer.
While previous research has mainly focused on a single mountain barrier, here we studied the role of low-level blocking and shear-induced turbulence on the microphysics of a mixed-phase cloud in a more complex terrain with narrow valleys and a series of mountain barriers. We found that the height of the shear layer and the cloud base and as a consequence the amount of precipitation in the valley were determined by the strength of the cross-barrier flow and low-level blocking. Furthermore, we found that local flow effects in mountain valleys (i.e., overturning cell due to blocked low-level flow) can induce the formation of low-level feeder clouds, which can enhance orographic precipitation through the seeder-feeder mechanism. Thus, this case study demonstrates that it can be challenging to study 'simple' conceptual mechanisms in complex terrain, due to numerous interactions between dynamics, microphysics and orography on different scales and the superposition of upstream and downstream effects. Nevertheless, it is important to perform field campaigns in complex terrain in order to improve our understanding of these processes and of orographic precipitation. Field campaigns in complex terrain should be designed in such a way that an extensive set of complementary instruments are deployed over the measurement area. The present observations were obtained in a region of 10 km $\times$ 10 km and mostly focused on the vertical structure. Information about the horizontal cloud structure (e.g., radar RHI scans, in situ aircraft observations) and observations over a larger area (e.g., covering the entire region between upstream and downstream mountain barriers) would be beneficial to obtain a more complete picture of the cloud dynamics and microphysics.

3.6 Conclusions

In this paper, we studied the influence of low-level flow blocking and shear-induced turbulence on the microphysics of a mixed-phase cloud in an inner-Alpine valley. Observations from a multi-dimensional set of ground-based remote sensing, balloon-borne in situ and ground-based precipitation instruments were analyzed, which were acquired during the RACLETS campaign in the Swiss Alps. The key findings are summarized as follows:

- The dynamical and microphysical structure of a mid-level cloud was characterized using ground-based remote sensing instrumentation (e.g., Ka-band polarimetric cloud radar, Ra-

man lidar, radar wind profiler). The wind profiler observations indicated the transition from a blocked to an unblocked low-level flow during the observational period and the presence of a shear-induced turbulent layer, which separated the blocked layer in the valley from the stronger cross-barrier flow. A supercooled liquid layer was embedded near cloud top, which provided a favorable environment for ice nucleation and growth. Changes in the microphysical cloud properties were observed within the turbulent shear layer including enhanced LDRs (i.e., change in particle shape) and increased radar reflectivities (i.e., enhanced ice growth). Our results are consistent with previous studies that have observed enhanced ice growth and precipitation formation through riming and aggregation in turbulent layers. In addition, based on the enhanced LDR and the ice particle habits observed at the surface, we suggest that needle growth on existing ice particles occurred within the turbulent layer and that collisions of these fragile ice crystals (e.g., dendrites, needle-like structures) with large ice particles might have caused mechanical break-up and the subsequent production of small secondary ice particles. These ice fragments have the potential to recirculate in the shear layer and influence the cloud microphysics aloft. However, this process could not be directly measured in this study. Further studies are required to investigate the role of secondary ice production mechanisms in turbulent shear layers.

- The altitude of the shear layer was determined by a complex interplay of upstream and downstream effects. For example, the shear layer was observed to lower as stronger cross-barrier flow moved over the upstream mountain barrier and the low-level blocking weakened. The cloud base was found to be associated with the shear layer. Precipitation was only observed in the valley when the shear layer was at its lowest altitude. The resulting lower cloud base altitude reduced the time that the ice particles spent in the subsaturated environment, ultimately allowing for the precipitation to reach the surface. Thus, we propose that the amount of precipitation observed in a mountain valley is influenced by several factors such as (1) the strength of the cross-barrier flow and low-level blocking, (2) the vertical position of the turbulent shear layer and cloud base and (3) the thermodynamic state of the boundary layer.

- In situ instrumentation on a tethered balloon system observed a low-level feeder cloud, which dissipated when the low-level flow turned from a blocked to an unblocked state. We suggest that an overturning cell formed as a consequence of the low-level flow impinging on the downstream mountain barrier. As a small-scale topographic feature was located upstream of the mountain barrier, we suggest that the generated counterflow (i.e., blocked flow) was forced to rise over the local topography and thereby acted as an updraft source and as a driving force for the formation of a low-level feeder cloud. Although the feeder cloud did not enhance precipitation in the present case (due to the dry boundary layer aloft), we propose that local flow effect such as low-level blocking can induce the formation of feeder clouds in other mountain valleys or on the leeward slope of foothills upstream of the main mountain barrier, where they can enhance orographic precipitation through the seeder-feeder mechanism.

Appendix

3.A Froude number

The dynamical response of a stable flow encountering a mountain barrier depends on the strength of the upstream airflow, the thermodynamic stability of the flow and the height of the mountain barrier. These components can be combined into a dimensionless number (Froude number; e.g., Colle et al., 2013):

$$Fr = \frac{U}{hN} \tag{3.2}$$

where U is the wind speed perpendicular to the mountain barrier, h is the height of the mountain barrier and N is the Brunt-Väisälä frequency, which is a measure for the atmospheric stability. If the Froude number is large ($Fr \gg 1$), the air flow can rise over the mountain barrier. When the Froude number is small (Fr $\ll 1$), the upstream flow is blocked and cannot ascend over the mountain barrier. The parameters to calculate the Froude number for the periods P1_bl (16 - 17:45 UTC), P2_unbl (17:45 - 18:40 UTC) and P3_bl (18:40 - 20 UTC) are given in Table 3.1.

Table 3.1: Parameters used to calculate the Froude number during P1_bl, P2_unbl and P3_bl.

	Wolfgang		Weissfluhjoch				
	T (°C)	p (hPa)	T (°C)	p (hPa)	U ($m\,s^{-1}$)	N (s^{-1})	Froude number
P1_bl	0.1	827.7	-5.2	725.6	7.6	0.013	0.75
P2_unbl	-0.1	828.4	-5.6	726.4	9.3	0.012	0.94
P3_bl	-0.2	829.2	-5.9	726.8	6.7	0.012	0.69

The effective terrain height h between the valley and the mountain barrier (2700 m) was around 800 m (see B2 in Fig. 3.1b). The wind speed was obtained from the radar wind profiler and averaged over the 1600 - 2800 m height interval. The temperature and pressure were measured at Wolfgang (1630 m) and at Weissfluhjoch (2700 m) and a linear temperature gradient was assumed between the two measurement locations. The calculated Froude numbers were below 1 for all periods, indicative for a blocked low-level flow. The Froude number increased during P2_unbl (to 0.94), suggesting a weakening of the blocking.

3.B Correlation between dynamics, microphysics and precipitation

To quantify the interactions between dynamics, microphysics and precipitation, correlation coefficients were calculated between the different parameters of Figure 3.9 (see Table 3.2).

Table 3.2: Correlation between (1) the height of the $10\,\mathrm{m\,s^{-1}\,km^{-1}}$ wind shear contour line, (2) the height of maximum radar reflectivity and (3) the precipitation rate measured at Wolfgang. The Spearman's rank correlation coefficient ρ and their p-Values are shown. The correlation coefficients were calculated between 16:45 UTC and 18:30 UTC. A time lag of 10 min was applied to the precipitation measurements.

	Spearman's rank correlation coefficient ρ (p-Value)		
	Height shear layer	Height max. reflectivity	Precipitation rate
Height shear layer	-	0.62 (<0.001)	-0.76 (<0.001)
Height max. reflectivity	0.62 (<0.001)	-	-0.55 (<0.001)
Precipitation rate	-0.76 (<0.001)	-0.55 (<0.001)	-

A moderate positive Spearman's rank correlation ($\rho = 0.62$) was observed between the shear layer height and the altitude of maximum radar reflectivity. On the other hand, a negative correlation was found between the precipitation rate and the shear layer height (ρ = -0.76) and altitude of maximum radar reflectivity (ρ = -0.55). All correlations were significant at the 5% confidence level. The moderate to strong correlations between dynamics, microphysics and precipitation parameters suggest that interactions between dynamical and microphysical processes were active within the turbulent shear layer, which enhanced ice growth and precipitation formation.

Acknowledgments

The authors would like to thank the participants of the RACLETS campaign for their technical support and many fruitful discussions. In particular, we are thankful to Michael Lehning (WSL/SLF, EPFL) and his whole team for their substantial support for realizing the RACLETS campaign by providing local contacts and support in requesting the necessary permissions. We would like to thank Paul Fopp for providing his land for the RACLETS campaign. We would also like to thank Alexander Beck for helping with the organization of the field campaign. Moreover, the authors are thankful to Susanne Crewell (University of Cologne) and Bernhard Pospichal (University of Cologne) for their help in interpreting the microwave radiometer data.We would also like to acknowledge Benjamin Walter (SLF) for providing data of the snowdrift station located at Gotschnagrat. We thank the Swiss Federal Office of Meteorology and Climatology MeteoSwiss for providing the meteorological measurements, ceilometer data from Klosters, MASC observations and access to the COSMO1 and weather radar data. Furthermore, we would also like to thank Eberhard Bodenschatz (MPI Goettingen) for his technical support during the development of the HoloBalloon platform. We would like to thank the Federal Office of Civil Aviation, particularly Judith Baumann and Jeroen Kroese, for their pragmatic approach

in obtaining the flight permit. FR, JH, AL, JP, JW and UL acknowledge funding from the Swiss National Science Foundation (SNSF) grant number 200021_175824. RD would like to acknowledge funding from the European Research Council (ERC) through Grant StG 758005.

Chapter 4

Microphysical investigation of the seeder and feeder region of an Alpine mixed-phase cloud

F. Ramelli[1], J. Henneberger[1], R. O. David[2], J. Bühl[3], M. Radenz[3], P. Seifert[3], J. Wieder[1], A. Lauber[1], J. T. Paquier[1], R. Engelmann[3], C. Mignani[4], M. Hervo[5] and U. Lohmann[1]

[1] Department of Environmental System Sciences, Institute for Atmospheric and Climate Science, ETH Zurich, Zurich, Switzerland
[2] Department of Geosciences, University of Oslo, Oslo, Norway
[3] Leibniz Institute for Tropospheric Research, Leipzig, Germany
[4] Institute of Environmental Geosciences, University of Basel, Basel, Switzerland
[5] Federal Office of Meteorology and Climatology MeteoSwiss, Payerne, Switzerland

This manuscript is in review for Atmospheric Chemistry and Physics.
DOI: https://doi.org/10.5194/acp-2020-772

Abstract

The seeder-feeder mechanism has been observed to enhance orographic precipitation in previous studies. However, the microphysical processes active in the seeder and feeder region are still being understood. In this paper, we investigate the seeder and feeder region of a mixed-phase cloud passing over the Swiss Alps, focusing on (1) fallstreaks of enhanced radar reflectivity originating from cloud top generating cells (seeder region) and (2) a persistent low-level feeder cloud produced by the boundary layer circulation (feeder region). Observations were obtained from a multi-dimensional set of instruments including ground-based remote sensing instrumentation

(Ka-band polarimetric cloud radar, microwave radiometer, wind profiler), in situ instrumentation on a tethered balloon system and ground-based aerosol and precipitation measurements.
The cloud radar observations suggest that ice formation and growth was enhanced within cloud top generating cells, which is consistent with previous observational studies. However, uncertainties exist regarding the dominant ice formation mechanism within these cells. Here we propose different mechanisms that potentially enhance ice nucleation and growth in cloud top generating cells (convective overshooting, radiative cooling, droplet shattering) and attempt to estimate their potential contribution from an ice nucleating particle perspective. Once ice formation and growth within the seeder region exceeded a threshold value, the mixed-phase cloud became fully glaciated.
Local flow effects on the lee side of the mountain barrier induced the formation of a persistent low-level feeder cloud over a small-scale topographic feature in the inner-Alpine valley. In situ measurements within the low-level feeder cloud observed the production of secondary ice particles likely due to the Hallett-Mossop process and ice particle fragmentation upon ice-ice collisions. Therefore, secondary ice production may have been partly responsible for the elevated ice crystal number concentrations that have been previously observed in feeder clouds at mountain-top observatories. Secondary ice production in feeder clouds can potentially enhance orographic precipitation.

4.1 Introduction

Mixed-phase clouds (MPCs), which consist of ice crystals and supercooled cloud droplets, play a crucial role for precipitation formation and are responsible for 30 % to 50 % of the precipitation in the mid-latitudes (Mülmenstädt et al., 2015). Furthermore, MPCs have important implications for the Earth's radiation budget. In particular, the phase partitioning between the liquid and ice phase in MPCs is of major importance, as the radiative properties of ice crystals and cloud droplets differ significantly (Sun and Shine, 1994). Thus, in order to understand the radiative effects and precipitation initiation in MPCs, it is important to understand the microphysical processes that govern MPCs as well as to characterize the vertical distribution of the liquid and ice phase hydrometeors within them.
The coexistence of the ice and liquid phase in MPCs is thermodynamically unstable due to the lower saturation vapor pressure over ice compared to over liquid. Therefore, ice crystals grow rapidly at the expense of the surrounding water droplets if the saturation vapor pressure lies between ice and water saturation. This process is known as the Wegener-Bergeron-Findeisen (WBF) process (Wegener, 1911; Bergeron, 1935; Findeisen, 1938) and can lead to rapid glaciation of the cloud and thus limits the lifetime of MPCs.
In order to sustain mixed-phase regions, two prerequisites need to be fulfilled. Firstly, the environment needs to be supersaturated with respect to liquid water, which can be achieved through sufficiently large updrafts (e.g., Rauber and Tokay, 1991; Harrington et al., 1999). Secondly, the condensate supply rate needs to exceed the diffusional growth rate of the ice crystals. Indeed, persistent MPCs are frequently observed in mountainous regions (e.g., Borys et al., 2003; Lowenthal et al., 2011; Dorsi et al., 2015; Lloyd et al., 2015; Lohmann et al., 2016a; Beck et al., 2017; Lowenthal et al., 2016; Lowenthal et al., 2019) where the local topography

produces updrafts capable of providing a continuous source of condensate. In addition, Rauber and Grant (1986) found two further regions where the prerequisites for persistent MPCs are fulfilled: near cloud top and near cloud base. The presence of a supercooled liquid layer at cloud top can increase radiative cooling (e.g., Sun and Shine, 1994; Possner et al., 2017; Eirund et al., 2019). Furthermore, this liquid layer can act as a source region for primary ice nucleation and initial ice growth (i.e., seeder region) and can influence the evolution of the microphysical cloud structure in the lower cloud levels. Meanwhile, the presence of a supercooled liquid layer near cloud base can act as a feeder region on which precipitation particles that formed in the seeder region of the cloud can "feed" on, ultimately enhancing precipitation (e.g., Reinking et al., 2000; Borys et al., 2000; Borys et al., 2003; Lowenthal et al., 2011; Lowenthal et al., 2016; Lowenthal et al., 2019).

Seeder regions were often observed in connection with cloud top generating cells (e.g., Hogan et al., 2002; Cronce et al., 2007; Stark et al., 2013; Kumjian et al., 2014; Rosenow et al., 2014; Plummer et al., 2014; Plummer et al., 2015; Rauber et al., 2015). The term "generating cell" describes a small region of enhanced radar reflectivity at cloud top, which produces an enhanced reflectivity trail, or fallstreak, characteristic of falling hydrometeors. Generating cells have horizontal extents of 1 - 2 km and updraft velocities in the range of 0.75 - 3 m s^{-1} (Rosenow et al., 2014; Kumjian et al., 2014). Most studies agree that radiative cooling at cloud top is a major driver for the formation and maintenance of generating cells (e.g., Kumjian et al., 2014; Keeler et al., 2016) and that these cells play an important role in primary ice nucleation and growth (e.g., Houze Jr et al., 1981; Hogan et al., 2002; Stark et al., 2013). Moreover, secondary ice production (SIP) processes might be active in generating cells, which can further increase the ice crystal number concentration (ICNC). Indeed, generating cells were found to only account for 10 - 20 % of the total ice growth (e.g., Houze Jr et al., 1981; Plummer et al., 2015), while the majority of the ice growth occurred in the feeder region below.

Ice crystals can grow by various ice processes depending on the ambient conditions and the size distribution of cloud droplets and ice crystals (e.g., Marshall and Langleben, 1954; Fukuta and Takahashi, 1999; Bailey and Hallett, 2009; Connolly et al., 2012). For example, small ice crystals grow initially by diffusion of water vapor and thus their habit is determined by the ambient temperature and supersaturation (Magono and Lee, 1966; Bailey and Hallett, 2009). When ice crystals reach a critical size, they can grow more efficiently by aggregation and riming. Aggregation involves the collision and coalescence between ice particles and is most efficient at temperatures higher than -10 °C due to the presence of a thicker quasi-liquid layer, which enhances the stickiness of the ice particles (e.g., Lohmann et al., 2016b). Riming, which involves the collision of an ice particle with a supercooled cloud droplet that freezes upon contact, has often been observed in the feeder regions of clouds (Mitchell et al., 1990; Borys et al., 2000; Borys et al., 2003; Saleeby et al., 2009; Saleeby et al., 2011; Lowenthal et al., 2011; Lowenthal et al., 2019) and has been found to enhance surface precipitation by up to 20 - 50 % (e.g., Mitchell et al., 1990; Borys et al., 2003; Lowenthal et al., 2016). For example, Lowenthal et al. (2016) observed that the precipitation at a mountain-top observatory gained the majority of its mass within 1 km above the mountain-top in the so-called feeder cloud. The efficiency of riming strongly depends on the cloud droplet size distribution (e.g., Borys et al., 2003; Saleeby et al.,

2013). Additionally, riming can also produce a large number of ice splinters; e.g., when a cloud droplet of an appropriate size ($> 25\,\mu m$ in diameter) collides with a rimed ice particle ($> 0.5\,mm$ in diameter) (Mossop, 1978; Lamb and Verlinde, 2011). This SIP process is called the Hallett-Mossop process (Hallett and Mossop, 1974) and is thought to be active at temperatures between -3 °C and -8 °C. Other SIP mechanisms include the fragmentation of fragile ice crystals upon collisions with large ice particles (Vardiman, 1978) and the release of small secondary ice particles upon freezing of drizzle-sized droplets (e.g. Langham and Mason, 1958; Mason and Maybank, 1960; Lauber et al., 2018). Indeed, the ICNCs measured in feeder clouds at mountain top research stations frequently exceed the observed ice nucleating particle (INP) concentrations by several orders of magnitude (e.g., Rogers and Vali, 1987; Lloyd et al., 2015; Beck et al., 2018; Lowenthal et al., 2019). Several studies suggested that this discrepancy between the INP concentration and the ICNC can be explained by the influence of surface processes such as blowing snow (Geerts et al., 2015; Beck et al., 2018), hoar frost (Lloyd et al., 2015) or riming on snow-covered surfaces (Rogers and Vali, 1987), which can significantly increase the local ICNC and thereby influence the further evolution of the cloud. So far, it has been difficult to disentangle the contribution of surface processes and SIP mechanisms to the observed ICNC by means of mountain top observations. Therefore, innovative measurement strategies that are located far enough from mountain-tops or mountain slopes are required to reduce the influence of surface processes and to assess the importance of SIP mechanisms and their implications for precipitation formation in feeder clouds.

In this study, we investigate the microphysics of a cloud system passing over the Swiss Alps by combining a multi-dimensional set of instruments. A particular emphasis is placed on studying the role of cloud top generating cells and a surface-decoupled feeder cloud for ice growth and precipitation initiation. While most of the studies agree that generating cells have important implications for precipitation formation, less research has focused on the mechanisms that are responsible for the enhanced ice formation and growth within these cells. We will approach this problem from an INP-cloud perspective, by combining INP and ice crystal measurements. Furthermore, we discuss the role of a low-level feeder cloud for ice growth and SIP processes. While the lowest part of the boundary layer is usually inaccessible for aircraft in complex terrain or is limited to observations at mountain-tops, we analyze the microstructure of the low-level feeder cloud by using a tethered balloon system. The presented case study was observed during the Role of Aerosols and CLouds Enhanced by Topography on Snow (RACLETS) campaign, which took place in the Swiss Alps during February and March 2019. The analysis is based on an extensive set of observations including (1) ground-based remote sensing observations from a cloud radar, microwave radiometer and wind profiler, (2) balloon-borne in situ observations, (3) INP measurements and (4) surface-based precipitation measurements.

4.2 Measurement location and instruments

The data presented in this paper was collected during the RACLETS campaign, which took place in the Swiss Alps in the region around Davos from 8 February 2019 to 28 March 2019 and was designed to observe the pathways of precipitation formation covering the entire aerosol-cloud-precipitation process chain.

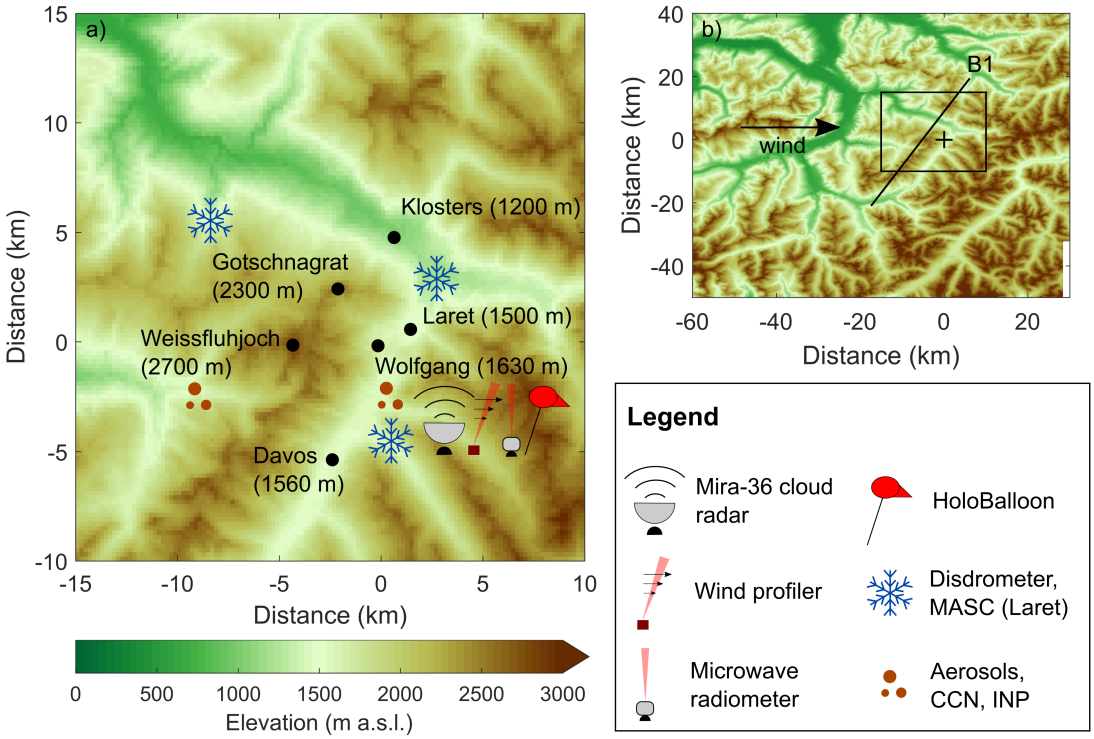

Figure 4.1: Overview of the measurement locations and the experimental setup (a). The geographical location of Wolfgang (black cross) and the surrounding topography is shown in (b). The large-scale wind direction was from the west as indicated by the black arrow. The most relevant mountain barrier is indicated by B1. An enlarged section of the measurement sites (black rectangle in b) and the instrument setup is shown in panel (a). The elevation data was obtained from the digital height model DHM25 of the Federal Office of Topography swisstopo: `https://shop.swisstopo.admin.ch/de/products/height_models/dhm25200`, last access: 9 March 2020.

Observations of the cloud microphysics were conducted at Wolfgang (1630 m; see Fig. 4.1) using remote sensing and in situ instruments. Ground-based remote sensing measurements were obtained with a vertically-pointing Ka-band polarimetric cloud radar (Mira-36 METEK GmbH, Germany; Görsdorf et al., 2015), which provided vertical profiles of radar reflectivity factor, Doppler velocity, spectral width and linear depolarization ratio (LDR). The radar observations have a vertical resolution of 31.17 m and a temporal resolution of 10 s. Moreover, a 14-channel microwave radiometer (HATPRO, Radiometer Physics GmbH, Germany; Rose et al., 2005) was used to observe vertical profiles of atmospheric temperature and humidity as well as the column integrated water vapor content (IWV) and liquid water path (LWP). Furthermore, the three-dimensional wind field was measured at Wolfgang using a radar wind profiler (LAP-3000 Wind profiler, Vaisala, US). The wind profiler data has a vertical resolution of 200 m and a temporal resolution of 5 min. In situ observations of the vertical low-level cloud structure were measured with the tethered balloon system HoloBalloon (Ramelli et al., 2020). The main component of the measurement platform is the HOLographic cloud Imager for Microscopic Objects (HOLIMO), which can image an ensemble of cloud particles in the size range from small cloud droplets (6 µm) to precipitation-sized particles (2 mm) in a three-dimensional sample volume (Henneberger et al., 2013; Beck et al., 2017; Ramelli et al., 2020). HOLIMO provides information about the phase-resolved particle size distribution and particle habit. As in Henneberger

et al. (2013) and Beck et al. (2017), partitioning between cloud droplets and ice crystals was applied to particles larger than 25 µm, i.e., particles smaller than 25 µm were classified as cloud droplets. In the present study, cloud droplets were classified using support vector machines, whereas the ice particles were classified visually (manual classification) in order to reduce the number of misclassified ice particles. Thus, because of the applied size threshold (25 µm) and the visual classification, the reported ice properties (e.g., ICNC, IWC) can be considered as a lower estimate. Additionally, the ICNC was derived from the remote sensing observations with the method of Bühl et al. (2019). The particle diameter was estimated from the particle terminal fall velocity and spectral width measured with the cloud radar. For this case, the particle shapes from Mitchell (1996) were used, assuming 'hexagonal plates' for ice crystals smaller than 600 µm in diameter and 'aggregates of planar polycrystals in cirrus clouds' for ice particles larger than 600 µm in diameter. The particle shape was derived from LDR measurements of the cloud radar and the images of ice crystals reconstructed from HOLIMO. The uncertainty of the retrieved ICNC is one order of magnitude.

Precipitation was measured at three locations (Wolfgang 1630 m, Laret 1500 m, Gotschnagrat 2300 m; see Fig. 4.1) using Particle Size Velocity (Parsivel) disdrometers (OTT Parsivel2, OTT HydroMet, Germany; Tokay et al., 2014). Parsivel disdrometers can measure both the size and the fall velocity of hydrometeors that fall through a laser sheet (Löffler-Mang and Joss, 2000). The size of the hydrometeor is estimated from the signal attenuation, whereas the fall velocity of the hydrometeor is obtained from the signal duration. Using the single particle size - fall velocity relationship, the observed particles can be classified into different hydrometeor classes, by applying different hydrometeor-dependent parameterizations (e.g., Yuter et al., 2006). Precipitation particles in the size range between 0.2 mm and 25 mm are measured. The temporal resolution of the measurements is 30 s. Additionally, a Multi-Angle Snowflake Camera (MASC; Garrett et al., 2012) was installed at Laret (see Fig. 4.1), which took photographs of hydrometeors from three different angles and simultaneously measured their fall velocity. The MASC is sensitive to hydrometeors in the size range between 100 µm and 10 cm. Furthermore, a snow drift station was installed at Gotschnagrat, which provided data about wind-driven redistribution of snow (Walter et al., 2020).

Lastly, aerosols and INP properties were measured at the valley station Wolfgang (1630 m) and at the mountain-top station Weissfluhjoch (2700 m) (see Fig. 4.1). Aerosol instruments were connected to heated inlets for measurements of ambient air at each site. Additionally, ambient aerosols were collected approximately every 1.5 h with a high flow rate impinger (Coriolis μ, Bertin Technologies, France, operation at 300 lpm for 20 mins; Carvalho et al., 2008). The impinger collected aerosol particles larger than 0.5 µm in swirling liquid water and the aqueous solution was analyzed in drop-freezing instruments in order to obtain INP concentration spectra from 0 °C to approximately -20 °C. The DRoplet Ice Nuclei Counter Zurich (DRINCZ; David et al., 2019a) was operated at Wolfgang and the LED-based Ice Nucleation Detection Apparatus (LINDA; Stopelli et al., 2014) was run at Weissfluhjoch. Both drop-freezing instruments use a digital camera to detect freezing by a change in the light transmission through the aqueous solution. An intercomparison study was conducted between DRINCZ and LINDA. The differences in observations were within the instrumental uncertainty.

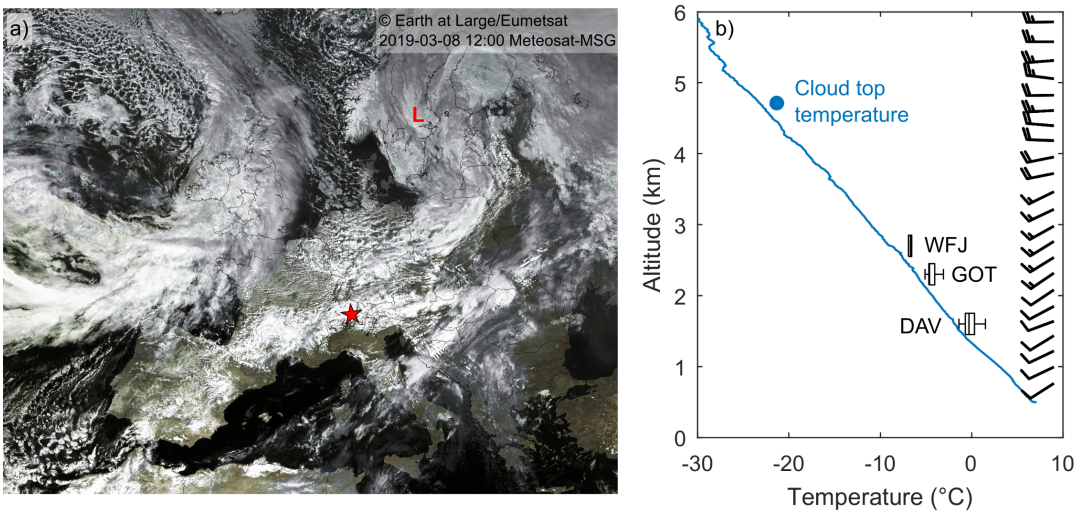

Figure 4.2: Overview of the synoptic weather situation on 8 March 2019, showing a satellite picture taken over Europe at 12 UTC (a, Eumetsat) and the vertical temperature profile measured by a radiosonde (12 UTC) launched from Payerne (b, MeteoSwiss). The boxplots in (b) indicate the temperature measured at the weather stations Davos (DAV, 1600 m), Gotschnagrat (GOT, 2300 m) and Weissfluhjoch (WFJ, 2700 m) during the passage of the cloud system. The blue dot indicates the cloud top temperature (-21 °C) and cloud top height (4700 m), which was estimated from the cloud radar observations averaged between 16 UTC and 18 UTC. The wind barbs are shown on the right side.

The cumulative INP concentration was calculated following eq. (4) in Vali (2019):

$$INPC(T) = -\frac{\ln(1 - FF(T))}{V_a \cdot C}, \tag{4.1}$$

$$\text{where} \quad C = \frac{F_{\text{impinger}} \cdot t_{\text{sample}}}{V_{\text{liquid}}} \cdot C_{\text{stdL}} \tag{4.2}$$

$$\text{and} \quad C_{\text{stdL}} = \frac{p_{\text{ambient}}}{p_{\text{ref}}} \cdot \frac{T_{\text{ref}}}{T_{\text{ambient}}} \tag{4.3}$$

using the temperature-dependent frozen fraction $FF(T)$, the volume of an individual aliquot V_a (50 µL at Wolfgang, 100 µL at Weissfluhjoch) and the normalization factor C, which converts the concentration to standard liters of ambient air. C was calculated for each sample by considering the flow rate of the impinger F_{impinger} (300 lpm), the sampling time t_{sample} (usually 20 min), the end volume of the liquid V_{liquid} (approx. 15 mL) and the conversion factor from liters to standard liters C_{stdL} (including the ambient temperature T_{ambient} and pressure p_{ambient} at each site and the reference temperature $T_{\text{ref}} = 273.15\,\text{K}$ and pressure $p_{\text{ref}} = 1013.25\,\text{hPa}$). According to the specifications above, the minimal detectable concentration (limit of detection) at Wolfgang was $6.3 \cdot 10^{-4}\,\text{stdL}^{-1}$ and at Weissfluhjoch $3.5 \cdot 10^{-4}\,\text{stdL}^{-1}$.

4.3 Description of the case study

The synoptic weather situation over Europe on 8 March 2019 was characterized by a large-scale westerly flow with several low pressure systems (Fig. 4.2a). This strong westerly flow persisted for several days and brought moist air from the Atlantic towards central Europe. A low-pressure

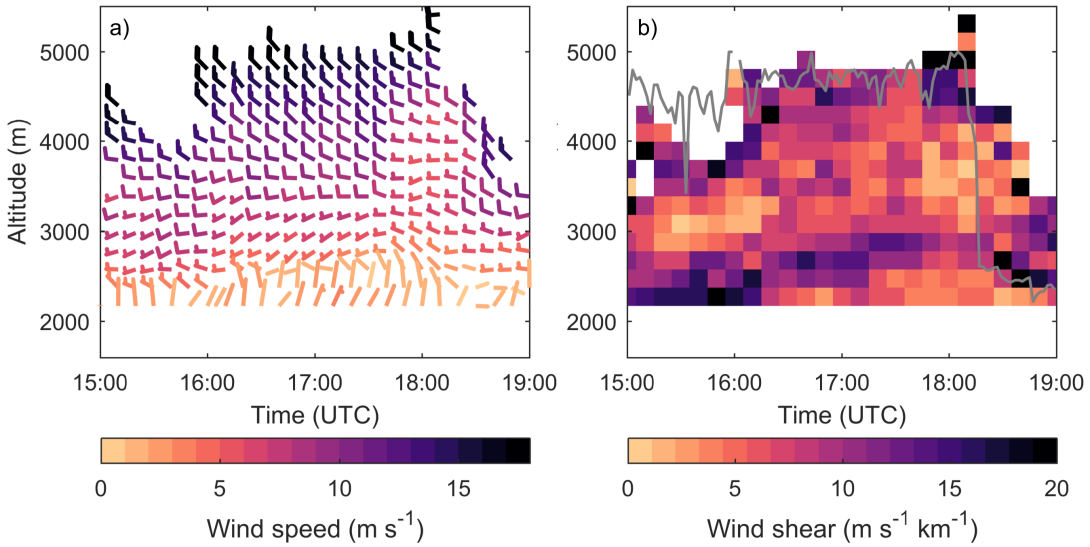

Figure 4.3: Observations of the wind speed and wind direction (a) and of the wind shear (b) measured by the radar wind profiler located at Wolfgang. The vertical wind shear (s) was calculated from the wind profiler observations, considering changes in the scalar wind speed and direction (u) between two adjacent height levels (z) ($s = \frac{u_2 - u_1}{z_2 - z_1}$). The gray line in (b) shows the cloud radar reflectivity contour of -30 dBZ, which indicates the cloud top height.

system located over Scandinavia produced a small-scale disturbance on its southern edge, which crossed Switzerland during the day and reached Davos in the afternoon. The presented case study was observed during the passage of this small-scale disturbance, which arrived in Davos at around 15 UTC and lasted until 19 UTC.

During the passage of the cloud system, the temperature at Davos decreased from 3 °C to -2 °C (ΔT = -5 °C) and the temperature at Weissfluhjoch decreased from -5 °C to -7.5 °C (ΔT = -2.5 °C). The vertical temperature profile of a radiosonde ascent is shown in Figure 4.2b. The radiosonde was launched from Payerne, which is located around 200 km upstream of Davos. The temperatures measured at Davos, Gotschnagrat and Weissfluhjoch were slightly warmer (1-2 °C) than the temperature measured by the radiosonde, but the observed lapse rate near Davos was in good agreement with the radiosonde profile measured at Payerne (see boxplots in Fig. 4.2b). A cloud top temperature of around -21 °C was estimated from the observed temperature profile, assuming the same temperature deviation as for the ground-based stations and a cloud top height of 4700 m (derived from the cloud radar observations averaged between 16 UTC and 18 UTC).

The horizontal wind fields were measured with a radar wind profiler at Wolfgang (Fig. 4.3a). In agreement with the Payerne sounding, the wind profiler showed a large-scale wind direction from the west with a mean wind speed in the range of 10 m s^{-1} to 15 m s^{-1} above 3000 m. Below 2400 m, the wind speed was lower (< 5 m s^{-1}) and the flow was coming from the north-east (confined by the Davos valley). This pattern in the low-level wind field can be explained by shielding effects due to the mountain barrier B1 located upstream of Wolfgang (Fig. 4.1b), resulting in a decoupled low-level flow in the lee of the mountain barrier. A strong decrease in wind speed was observed above 2700 m between 17:45 UTC and 18:30 UTC. In addition, the wind direction veered from 250° to 280° during this time period. This change in the wind pattern coincides with the period of the strongest precipitation event at Wolfgang (Fig. 4.4e) and could potentially

have contributed to the glaciation of the MPC. Furthermore, enhanced wind shear was observed near cloud top ($> 10\,\mathrm{m\,s^{-1}\,km^{-1}}$) with a maximum of $20\,\mathrm{m\,s^{-1}\,km^{-1}}$ corresponding to the most intense precipitation peak (cf. Fig. 4.3b, Fig. 4.4e). Another layer of enhanced wind shear was observed between 2500 m and 3000 m, due to the interaction of the large-scale flow with the mountain barrier B1 (Fig. 4.1).

4.4 Results and Discussion

4.4.1 Overview of the microphysical cloud structure

An overview of the observed microphysical cloud structure is shown in Figure 4.4. The radar reflectivity shows that the precipitation began at 15:10 UTC and was convective in nature (Fig. 4.4a). At around 17:30 UTC, the reflectivity increased at all altitudes and the highest precipitation rates were observed at the surface (Fig. 4.4e). The period of high reflectivity (> 10 dBZ) lasted for about one hour. After this period, the cloud top lowered from 5000 m to 2800 m and the precipitation ended shortly after 18:40 UTC. The bulk of the precipitation originated at cloud top as can be seen from the fallstreak pattern of enhanced radar reflectivity (> 10 dBZ, Fig. 4.4a). The contour frequency by altitude diagram (CFAD, Fig. 4.5) of the radar reflectivity (Fig. 4.5a) indicates a rapid increase in the radar reflectivity near cloud top, suggesting that the ice crystals were formed in the layer between 5000 m and 4000 m. The ice crystals rapidly grew to large sizes between 4000 m and 3000 m, before they partly sublimated in the layer between 3000 m and 2000 m, as indicated by the decreasing radar reflectivity (Fig. 4.4a and 4.5a) and Doppler velocity (Fig. 4.4b and 4.5b) below 3000 m (assuming horizontal homogeneity). The majority of upward motion was observed above 3500 m (Fig. 4.4b and 4.5b). It is important to note that the measured vertical Doppler velocity is the sum of the particle fall speed and the air motion. Thus, as the ice particles grow to larger sizes while falling towards the ground, their fall speed increases and therefore mask the updrafts more easily. The Doppler velocity CFAD shows large variations between -4 $\mathrm{m\,s^{-1}}$ to 2 $\mathrm{m\,s^{-1}}$ near cloud top (Fig. 4.5b), indicative of turbulent motions. Indeed, the strong variability in the Doppler velocity was collocated with the enhanced shear layer from the wind profiler (Fig. 4.3b). Furthermore, the spectral width was also enhanced locally near cloud top (Fig. 4.4c), which can be attributed to the presence of turbulence (see Fig. 4.4b) near cloud top. The occurrence of (1) high radar reflectivity fallstreaks (Fig. 4.4a), (2) positive Doppler velocities (Fig. 4.4b) and (3) increased spectral width (Fig. 4.4c) near cloud top, suggest the presence of cloud top generating cells. Cloud top generating cells can enhance ice nucleation and growth and as such have important implications for precipitation formation (e.g., Houze Jr et al., 1981; Hogan et al., 2002; Evans et al., 2005; Ikeda et al., 2007; Crosier et al., 2014; Kumjian et al., 2014; Plummer et al., 2014; Rosenow et al., 2014; Plummer et al., 2015; Rauber et al., 2015) as will be further discussed in Section 4.4.2.

Ice particles that formed within the seeder region interact with other cloud particles while falling through the cloud and thus influence the microphysics of the feeder region below. The low-level cloud structure was observed with the tethered balloon system HoloBalloon (see Fig. 4.6). The balloon-borne measurements indicate the presence of a low-level liquid layer that was confined to the lowest 300 m of the cloud (see Fig. 4.6). The cloud droplet number concentration (CDNC)

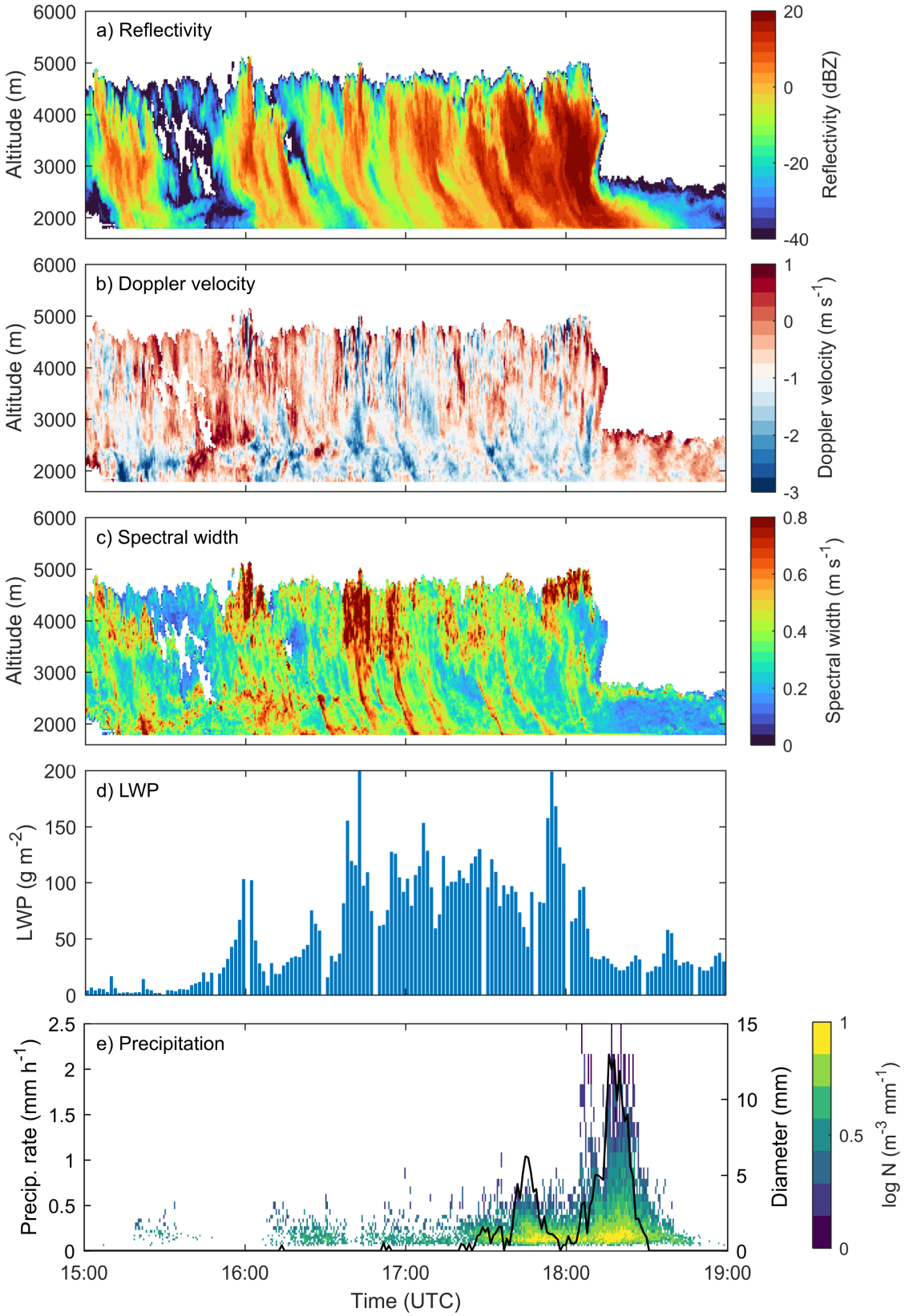

Figure 4.4: Observations of the cloud structure measured by the cloud radar (a-c) and the microwave radiometer (d) at Wolfgang on 8 March 2019. The cloud radar observations show the radar reflectivity (a), Doppler velocity (b) and spectral width (c). Note that the colorbar in (b) is centered at -1 m s^{-1} to approximately account for the hydrometeor fall speed. The column-integrated LWP measured by the microwave radiometer is shown in (d) and the precipitation measured by the disdrometer at Wolfgang (1630 m) is shown in panel (e).

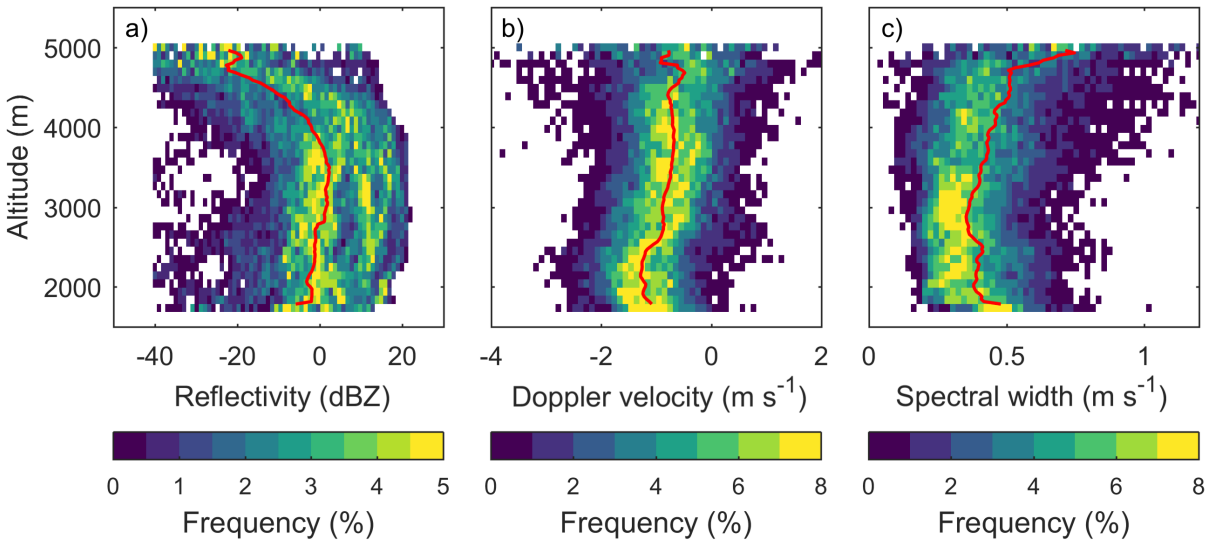

Figure 4.5: CFADs of the radar reflectivity (a), Doppler velocity (b) and spectral width (c) for the time period between 15:50 UTC and 18:20 UTC. The red line shows the mean vertical profile. The following bin sizes were applied: (1) radar reflectivity from -40 dBZ to 30 dBZ in 1 dBZ intervals, (2) Doppler velocity from -4 m s^{-1} to 3 m s^{-1} in 0.1 m s^{-1} intervals and (3) spectral width from 0 m s^{-1} to 1.2 m s^{-1} in 0.02 m s^{-1} intervals. A height interval of 100 m was used for all radar properties.

increased from 100 cm^{-3} to 350 cm^{-3} between 16 UTC and 17:45 UTC (Fig. 4.6a), before the CDNC decreased after 18 UTC. The mean cloud droplet diameter ranged between 8 µm and 12 µm as shown by the size distribution in Figure 4.7a. The ICNC was in the range of 1 L^{-1} to 4 L^{-1} between 16 UTC and 18 UTC (Fig. 4.6b). Ice crystals were especially observed when fallstreaks of enhanced radar reflectivity reached the surface. During the main precipitation event, after 18 UTC, the ICNC increased up to 14 L^{-1}. During the same time period, the ratio between the ice water content (IWC) and total water content (TWC), which is often used to characterize the cloud phase (e.g., Korolev et al., 2003; Lohmann et al., 2016a), increased from 0.05 - 0.3 (liquid to mixed-phase) to 0.9 (ice-phase). Thus, a transition from a mixed-phase low-level cloud (before 18 UTC) to an ice-dominated low-level cloud (after 18 UTC) was observed during the passage of the cloud system (Fig. 4.6c). The cloud radar and microwave radiometer observations suggest that the entire cloud layer glaciated, as an increase in the radar reflectivity (Fig. 4.4a) and a decrease in the LWP (Fig. 4.4d) was observed after 18 UTC. In the absence of sufficiently large updraft velocities for additional cloud droplet activation, the presence of large ice particles or high ICNC can lead to rapid glaciation of the cloud by the WBF process (Korolev and Isaac, 2003).

Even though downward motions were present on the lee side of the mountain barrier (see increased fraction of negative Doppler velocities in Fig. 4.5b), which contributed to hydrometeor evaporation/sublimation (see decreased reflectivity in Fig. 4.5a), a persistent low-level liquid layer was observed at Wolfgang. We suggest that this shallow low-level feeder cloud formed due to orographic lifting, as the low-level flow in the lee of the mountain barrier was decoupled from the large-scale flow (Fig. 4.3a) and was forced to rise from Klosters (1200 m) to Wolfgang (1630 m) over the local topography. It is assumed that this shallow cloud could not generate significant precipitation by itself, due to the limited time available for collision-coalescence of cloud

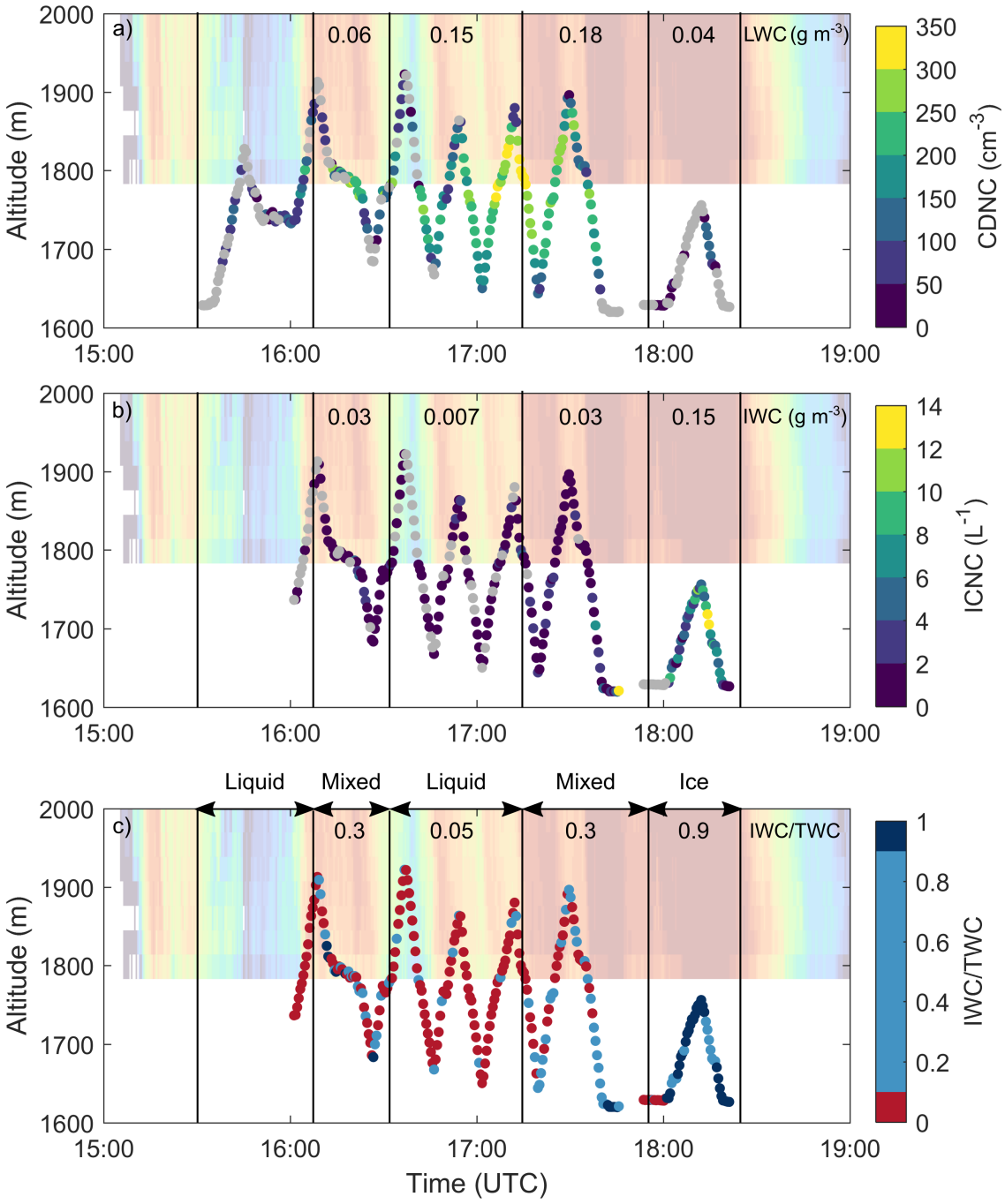

Figure 4.6: Vertical in situ profiles of the CDNC (a), ICNC (b) and the IWC/TWC ratio (c). The gray dots in (a) and (b) indicate measurement points, which are associated with a liquid water content (LWC) of $< 0.01\,\mathrm{g\,m^{-3}}$ (for CDNC) or an IWC of $0\,\mathrm{L^{-1}}$ (for ICNC). In (c), red colors represents liquid cloud regions (IWC/TWC < 0.1), light blue mixed-phase cloud regions ($0.1 \leq$ IWC/TWC < 0.9) and dark blue indicates ice cloud regions (IWC/TWC ≥ 0.9). The cloud radar reflectivity is shown in the background. The numbers in (a), (b) and (c) indicate the mean LWC, IWC and IWC/TWC ratio within the intervals defined by the black vertical lines.

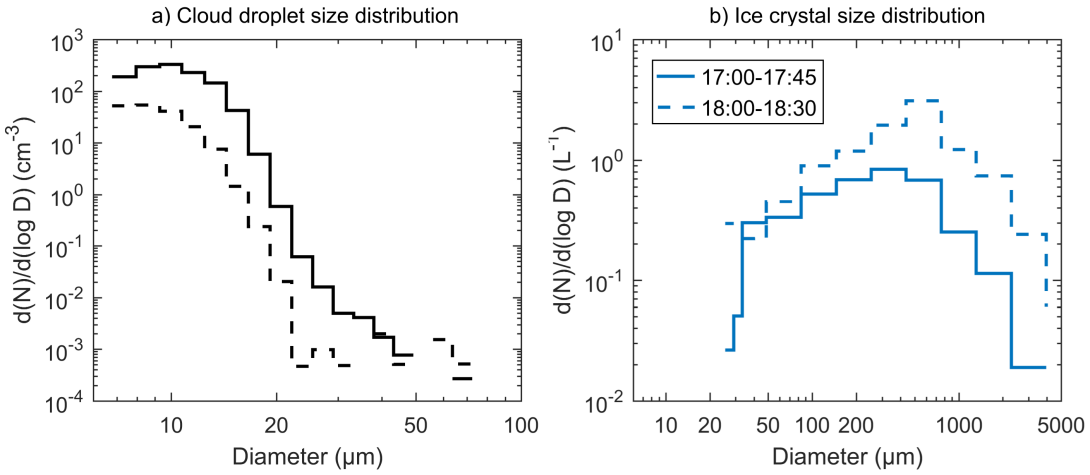

Figure 4.7: Cloud droplet (a) and ice crystal (b) size distributions observed with the HoloBalloon platform. The size distributions were averaged between 17 UTC and 17:45 UTC (solid line) and between 18 UTC and 18:30 UTC (dashed line).

droplets to produce precipitation-sized particles and due to the warm temperatures (> -3 °C), which were limiting the amount of INPs and thus ice formed through primary ice nucleation. However, the hydrometeors that formed in the generating cells can "feed" on the low-level liquid layer and thus enhance precipitation by riming and depositional growth. Additionally, it can provide an environment favorable for the production of secondary ice particles as will be discussed in Section 4.4.3. In the following section, we investigate the microphysics and dynamics in cloud top generating cells and explore the origin of ice crystals.

4.4.2 The origin and growth of ice crystals in cloud top generating cells

Observations from the cloud radar, microwave radiometer, HoloBalloon platform and ground-based aerosol measurements were combined to study the dynamics and microphysics within cloud top generating cells. Since no in situ observations within generating cells or near cloud top were available during the RACLETS campaign, the analysis of the microphysics was limited to observations from remote sensing instrumentation and balloon-borne in situ measurements near cloud base. In the first part of this section, the overall dynamical and microphysical structure of generating cells is characterized, whereas in the second part the origin of ice crystals and the microphysical growth processes active within generating cells are investigated from an INP-cloud perspective.

When the strongest generating cells were present, vertical overshooting of up to 500 m was observed at the cloud top (Fig. 4.8; e.g., at 16 UTC and 16:45 UTC), indicating the presence of strong updrafts. This was also supported by observations of the maximum Doppler velocity (Fig. 4.8b), which was derived from the Doppler spectra (see Appendix 4.A) and used as a proxy to identify updraft regions. The maximum Doppler velocity suggests that the strongest updrafts were present in the core regions of the cloud top generating cells ($> 3\,\mathrm{m\,s^{-1}}$), whereas updrafts were weaker outside of the generating cells and at altitudes below 3000 m (Fig. 4.8b). It is likely that liquid water was produced in these updraft cells, as a positive correlation was found between the vertically-integrated maximum Doppler velocity and the LWP measured by

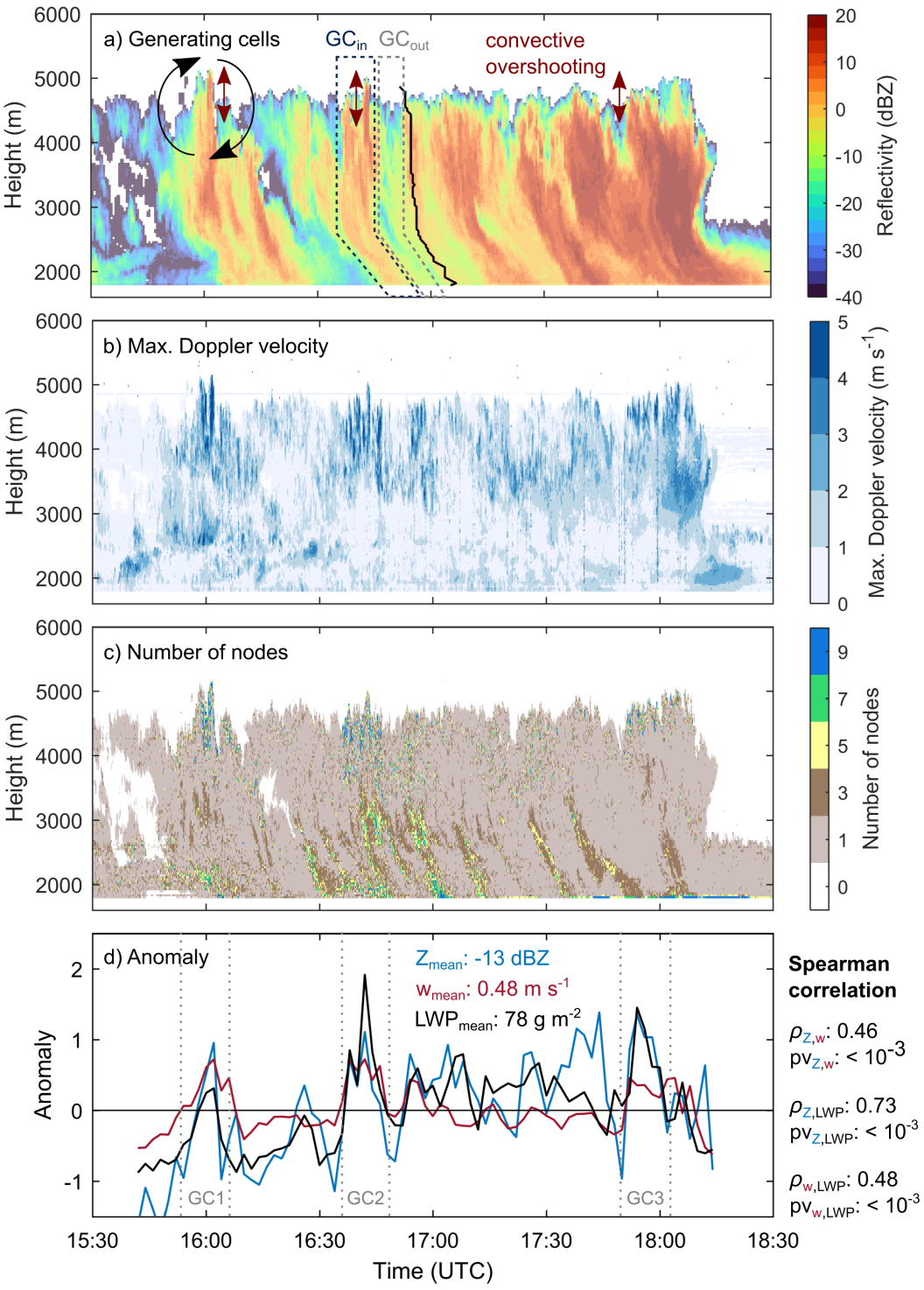

Figure 4.8: Time series of the radar reflectivity (a), maximum Doppler velocity (b) and number of nodes (c). The black line in panel (a) indicates the 17 UTC fallstreak, which was investigated in Fig. 4.9. The dashed lines indicate the regions inside (GC_{in}) and outside (GC_{out}) of GC2, which were used for the analysis in Appendix 4.B. The maximum Doppler velocity was derived from the Doppler spectra (see Appendix 4.A). The number of nodes were obtained from the peakTree analysis following the procedure described in Radenz et al. (2019). The evolution of the cloud top anomalies is shown in (d). The radar reflectivity (blue line) and spectral width (red line) were averaged over 600 m from the cloud top. The anomalies were normalized to the mean value, which is indicated in panel (d). The results of the Spearman's rank correlation are shown to the right of panel (d) with ρ indicating the correlation coefficient and pv the p-value of the Spearman's rank correlation.

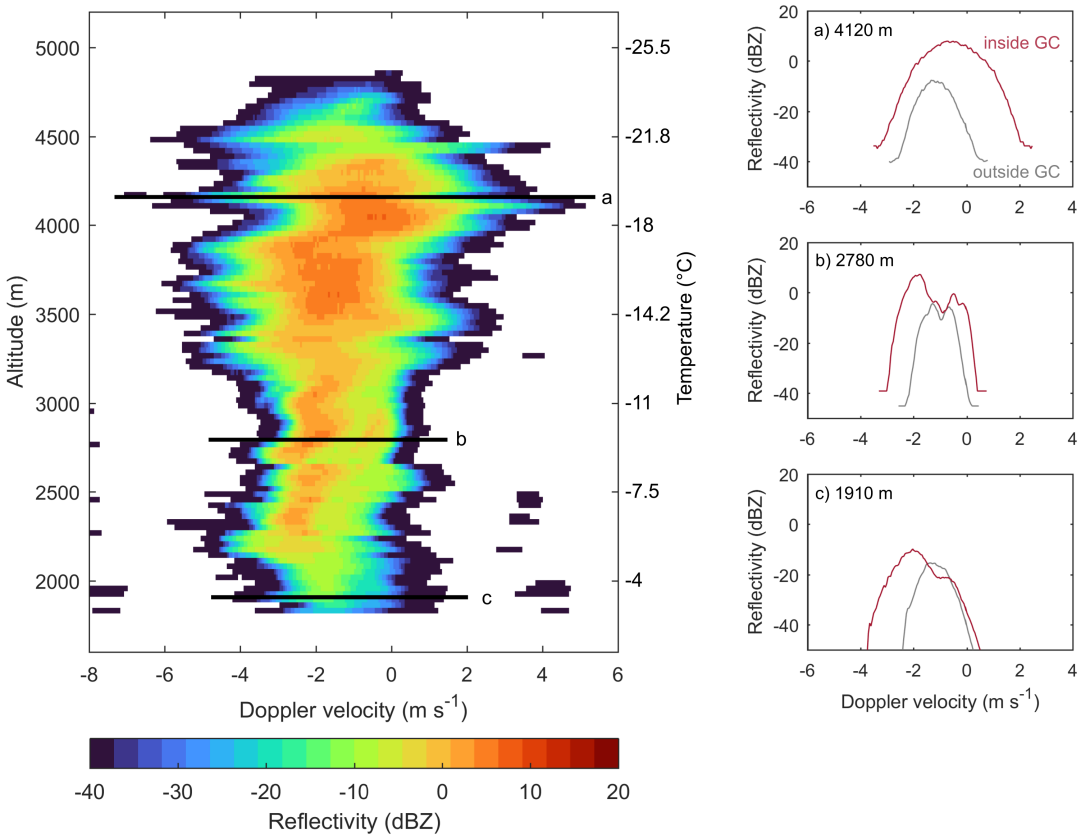

Figure 4.9: Vertical profile of the Doppler spectra along the 17 UTC fallstreak averaged over 1 min (indicated by black line in Fig. 4.8a). The Doppler spectra at three selected heights are shown on the right: 4120 m (within turbulent layer), 2780 m (at mountain barrier height), 1910 m (at balloon flight height). The red line indicates the Doppler spectrum inside the 17 UTC fallstreak, whereas the gray spectrum was measured before the fallstreak (inside GC_{out} in Fig. 4.8a).

the microwave radiometer (see Fig. 4.16b). Moreover, anomalies in the cloud top properties and the LWP were observed during the periods with generating cells (Fig. 4.8d). Coinciding peaks in the anomaly signal were labeled as GC1 (16 UTC), GC2 (16:45 UTC) and GC3 (17:55 UTC). The Spearman's rank correlation coefficients of the anomalies ranged between 0.46 (for reflectivity and spectral width) and 0.73 (for reflectivity and LWP) significant at the 5 % level. Thus, given the significant correlation between updrafts, LWP and radar reflectivity within generating cells, it is likely that the updrafts acted as a major driver for the formation and maintenance of generating cells by providing a continuous source of liquid water and thereby enhancing ice nucleation and growth through immersion freezing, subsequent vapor deposition and riming. Indeed, the comparison of the Doppler spectra inside (GC_{in}) and outside (GC_{out}) of GC2 suggests that the generating cell contributed 10 dBZ to the radar reflectivity (see Appendix 4.B).

To further explore the microphysics within cloud top generating cells, the Doppler spectra along the 17 UTC fallstreak were investigated (Fig. 4.9). This approach allows to obtain a continuous picture of the evolution of the particle populations along the fallstreak and to draw conclusions regarding the microphysical processes active. Previous studies used the Doppler spectra information for the classification and characterization of ice particle shape and particle populations (e.g., Myagkov et al., 2016; Bühl et al., 2016). The vertical profile of the Doppler spectra shows a

broad particle distribution spanning from -5 m s^{-1} to 4 m s^{-1} between 3300 m and 5000 m height, indicative of a turbulent layer. This layer likely marked the extent of the generating cell, where ice crystals were produced and initial growth occurred. The Doppler spectra show a spectral bimodality below 3300 m (Fig. 4.9; i.e. presence of multiple particle populations with different fall speeds), which extends down to the surface. When analyzing the Doppler spectra of the full period with the peakTree technique (Radenz et al., 2019), multi-peaked situations become evident at the leading edges of the fallstreaks (Fig. 4.8c). The peakTree algorithm transforms each Doppler spectrum into a full binary tree structure, where the individual sub-peaks are represented as nodes (see Radenz et al., 2019). Thus, three nodes corresponds to two sub-peaks. For example, the Doppler spectrum in Figure 4.9b (red line) indicates the presence of two particle populations, a fast falling one (-2 m s^{-1}) and a slow falling one (-0.5 m s^{-1}). The LDR of the slower falling particle population was slightly higher (-25 dB; not shown) compared to the faster falling population (-28 dB; not shown). These LDR values are characteristic for oblate or plate-like particles (Myagkov et al., 2016). The observed Doppler spectra and the ice habits observed near cloud base (Fig. 4.13) suggest that the faster falling population represents heavily rimed ice particles/graupel, whereas the slower falling population was associated with stellar dendrites. This is also consistent with the observed temperature (dendrite regime; Magono and Lee, 1966; Bailey and Hallett, 2009) and the presence of supercooled liquid (riming) within the generating cells. It is likely that these two particle populations were already present above, but only separated below the turbulent layer due to the weaker updrafts and their difference in fall speed.

In the following, we will further investigate the origin of ice particles that formed within generating cells. Numerous studies have observed enhanced ice formation and growth in these updraft regions (Houze Jr et al., 1981; Hogan et al., 2002; Plummer et al., 2014; Ikeda et al., 2007; Crosier et al., 2014; Kumjian et al., 2014; Rauber et al., 2015). For example, Plummer et al. (2014) found that the ICNC was enhanced by a factor of 2 to 3 within the core region of generating cells compared to the region between the cells. While most of the studies agree that radiative cooling is a major driver for the formation and maintenance of cloud top generating cells, less research has focused on the reason for the enhanced ICNCs that were observed within these cells. Here we provide potential reasons from an INP-cloud perspective and propose possible mechanisms by considering the measured INP concentrations and cloud-base observations of the ICNC and ice particle size. INP concentrations were measured at the valley site Wolfgang (1630 m) and at the mountain-top station Weissfluhjoch (2700 m) (Fig. 4.10). The observed INP concentrations at a given temperature spanned over one order of magnitude. The INP concentration measured at Wolfgang was a factor of 3 - 10 higher compared to Weissfluhjoch, which was likely a consequence of the decoupled low-level flow (see Fig. 4.3a) and thus the sampling of different air masses. Based on the INP measurements at Weissfluhjoch, an INP concentration of 0.3 L^{-1} was extrapolated at cloud top (Fig. 4.10). It is important to note that the cloud top INP concentration was estimated from the Weissfluhjoch measurements in the morning (i.e., representative for pre-cloud INP concentrations), as no INP concentrations were measured at Weissfluhjoch during the passage of the cloud system. Additionally, cloud measurements were conducted by the HoloBalloon platform near cloud base. Since no in situ observations were available within

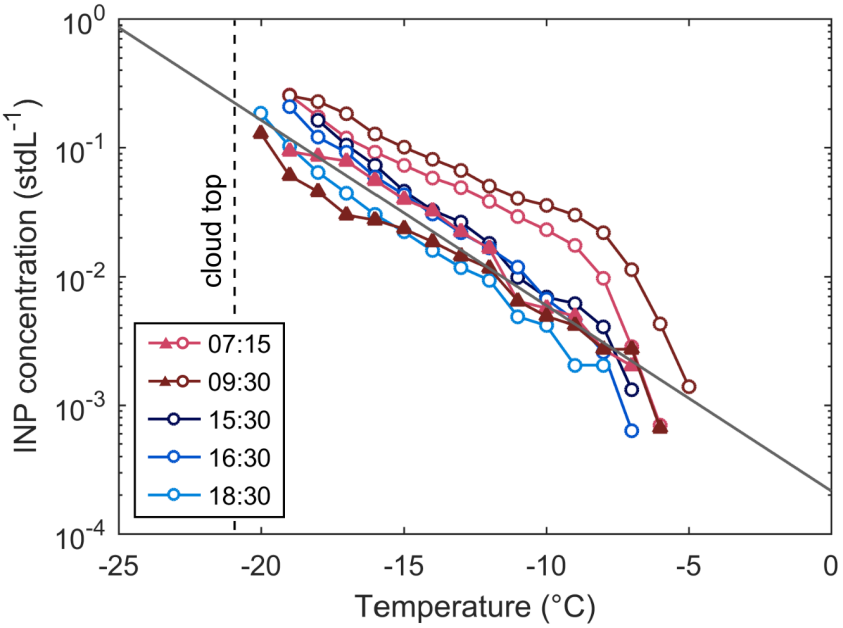

Figure 4.10: INP concentrations measured at Wolfgang (1630 m, circle) and Weissfluhjoch (2700 m, triangle) for different temperatures and times as indicated in the legend. The cloud top temperature of -21 °C is shown by the vertical dashed line. The dark gray line is a fit to the INP concentrations measured at Weissfluhjoch at temperatures between -9 °C and -17 °C (pre-cloud INP conditions).

the generating cells, assumptions regarding the upper-level cloud properties were required. We assumed that the largest ice particles (> 400 - 600 µm; derived from particle size distribution in Fig. 4.7b) formed near cloud top and grew to these large sizes while falling to the surface. This criterion is based on the assumption that the large ice particles did not sublimate completely prior to reaching the surface. The ICNC observed near cloud base was in the same order of magnitude as the ICNC retrieved from the remote sensing observations (red dots in Fig. 4.11) using the method described in Bühl et al. (2019). The comparison between the observed ICNC of large ice particles ($ICNC_{>500\,\mu m}$) and the INP concentration at cloud top shows a discrepancy between the observed INP concentration and ICNC during certain time periods (Fig. 4.11), suggesting that the ICNC cannot be solely explained by primary ice nucleation, but that other mechanisms were active.

Static instability driven by cloud top radiative cooling can produce strong updrafts (Fig. 4.8b) and lead to convective overshooting of cloud top generating cells (see red arrows in Fig. 4.8a). This convective overshooting can decrease the cloud top temperature and therefore increase the ICNC formed by primary ice nucleation. For example, the cloud top height during GC1 increased by 500 m from 4500 m to 5000 m. Considering the observed temperature profile in Figure 4.2b, the cloud top temperature decreased by 3.6 °C from -21 °C (at the average cloud top height) to -24.6 °C (at 5000 m) upon convective overshooting. Consequently, the INP concentration increased by a factor of 3.3 from 0.3 L^{-1} to 1 L^{-1} (Fig. 4.10) due to the colder cloud top temperature. The $ICNC_{>500\,\mu m}$ measured near cloud base lied below the extrapolated INP concentration at -25 °C before 18 UTC (Fig. 4.11), suggesting that the observed $ICNC_{>500\,\mu m}$ near cloud base can be solely explained by primary ice nucleation and convective overshooting. After 18 UTC, the $ICNC_{>500\,\mu m}$ measured near cloud base lied above the convective overshoot-

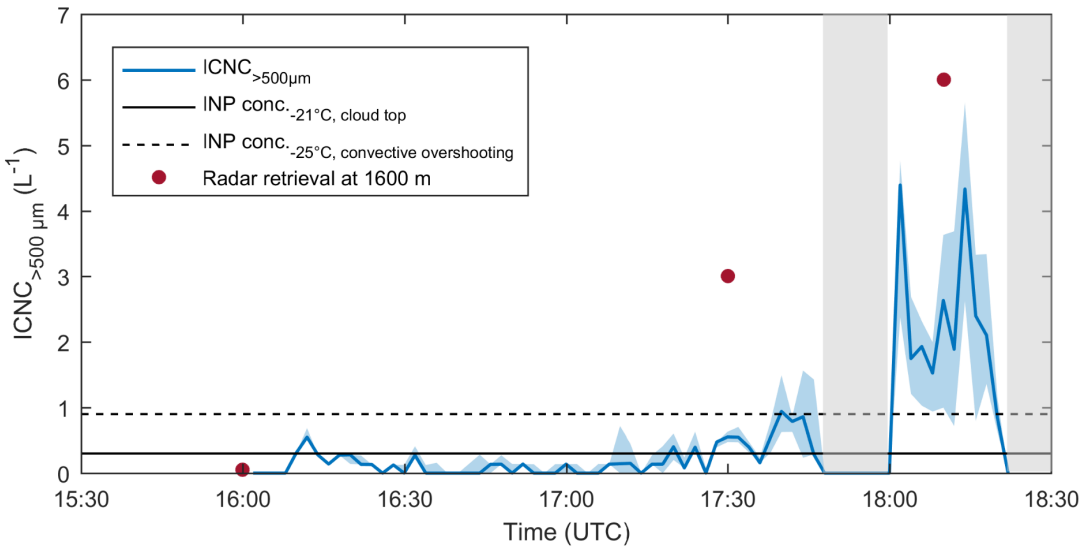

Figure 4.11: Timeseries of the ICNC of large ice particles ($>500\,\mu m$, $ICNC_{>500\,\mu m}$, blue line) measured near cloud base by the HoloBalloon platform. Ice particles larger than 500 µm in diameter were assumed to have formed near cloud top. The blue shaded area indicates ice particles larger than 400 µm (upper bound) and larger than 600 µm (lower bound). The INP concentrations extrapolated to -21 °C (cloud top, solid line) and to -25 °C (convective overshooting, dashed line) are indicated by the black horizontal lines. The ICNC estimated from the radar observations are shown by the red dots using the procedure described in Bühl et al. (2019) (see also Section 4.2). No microphysical measurements were available within the gray shaded areas.

ing line (Fig. 4.11), suggesting that other processes were occurring.

For example, the positive feedback between supercooled liquid water, radiative cooling and turbulence that has been observed near cloud tops (e.g., Morrison et al., 2012) might have contributed to enhanced ice formation. The presence of supercooled liquid can lead to strong longwave radiative cooling (e.g., Possner et al., 2017). This radiative cooling decreases the stability near cloud top, which causes turbulent motions, which in turn can produce further supercooled liquid water. The magnitude of the longwave radiative cooling strongly depends on the cloud phase, the liquid water content and particle size distribution, among other factors (e.g., Turner et al., 2018). Indeed, the LWP, as measured by the microwave radiometer, was enhanced within generating cells (see Fig. 4.8d) and thus likely increased the longwave radiative cooling at cloud top. The question is by how much the radiative cooling was enhanced within generating cells due the increased cloud liquid water compared to their surrounding regions. Previous studies observed longwave radiative cooling rates in the range of $1\text{-}5\,K\,h^{-1}$ near cloud top (e.g., Chen and Cotton, 1987; Pinto, 1998; Jiang et al., 2000; Rasmussen et al., 2002; Morrison et al., 2011; Morrison et al., 2012; Possner et al., 2017; Turner et al., 2018; Eirund et al., 2019). Additionally, Turner et al. (2018) computed radiative heating rate (RHR) profiles in the atmosphere as a function of cloud type and LWP by using an observational data set. According to Turner et al. (2018), an increase in the LWP from $50\,g\,m^{-2}$ to $150\,g\,m^{-2}$ (e.g., GC2 in Fig. 4.8) can cause an increase in the longwave radiative cooling rate from around $1.7\,K\,h^{-1}$ to $2.9\,K\,h^{-1}$ ($\Delta RHR = 1.2\,K\,h^{-1}$). This could potentially cool the cloud top temperature by 0.3 K, if a lifetime of around 15 min is assumed for cloud top generating cells (i.e., $1.2\,K\,h^{-1} \times 15\,min = 0.3\,K$),

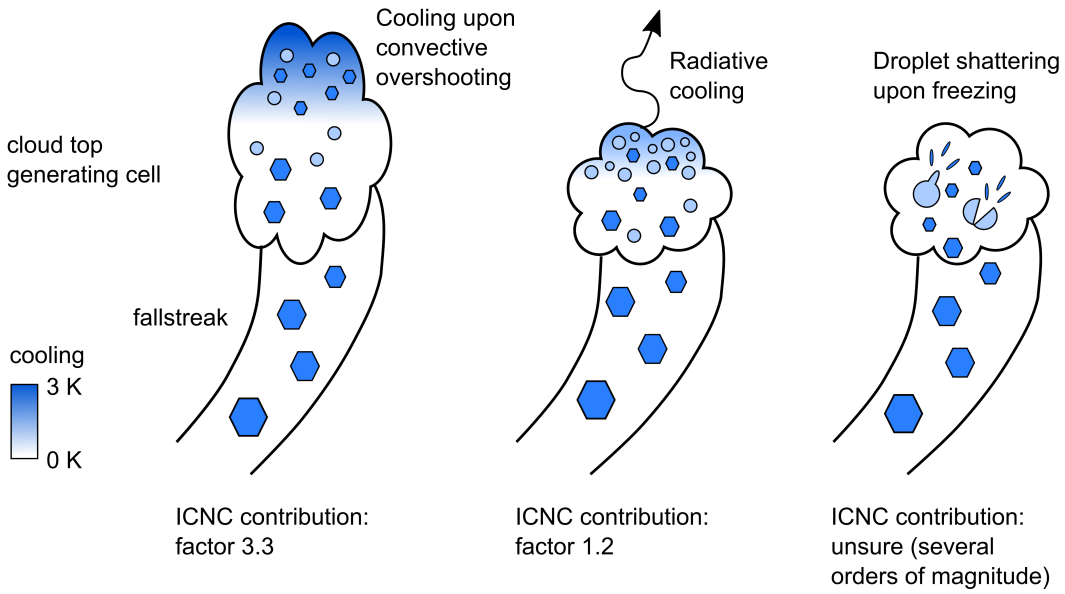

Figure 4.12: Potential mechanisms that could enhance the ICNC in cloud top generating cells: convective overshooting (left), radiative cooling (center) and droplet shattering upon freezing (right). Their potential contributions to the ICNC are estimated at the bottom based on the present case study (see text for more details).

and increase the INP concentration from $0.3\,\mathrm{L}^{-1}$ to $0.35\,\mathrm{L}^{-1}$ (factor 1.2, see Fig. 4.10). Thus, longwave radiative cooling only plays a minor role in enhancing primary ice nucleation. Nevertheless, longwave radiative cooling is of major importance for the production of radiatively driven turbulence near cloud top and thus for maintaining generating cells.

Other mechanisms must be active to explain the increased ICNCs after 18 UTC. For instance, the enhanced updrafts in generating cells allow all hydrometeors to grow to larger sizes. It is unlikely that the larger cloud droplet size would significantly increase primary ice nucleation by immersion freezing, which is the dominant ice nucleation mechanism in MPCs (e.g., Ansmann et al., 2008; De Boer et al., 2011; Westbrook and Illingworth, 2011), but it can play an important role for SIP. For example, the freezing of drizzle-sized droplets can release a large number of small secondary ice particles (e.g, Langham and Mason, 1958; Mason and Maybank, 1960; Lauber et al., 2018; Korolev and Leisner, 2020). This process is known as droplet shattering and has been observed to be strongly dependent on the cloud droplet size and to be potentially effective over a large temperature range (Lauber et al., 2018). Previous field studies have observed the presence of drizzle-sized droplets in the size range of 100 µm - 300 µm in regions of strong vertical updrafts (e.g, Hauf and Schröder, 2006; Ikeda et al., 2007). A single shattering event has the potential to produce hundreds of ice crystals. Thus, droplet shattering could increase the ICNC in generating cells by several orders of magnitude if supercooled drizzle drops are present in the updraft regions. As the discrepancy between the INP concentration at cloud top and $\mathrm{ICNC}_{>500\,\mu\mathrm{m}}$ was up to a factor 8 after 18 UTC, droplet shattering might have contributed to enhanced ice formation and growth and to the glaciation of the MPC. However, in situ observations within generating cells would be necessary to further investigate this hypothesis.

In summary, the increased ICNC in generating cells can be the result of different mechanisms or a combination of several mechanisms. Three possible mechanisms have been proposed in

this study and their potential contributions are summarized in Figure 4.12. Firstly, primary ice nucleation in generating cells can be increased due to convective overshooting or radiative cooling. The ICNC observed before 18 UTC can likely be explained by these two mechanisms, since the INP concentration and the $ICNC_{>500\,\mu m}$ measured near cloud base agreed within the same order of magnitude (Fig. 4.11). We found that the contribution from convective overshooting (factor 3.3) was larger than that of radiative cooling (factor 1.2) in the present study. On the other hand, the ICNC of large particles measured at the surface after 18 UTC exceeded the INP concentration by almost one order of magnitude, suggesting that SIP processes such as droplet shattering might be active within generating cells. However, more targeted studies are necessary to understand which mechanisms are responsible for enhanced ice formation and growth within generating cells. In particular, in situ measurements of the cloud properties within generating cells and their environmental conditions (e.g., temperature, updrafts, INP conditions) are of major importance to address these questions.

4.4.3 Secondary ice production processes in feeder cloud

Ice crystals that formed in the seeder region can grow by microphysical interactions with other cloud particles while falling through the cloud layer and thus influence the microphysics of the entire cloud. For example, if large ice particles fall through a supercooled liquid layer, they can initiate the glaciation of the cloud layer through the WBF process and/or grow by riming. Furthermore, the total number of nodes (Fig. 4.8c) shows multi-peaked situations below 3300 m, indicating the presence of multiple particle populations with different fall speed. This suggest that secondary ice particles might be produced in the feeder region of the cloud. In the following, we investigate the importance of ice growth and SIP in the feeder region by analyzing the phase-resolved cloud properties measured in situ with the HoloBalloon platform. In particular, the analysis of the ice crystal habit and size can provide important information about the formation and growth history of ice particles.

Figure 4.13 shows a representative set of ice particle images observed by HOLIMO as a function of height and time. It can be seen that ice crystal habits varied greatly during the passage of the cloud system. For example, the images indicate the presence of numerous columns between 17:00 UTC and 17:20 UTC at altitudes above 1780 m (yellow boxes), which are known to grow at temperatures between -3 °C and -10 °C (Magono and Lee, 1966; Bailey and Hallett, 2009). Furthermore, irregular shaped particles were abundant (green boxes), consistent with previous studies (e.g., Korolev et al., 1999; Stoelinga et al., 2007). A large fraction of graupel and rimed particles was observed between 17 UTC and 17:40 UTC (red boxes). After 18 UTC, the ice crystals became more aggregated (blue boxes) and less rimed (see also MASC data in Fig. 4.14d), suggesting a decrease in the amount of liquid water available for riming. Furthermore, small pristine ice crystals (plates and columns) were present over the entire period (see Fig. 4.15c and purple boxes in Fig. 4.13).

The large variability in ice crystal habit and size suggests that the ice crystals have formed and grown in different regions. As discussed in Section 4.4.2, it is likely that the heavily rimed ice particles and large dendrites (Fig. 4.13) were produced within the seeder region of the cloud and gained mass by riming and deposition while falling through the cloud. On the other hand,

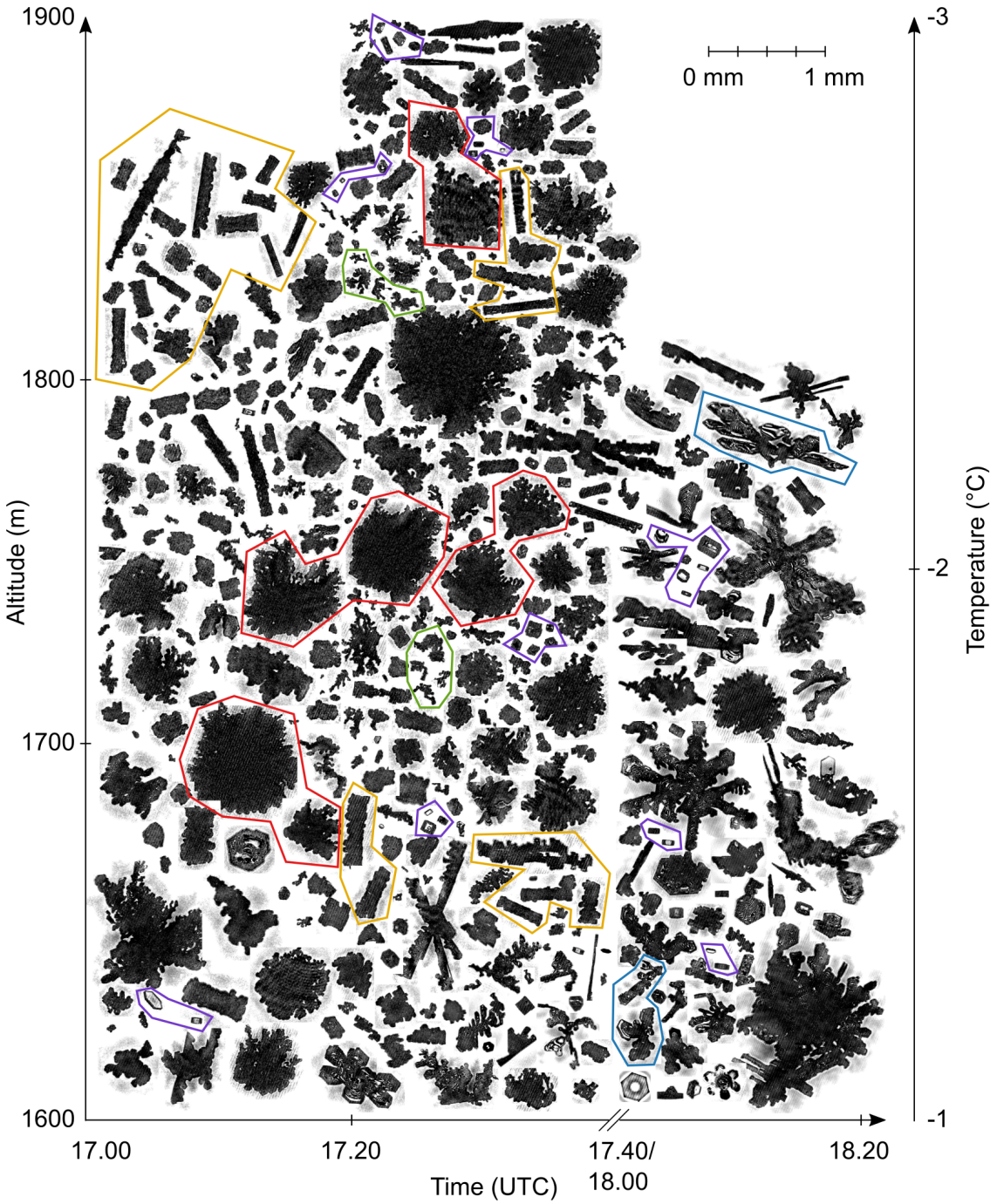

Figure 4.13: Example images of the ice crystals observed with HOLIMO as a function of height and time. The height-corresponding temperature is shown on the y-axis on the right side. The boxes indicate columns (yellow), pristine ice particles (purple), large rimed particles (red), irregular particles (green) and aggregates (blue).

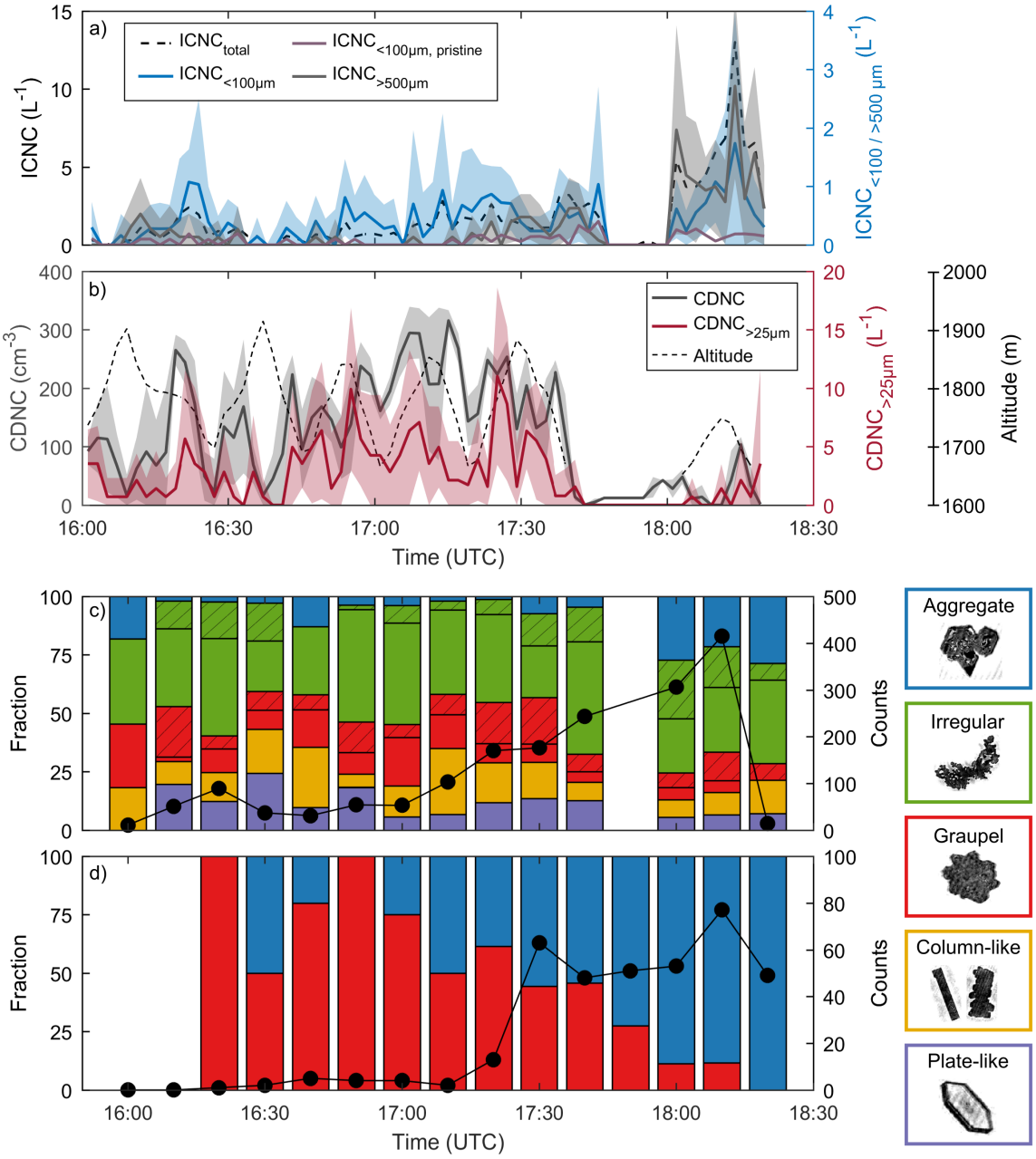

Figure 4.14: Timeseries of the ice (a) and liquid (b) cloud properties measured by the HoloBalloon platform. The shaded areas indicate the standard deviations. The dashed line in (b) shows the altitude of the balloon. The temporal evolution of the ice habit fraction is shown in (c, HOLIMO) and (d, MASC). The total counts during the 10 min-interval are indicated by the black dots. The ice particles observed with HOLIMO were classified into 5 categories: (1) plate-like, (2) column-like, (3) graupel (roundish particles), (4) irregular (unidentified habit) and (5) aggregates. Example ice particles are shown on the right. Only particles larger than 50 µm were considered in the habit analysis. Shaded areas in (c) indicate particles with a higher degree of riming. The hydrometeors observed by the MASC were classified into graupel and aggregates/snowflakes.

the small pristine ice crystals were likely formed within the feeder region of the cloud. Previous studies have found that small pristine ice crystals ($< 100\,\mu m$) were spatially correlated with their environment of origin (e.g., Korolev et al., 2020). For example, it is possible that the observed columns originated within the multi-peaked structures (Fig. 4.8c), as the temperature below 3000 m was in the temperature regime of columnar growth (Bailey and Hallett, 2009). Pristine plates likely grew in the lowest part of the cloud, where the prevailing temperature was above -3 °C. These small ice crystals ($< 100\,\mu m$) could have formed either by primary ice nucleation or by SIP processes within the feeder cloud and rapidly grown by diffusion to larger sizes (e.g., Korolev et al., 2020). The contribution of primary ice nucleation to the observed ICNC can be estimated from the measured INP concentration (Fig. 4.10), which was below the minimal detectable concentration ($6.3 \cdot 10^{-4}\,stdL^{-1}$; see Section 4.2) at a temperature of -3 °C. Thus, the minimal detectable concentration of $6.3 \cdot 10^{-4}\,stdL^{-1}$ represents an upper limit for the INP concentration within the feeder region. The ICNC of particles smaller than 100 µm in diameter observed in the feeder cloud (1 - $2\,L^{-1}$; Fig. 4.14a) exceeded the INP concentration by three orders of magnitude, suggesting that primary ice nucleation alone cannot explain the small ice crystals observed.

Secondary ice production processes are necessary to explain the observed ICNC in the low-level liquid layer. As the cloud droplets in the low-level feeder cloud were small ($< 50\,\mu m$ in diameter, Fig. 4.7a), droplet shattering was likely not the responsible mechanism. However, as the temperature at 1900 m was around -3 °C and large rimed particles (Fig. 4.14a) and cloud droplets larger than 25 µm in diameter (Fig. 4.14b) were observed in the low-level liquid layer, the Hallett-Mossop process may have been active (Hallett and Mossop, 1974; Mossop, 1978). Another mechanism that could have led to the production of secondary ice particles in the low-level feeder cloud is ice particle fragmentation upon ice-ice collisions (e.g., Vardiman, 1978; Takahashi et al., 1995). As the low-level liquid layer contained small pristine and large rimed ice particles (Fig. 4.13), which have different terminal fall velocities and therefore enhanced collision efficiencies, this suggests that collisional ice fragmentation may have been occurring. Indeed, the ice crystal images in Figure 4.13 indicate the presence of ice fragments. Therefore, based on the temporal evolution of the cloud properties (Fig. 4.14a, b), we suggest that ice particle fragmentation upon collision was the dominant SIP process after 18 UTC, since the CDNC and in particular the number of large cloud droplets decreased after 18 UTC (Fig. 4.14b). In contrast, the presence of large cloud droplets ($> 25\,\mu m$) before 18 UTC suggests that both the Hallett-Mossop process and collisional ice fragmentation contributed to the observed ICNC.

Previous studies have observed large discrepancies between the INP concentration and ICNC in the feeder region of clouds (e.g., Rogers and Vali, 1987; Lloyd et al., 2015; Beck et al., 2018; Lowenthal et al., 2019). These observations were frequently conducted at mountain-top research stations or near mountain slopes, where ICNCs of several hundreds to thousands per liter have been reported (e.g., Rogers and Vali, 1987; Lloyd et al., 2015; Lowenthal et al., 2019). These large ICNCs were attributed to the influence of surface processes such as blowing snow (Rogers and Vali, 1987, Geerts et al., 2015), hoar frost (Lloyd et al., 2015), riming on snow-covered surfaces (Rogers and Vali, 1987) or ice crystal enhancement through turbulence and convergence (Beck et al., 2018), whereas the contribution of SIP processes has been suggested to be minor or has

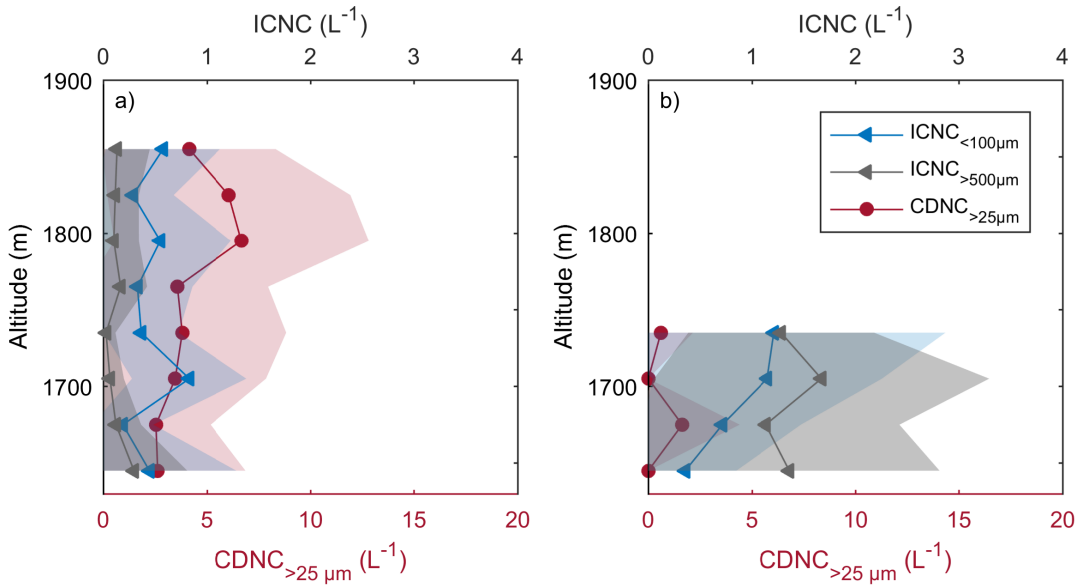

Figure 4.15: Mean vertical profiles of the liquid and ice properties measured between 16.30 - 17.30 UTC (a) and between 17:50 - 18:20 UTC (b) with the HoloBalloon platform. The shaded areas indicate the standard deviations.

been difficult to assess (Lloyd et al., 2015, Beck et al., 2018). By performing balloon-borne measurements in a mountain valley, we measured ICNC two order of magnitude lower than previous observations at mountain-tops (1 - 10 L^{-1} instead of 100 - 1000 L^{-1}) and thus were able to significantly reduce the impact of surface processes. Based on the observed INP concentration (Fig. 4.10) and ICNC (Fig. 4.14a), we suggest that SIP processes contributed up to 1-2 L^{-1} to the observed ICNC and thus accounted for up to 50 % of the total ICNC before 18 UTC. On the other hand, the increase in the ICNC from 3 L^{-1} up to 15 L^{-1} after 18 UTC (Fig. 4.14a) cannot be solely explained by SIP within the feeder cloud, since the observed increase was primarily due to large ice particles (> 300 µm, see Fig. 4.7b). This increase in ICNC can likely be attributed to a change in the microphysics within the seeder region, which initiated the glaciation of the MPC.

If only a small concentration of secondary ice particles is captured by updrafts or turbulence within the feeder region and lifted aloft, they can initiate further ice formation and growth at temperatures well above typical INP activation temperatures and have a significant impact on the development of the cloud (e.g., cloud properties, glaciation, lifetime). While the CDNC decreased above 1850 m, the vertical profiles of the ICNC showed no height dependence over the 200 m height interval (Fig. 4.15a). This suggests that SIP was active over the entire low-level liquid layer. However, due to the limited vertical extent of the profiles, we cannot make a final statement regarding the impact of SIP within the feeder region on the cloud microphysics aloft. Further observations in 'surface-decoupled' environments (i.e., reduced influence of surface processes) with a larger vertical extent are required to assess the role of SIP in feeder clouds. This is important, as it can lead to the formation of precipitation in clouds which otherwise may not have produced significant precipitation.

4.5 Conclusions

In this paper, we investigated the microphysical evolution of a mixed-phase cloud passing over the Swiss Alps using a multi-dimensional set of observations and instruments including (1) ground-based remote sensing, (2) in situ microphysical observations on a tethered balloon system, (3) INP measurements and (4) surface precipitation measurements. A particular emphasis was placed on studying the microphysics within cloud top generating cells and a persistent low-level feeder cloud from an aerosol-cloud-precipitation perspective. The key findings are summarized as follows:

- The microphysical structure of the MPC was observed with a vertically-pointing Ka-band polarimetric cloud radar and with a tethered balloon system. The phase transition from a liquid to an ice cloud was observed during the passage of the cloud system. It is likely that the Wegener-Bergeron-Findeisen process contributed to the glaciation of the MPC. Regarding the vertical cloud structure, generating cells with enhanced radar reflectivity were observed near the cloud top, which acted as a seeder region and produced fallstreaks of enhanced radar reflectivity. Furthermore, the decoupled boundary layer circulation in the lee of the mountain barrier produced local updrafts and turbulence, which led to the formation of a persistent low-level feeder cloud.

- The cloud radar and microwave radiometer observations suggest that ice formation and growth as well as liquid water production was enhanced within cloud top generating cells. While numerous studies have observed enhanced ICNCs within generating cells, uncertainties exist regarding their ice formation mechanism. Here we proposed different processes and discussed their potential contribution. Cooling associated with convective overshooting was suggested to increase the INP concentration by a factor of 3.3, whereas radiative cooling was estimated to increase the ICNC formed by primary ice nucleation only by a factor of 1.2. In addition, secondary ice production through droplet shattering was proposed to potentially increase the ICNC by several orders of magnitude and might have contributed to the glaciation of the MPC.

- The co-existence of small pristine ice crystals and large rimed ice particles was observed in the low-level feeder cloud, suggesting the occurrence of secondary ice production. By using a tethered balloon to observe the feeder cloud in the mountain valley, we were able to significantly reduce the influence of surface processes compared to previous observations at mountain tops and to investigate the contribution of secondary ice production in the feeder region of clouds. The ICNC of small ice crystals ($< 100\,\mu m$) measured near cloud base exceeded the INP concentration by three orders of magnitude. Conditions favorable for the Hallett-Mossop process and ice particle fragmentation upon ice-ice collisions were found. We suggest that secondary ice production in the feeder cloud increased the ICNC by a factor of 2.

Overall, this study observed the temporal and spatial evolution of the microphysics within the seeder and feeder region of a MPC passing over the Swiss Alps. We found that a significant increase in ice formation and growth within the seeder region can induce the glaciation of the

MPC. In addition, we found that secondary ice production mechanisms were active in the feeder cloud, which initiated ice formation at temperatures where no INP were detectable. This case study demonstrates that secondary ice production can occur in different cloud regions and have important implications for precipitation initiation and the lifetime of MPCs in general. Further studies are required to understand the role of secondary ice production both in the seeder and feeder regions of clouds. These studies should include vertically-resolved in situ observations of the microphysical properties, aerosol properties (e.g., INP) and environmental conditions (e.g., temperature, vertical updraft velocity) over the entire cloud depth and should be performed in a 'surface-decoupled' environment (i.e., reduced influence of surface processes).

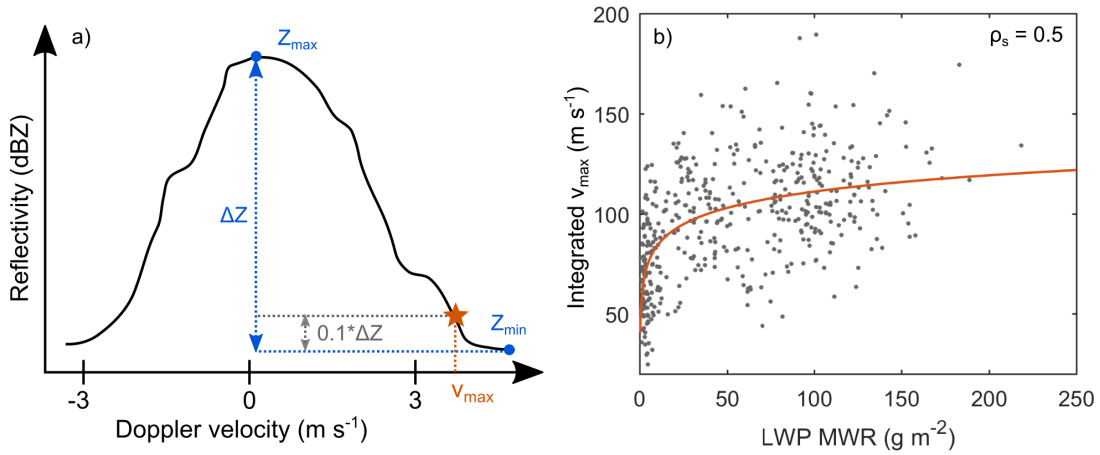

Figure 4.16: An example Doppler spectrum is shown in (a) to demonstrate the derivation of the maximum Doppler velocity v_{max} (orange star), where Z_{min} and Z_{max} are the minimum and maximum radar reflectivity (see text for more details). The relationship between the vertically-integrated v_{max} and the LWP measured by the microwave radiometer for the time period 15 - 18 UTC is shown in panel (b). The orange line is a logarithmic fit through the data points. ρ_s indicates the Spearman's rank correlation coefficient.

Appendix

4.A The use of the maximum Doppler velocity as a proxy for regions with updrafts and liquid water

In the framework of the present study, the maximum Doppler velocity was used as a proxy to identify regions with updrafts and liquid water. The maximum Doppler velocity v_{max} was derived from the Doppler spectra as shown in Figure 4.16a. In order to be more robust regarding the presence of extreme values, v_{max} was defined as follows:

$$v_{max} = \text{maximum Doppler velocity where } Z >= (Z_{min} + 0.1 \cdot (Z_{max} - Z_{min})) \tag{4.4}$$

where Z_{min} and Z_{max} are the minimum and maximum radar reflectivity. To validate whether v_{max} can also be used to identify regions with liquid water, it was compared to the LWP measured by the microwave radiometer. Since the LWP is integrated over the whole vertical column, the vertically-integrated v_{max} is shown in Figure 4.16b. A positive correlation was found between v_{max} and the LWP with a Spearman rank correlation coefficient of 0.5 significant at the 5% level. Based on this result, we assume that v_{max} can be used as a proxy for updraft regions and regions with liquid water.

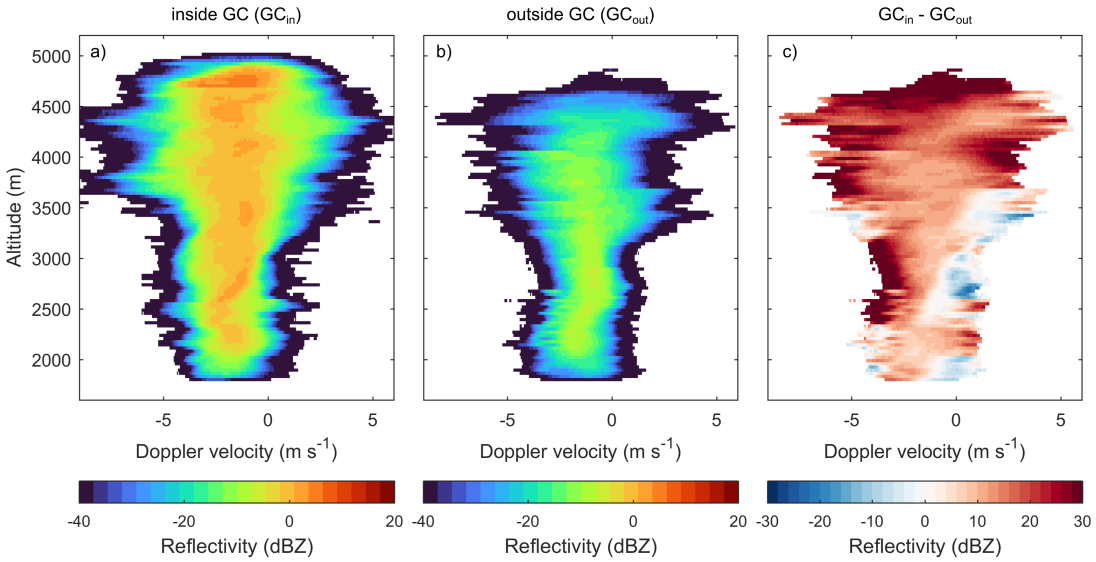

Figure 4.17: Vertical profile of the Doppler spectra inside (a; averaged over the region GC_{in}) and outside (b; averaged over the region GC_{out}) of the generating cell at 16:45 UTC (GC_{in} and GC_{out} are specified in Fig. 4.8a). The difference in the Doppler spectra between GC_{in} and GC_{out} is shown in panel (c).

4.B Cloud properties inside and outside of generating cells

To estimate the contribution of generating cells to the observed radar reflectivity signal, the cloud properties inside (a) and outside (b) of GC2 were compared (Fig. 4.17). The region inside the generating cell was determined by tracking the fallstreak of enhanced radar reflectivity, whereas the region outside of the generating cell was defined by the region between two adjacent cells that was characterized by a lower radar reflectivity (see Fig. 4.8a). The difference between the Doppler spectra inside and outside of generating cells (Fig. 4.17c) suggests that the generating cell at 16:45 UTC contributed 10 dBZ to the radar reflectivity and thus enhanced ice and precipitation formation. For a quantitative analysis, a large number of generating cells needs to be analyzed, which was beyond the scope of the present study.

Acknowledgments

The authors would like to thank the participants of the RACLETS campaign for their technical support and many fruitful discussions. In particular, we are thankful to Michael Lehning (WSL/SLF, EPFL) and his whole team for their substantial support for realizing the RACLETS campaign by providing local contacts and support in requesting the necessary permissions. We would like to thank Paul Fopp for providing his land for the RACLETS campaign. We would also like to thank Alexander Beck for helping with the organization of the field campaign. Moreover, the authors are thankful to Susanne Crewell (University of Cologne) and Bernhard Pospichal (University of Cologne) for their help in interpreting the microwave radiometer data. We would also like to acknowledge Benjamin Walter (SLF) for providing data of the snowdrift station

located at Gotschnagrat. We thank the Swiss Federal Office of Meteorology and Climatology MeteoSwiss for providing the meteorological measurements, radiosonde data from Payerne, MASC observations and access to the COSMO1 and weather radar data. Furthermore, we would also like to thank Eberhard Bodenschatz (MPI Goettingen) for his technical support during the development of the HoloBalloon platform. We would like to thank the Federal Office of Civil Aviation, particularly Judith Baumann and Jeroen Kroese, for their pragmatic approach in obtaining the flight permit. FR, JH, JW, AL, JP and UL acknowledge funding from the Swiss National Science Foundation (SNSF) grant number 200021_175824. RD would like to acknowledge funding from the European Research Council (ERC) through Grant StG 758005. CM acknowledges funding from the SNSF through grant number 200021_169620.

Chapter 5

Conclusion and outlook

5.1 Summary of results

In this thesis, we investigated the microphysics and dynamics of MPCs using balloon-borne in situ observations and ground-based remote sensing instrumentation, with a particular focus on orographic clouds in the Swiss Alps. A case study approach was chosen to study unique microphysical features and the complex interplay between orography, dynamics and microphysics on a process level. The objectives of the thesis were to develop a new measurement platform for observations of boundary layer clouds in complex terrain and to improve the process understanding of orographic MPCs and precipitation. The following section summarizes the main findings and conclusions of this thesis.

5.1.1 HoloBalloon - a cloud measurement platform for boundary layer clouds

In the framework of this thesis, a new measurement platform on a tethered balloon system (HoloBalloon) was developed to study boundary layer clouds in complex terrain or densely-populated areas. The major component of the measurement platform is the HOLographic Imager for Microscopic Objects 3B (HOLIMO 3B), which uses digital in-line holography to image an ensemble of cloud particles in a three-dimensional sample volume and to obtain information about the phase-resolved particle size distribution and particle shape. As the previous version (HOLIMO 3G; Beck et al., 2017), HOLIMO 3B has an open-path configuration and additionally, has an improved optical system (larger detection volume, an improved lens system, 355 nm laser) and an adapted instrument tip design suitable for the application on a tethered balloon system. Holographic imagers benefit from (1) a well-defined sample volume independent of particle size and air speed, (2) their outstanding feature to observe the spatial distribution of an ensemble of cloud particles and (3) their ability to measure particles over a wide size range (6 µm - 2 mm). The combination of a holographic imager and a balloon-borne measurement platform provides unique observations of cloud structures from the kilometer down to the millimeter scale. The measurement platform is also equipped with auxiliary instruments (e.g., temperature, pressure and relative humidity sensor, 3D ultrasonic anemometer), which allows for meteorological parameters to be observed.

The HoloBalloon platform was successfully deployed in different environments (e.g., stratus

clouds, orographic clouds) and atmospheric conditions (e.g., temperatures down to -8 °C, wind speeds up to 15 $\mathrm{m\,s^{-1}}$). The platform was able to accurately observe phase-resolved cloud properties and to capture small-scale variations in the particle number concentration, particle size and particle shape on a meter scale.

5.1.2 Orographic effects on precipitating clouds

Orography can trigger the formation of orographic clouds or influence the structure of incoming cloud systems and thereby enhance precipitation and influence its spatial distribution (e.g., Roe, 2005; Houze Jr, 2012; Smith, 2019). The amount and distribution of orographic precipitation over and near complex terrain is determined by different factors such as the height and shape of the mountain, the dynamical response of the flow encountering a mountain barrier, the microphysics of particle growth and the thermodynamics of the atmosphere (e.g., Houze Jr, 2012).
In this thesis, the interplay between orography, dynamics, microphysics and precipitation was studied on the basis of several case studies. For example, in Chapter 3, we investigated the role of low-level blocking and shear-induced turbulence on the cloud microphysics and precipitation formation in an inner-Alpine valley. The boundary layer was characterized by blocked low-level flow. At the interface between the blocked layer and the stronger cross-barrier flow aloft, a strong shear layer ($> 10\,\mathrm{m\,s^{-1}\,km^{-1}}$) embedded with turbulent cells was observed. The cloud radar indicated changes in the microphysical cloud properties within the turbulent shear layer including increased radar reflectivity (i.e., enhanced ice growth) and enhanced linear depolarization ratio (i.e., changes in particle shape). Previous studies suggested that theses turbulent cells can enhance ice growth and precipitation through riming and aggregation (e.g., Houze Jr and Medina, 2005; Houze Jr and Medina, 2005; Geerts et al., 2011; Aikins et al., 2016). Furthermore, we suggest that ice fragmentation upon collision within the turbulent shear layer might have contributed to secondary ice production. These secondary ice particles have the potential to recirculate in the shear layer and influence the cloud microphysics aloft (e.g. Grazioli et al., 2015). However, this process could not be directly measured in this study due to limitations in the flight level.
In the observed case study (Chapter 3), the amount of precipitation in the inner-Alpine valley was coupled to the strength of the low-level blocking and the cross-barrier flow, as the interplay between these dynamical effects determined the height of the shear layer and cloud base. The shear layer was observed to lower when stronger cross-barrier flow moved over the upstream mountain barrier and the low-level blocking weakened. As a consequence of the lower shear layer altitude and cloud base, hydrometeors could reach the surface as precipitation prior to complete sublimation.
Additionally, a low-level liquid cloud was observed by the HoloBalloon platform when the low-level flow was blocked (Chapter 3). This low-level cloud dissipated when the low-level flow turned from a blocked to an unblocked state. Our observations suggest that the low-level blocking (due to the downstream mountain barrier) caused the low-level flow to ascend the leeward slope of the local topography in the valley and thus produced a low-level feeder cloud. Similarly, a persistent low-level feeder cloud was observed in Chapter 4, when the low-level flow was forced to ascend over the local topography. This shallow low-level cloud was assumed to not have generated sig-

nificant precipitation by itself, because of the relatively warm temperatures (-3 °C), which were limiting ice formation through primary ice nucleation, and due to the limited time available to form precipitation-sized particles through collision-coalescence. However, this shallow low-level liquid cloud was found to "feed" on precipitation particles that formed at higher altitudes and thus to enhance precipitation by riming and depositional growth. Thus, we propose that local flow effects such as low-level blocking can induce the formation of feeder clouds in mountain valleys and on the leeward slope of foothills upstream of the main mountain barrier, where they can enhance orographic precipitation through the seeder-feeder mechanism.

5.1.3 The origins of ice crystals in orographic MPCs

The ice phase plays a crucial role for precipitation formation in the mid-latitudes, since more than 90% of the precipitation originates in ice containing clouds (e.g., Mülmenstädt et al., 2015; Field and Heymsfield, 2015). The WBF process and riming can increase the growth of ice particles at the expense of the liquid phase and thereby favor the glaciation of MPCs. Nevertheless, persistent MPCs have been frequently observed in mountain regions (e.g., Borys et al., 2003; Geerts et al., 2010; Lowenthal et al., 2011; Lloyd et al., 2015; Lohmann et al., 2016a; Beck, 2017), where the local topography produces sufficiently large updrafts and turbulence to provide a continuous source of condensate. It is important to understand the delicate balance between the production and consumption of supercooled liquid water, because it determines precipitation formation and the lifetime of MPCs.

In Chapter 4, we studied the role of cloud top generating cells and of a low-level feeder cloud for ice formation, ice growth and precipitation on the basis of a case study. The cloud radar observations showed fallstreaks of enhanced radar reflectivity near cloud top, indicating that the bulk of precipitation originated at the cloud top in so-called generating cells. While most of the previous studies agree that cloud top generating cells are governed by radiative cooling and are important for ice and precipitation formation (e.g., Houze Jr et al., 1981; Hogan et al., 2002; Ikeda et al., 2007; Crosier et al., 2014; Plummer et al., 2015; Rauber et al., 2015), uncertainties remain regarding the underlying microphysical processes. In Chapter 4, we proposed different mechanisms that potentially increase ice formation and growth within generating cells by analyzing the INP concentrations and ICNC measured near cloud base. We suggest that convective overshooting and enhanced radiative cooling due to higher LWP can increase primary ice nucleation by a factor of 3.3 and 1.2, respectively. In cases where the ICNC exceeds the INP concentration by several orders of magnitude, secondary ice production processes might be active within generating cells (e.g., droplet shattering). We found that enhance ice formation and growth within the seeder region can initiate the full glaciation of the cloud. More research is required to understand the dynamics and microphysics of generating cells. Future studies should include in situ observations of cloud properties, aerosol properties (e.g., INP) and environmental conditions (e.g., temperature, updraft velocity) over the entire cloud depth.

Furthermore, a persistent low-level feeder cloud was observed, which was sustained by updrafts within the boundary layer circulation. The ICNC within the low-level cloud was three orders of magnitude higher than the observed INP concentration. Indeed, observations from the HoloBalloon platform indicated the coexistence of small pristine ice crystals and large rimed ice

particles, suggesting that secondary ice production processes were active in the low-level feeder cloud. Conditions favorable for the Hallett-Mossop process and collisional ice fragmentation were found, which were suggested to contribute 50% of the observed ICNC. While previous observations at mountain-top stations had limitations in investigating the role of secondary ice production in feeder clouds, we were able to significantly reduce the influence of surface processes by using a tethered balloon. If only a small concentration of secondary ice particles is captured by updraft within the feeder region and lifted aloft, they can initiate further ice formation and growth and thus have a significant impact on the further evolution of the cloud.

5.2 Outlook and proposed future research

5.2.1 Technical improvements of HoloBalloon

Based on the experiences gained during the first two field campaigns, technical changes have been made to the HoloBalloon platform. Firstly, due to the optical resolution limit of HOLIMO 3B (6 µm), HOLIMO 3B was not able to detect the entire cloud droplet size distribution during the first field campaign in stratus clouds over the Swiss Plateau. This can introduce a bias and lead to an underestimation of CDNC, especially close to the cloud base, in entrainment regions or in clouds with small cloud droplets. To overcome this issue, the HoloBalloon platform was equipped with an optical particle counter (OPC) during the RACLETS campaign, which was capable of measuring even the smallest cloud particles. Parallel measurements of the cloud properties with HOLIMO 3B and an OPC allowed for the entire cloud droplet spectrum to be covered and thus to accurately capture cloud activation and entrainment.
Secondly, it is recommended to install the instrument package 20 - 30 m below the balloon in future field campaigns in order to minimize potential influences of the balloon on the microphysical and turbulence measurements. More specifically, the mounting of HOLIMO 3B on the keel could have influenced the observation of large ice particles due to shielding effects of the balloon, which may have led to an underestimation of the ICNC of large ice particles and therefore of the IWC. This effect is expected to be strongest at low wind speed, when the balloon ascends almost vertically. Computational fluid dynamics simulations at different wind conditions could help to assess the influence of the balloon on the air flow and to determine the minimum distance required between the balloon and the instrument package to ensure accurate measurements of cloud properties and turbulence. In addition, the hanging mount facilitates the ground handling in difficult wind conditions, as the instrument package can be retrieved while the balloon is still flying. The feasibility of a hanging mount was already successfully tested and applied in the field in the fall of 2019.
Lastly, future campaigns should measure or collect INPs on the HoloBalloon platform. That way INPs are sampled directly in the cloud rather than relying on the ground-based measurements, which may not be representative of the INP concentrations aloft. In Chapter 4, we were limited to ground-based INP measurements and had to assume that the observed INP concentrations at the surface were representative of the INP concentration inside the cloud. This assumption might not always be justified, especially when the low-level flow is decoupled from the large-scale flow. Aerosol particles can for example be collected by a miniaturized electrostatic

precipitator onto silicon wafers (Schrod et al., 2017). Another possibility is to use a miniaturized cloud water sampler for collection of cloud water, which was already successfully deployed on a tethered balloon system during the Microbiology-Ocean-Cloud-Coupling in the High Arctic (MOCCHA) campaign (Zinke et al., 2020). The collected aerosol particles and cloud water can be analyzed in the laboratory regarding their chemical composition and ice nucleating activity by using the drop-freezing instrument DRINCZ (David et al., 2019a). This further development of the HoloBalloon platform could be helpful to study the origins of ice crystals in clouds and improve our understanding of aerosol-cloud interactions.

5.2.2 Future field campaigns

Parallel measurements of in situ and remote sensing instruments are highly recommended for future field campaigns. While the HoloBalloon platform can provide high-resolution measurement of cloud properties, it has limitations regarding the temporal and spatial coverage. As a consequence, only limited understanding about the microphysics of stratus clouds was obtained during the first field campaign over the Swiss Plateau (Chapter 2). On the other hand, the extensive set of instruments during the RACLETS campaign enabled a thorough characterization of the cloud structure and a more comprehensive understanding of the observed cloud systems. Remote sensing instrumentation are particularly important for continuous measurements of the cloud microphysics. Furthermore, observations of the three-dimensional wind field are of great importance in complex terrain. A further benefit of parallel in situ and remote sensing measurements, is the validation of remote sensing retrievals with the help of in situ observations (e.g., Protat et al., 2007; Matrosov et al., 2012; Deng et al., 2013).
The deployment of the HoloBalloon platform was restricted to the lowest 200 - 400 m of the boundary layer during the RACLETS campaign, because of limited lifting capacity and turbulent wind conditions in the inner-Alpine valley. For future field campaigns in mountain regions, the HoloBalloon platform should be launched from locations below 1200 m to ensure higher lifting capacity. Moreover, locations on the windward side of the mountain barrier are preferred in order to minimize turbulent conditions and downward wind motions, facilitating easier handling of the tethered balloon system. Nevertheless, the range of the HoloBalloon platform in mountain regions will be limited to the lower part of the boundary layer, whereas the upper part of the cloud requires the use of auxiliary instruments and measurement platforms (e.g., aircraft, remote sensing instrumentation). Therefore, it should be considered to deploy the HoloBalloon platform in low-level clouds and at locations close to sea level to enable the penetration of the entire cloud layer. For example, the HoloBalloon platform can be used to improve our understanding of the development and dissipation of fog and low stratus clouds over the Swiss Plateau, which represents a major challenge for current numerical weather prediction models. Due to their relatively stable conditions, stratus clouds can also be exploited as a natural laboratory to study aerosol-cloud interactions by injecting INPs into the cloud and by observing the consequential changes in the cloud properties with the HoloBalloon platform and ground-based remote sensing instrumentation. Furthermore, the HoloBalloon platform can be deployed in Arctic MPCs, where the clouds are often so shallow that HOLIMO can observe the phase-resolved cloud properties within the supercooled liquid layer near cloud top. This would help to

improve our understanding about the underlying physical processes and feedback mechanisms operating in Arctic MPCs.

5.2.3 Scale-dependent phase partitioning in MPCs

Observations of the partitioning of the liquid and ice phase can help to improve our understanding of ice initiation and cloud glaciation and thus the life cycle of MPCs. The phase partitioning is strongly dependent on the spatial averaging scale. The HoloBalloon platform benefits from its ability to observe cloud properties over a wide range of scales, which allows investigating the spatial distribution of the liquid and ice phase from the meter down to the millimeter scale.
The holographic imager HOLIMO 3B has a well-defined sample volume, which is defined by the cross-sectional area of the camera and the distance between the instrument towers (i.e., $15 \times 15 \times 200\,\mathrm{mm}$). The sample volume rate can vary between $45\,\mathrm{cm^{-3}\,s^{-1}}$ (for 1 fps) and $3600\,\mathrm{cm^{-3}\,s^{-1}}$ (for 80 fps) depending on the frame rate. The choice of the frame rate is a trade-off between high temporal and spatial resolution and long time series and depends on the measurement strategy, which is constrained by the research questions. So far, we aimed to achieve a balance between high spatial resolution and high temporal coverage by applying a frame rate of 10 fps. This allows the investigation of phase partitioning on a meter scale. Future field campaigns in MPCs could acquire holograms with a higher frame rate of 80 fps. This measurement strategy would allow to investigate the horizontal and vertical distribution of the liquid and ice phase on an even smaller scale.
For example, the spatial inhomogeneity of MPCs can have important implications for the glaciation time of MPCs. If the liquid and ice phase are spatially separated in different clusters, the efficiency of the WBF is reduced because regions with pure liquid are not exposed to regions with ice particles. This results in an extended glaciation time of the MPC and thus in a longer lifetime. The phase partitioning is particularly important near the cloud top, since the coldest temperatures are usually present there, which determine the amount of ice produced. Furthermore, the horizontal distribution of the liquid and ice phase near cloud top has important implications for radiative effects.
The high acquisition rate of HOLIMO 3B allows the investigation of the variability of ICNC on even smaller scales. This, in combination with the ability of HOLIMO 3B to observe particles over a wide size range, i.e. from cloud droplets (6 µm) to small ice crystals at the early stage of formation (25 µm - 100 µm) to large rimed ice particles (500 µm - 2 mm), enables to detect regions with a sudden increase in ICNC and thus to identify conditions favorable for secondary ice production (e.g., temperature, cloud droplet size distribution, vertical updrafts). This information can help to improve our physical understanding of the different secondary ice production mechanisms (Field et al., 2017), including the environment and scales that they occur at.
In environmental conditions with low wind speed, the high acquisition rate might enable creating a large coherent cloud volume. An overlap of individual holograms can be achieved with a frame rate of 80 fps at wind speeds below $1.2\,\mathrm{m\,s^{-1}}$ (i.e., $15\,\mathrm{mm} \times 80\,\mathrm{fps}$). A large coherent cloud volume can be favorable to study the spatial distribution of ice particles in the cloud. Since ice particles are less abundant in the atmosphere than cloud droplets, only a few ice crystals are usually observed in a single hologram. This makes it challenging to study the spatial distri-

bution of ice particles on a single hologram basis, as conventional methods such as the nearest neighbor analysis (e.g., Beck et al., 2017) or the three-dimensional radial distribution function (e.g., Larsen and Shaw, 2018) cannot be used. However, these numerical methods might also be applicable for ice particles if a large coherent volume can be created from several connected holograms. This would allow investigating the spatial distribution of ice particles on a sub-meter scale, which can further improve the understanding of cloud glaciation and secondary ice production.

5.2.4 Entrainment and mixing at cloud edges

The spatial distribution of cloud droplets can be analyzed on a single-hologram basis by making use of the unique feature of holographic cloud imagers to observe the spatial distribution of an ensemble of cloud particles (e.g., Beals et al. (2015); Beck et al., 2017; Glienke et al., 2020). This unique feature allows investigating small-scale cloud processes or interactions between cloud particles. For example, entrainment and mixing of sub-saturated air from the surrounding can influence the cloud droplet number size distribution through complete evaporation of a fraction of cloud droplets (i.e., inhomogeneous mixing, Pinsky et al., 2016a) or through partial evaporation of all cloud droplets (i.e., homogeneous mixing, Pinsky et al., 2016b). Both types of mixing change the shape of the cloud droplet size distribution and thus have important implications for cloud radiative effects and precipitation initiation (Korolev et al., 2016). The effects of entrainment and mixing are further complicated in MPCs due to the presence of ice particles, which add another layer of complexity (Korolev et al., 2017). The HoloBalloon platform can help to improve our understanding of entrainment and turbulent mixing at cloud top or cloud edges in MPCs by analyzing the spatial distribution of cloud particles and the spatial variability of the phase-resolved cloud particle size distribution.
Additionally, in an environment with low wind speed ($< 1.2\,\mathrm{m\,s^{-1}}$; e.g., in ground fog and low stratus clouds), three-dimensional tracking of an ensemble of cloud particles might be possible, if the same cloud particles are illuminated multiple times. Three-dimensional particle tracking can be used to study turbulence, entrainment and mixing at cloud edges. A single-camera, in-line holography tracking method was proposed by Lu et al. (2008), who obtained measurements of the three-dimensional Lagrangian properties of particles in a turbulence chamber. However, it is questionable whether a frame rate of 80 fps is sufficient for three-dimensional particle tracking in a natural cloud environment.

5.2.5 High resolution modeling of orographic MPCs

Precipitation forecasts in complex terrain remain challenging in terms of amount, timing and location. The observations obtained within the framework of this thesis showed that a complex interplay between orography, dynamics and microphysics can influence precipitation formation in complex terrain. Microphysical signatures on the scales of several tens of meters to a few kilometers were found to enhance precipitation. For example, cloud top generating cells were identified to enhance ice formation and growth and to act as a seeder region. These generating cells are usually 1 - 2 km deep and 0.5 - 2 km wide (e.g., Rosenow et al., 2014; Kumjian et al., 2014). Additionally, the decoupled low-level flow on the lee side of the mountain barrier was

found to induce the formation of a shallow low-level feeder cloud above a small-scale topographic feature, which enhanced precipitation through the seeder-feeder mechanism. High resolution models are required to capture these small-scale microphysical signatures and to resolve the influence of topography on the cloud structure, dynamics and microphysics, which ultimately contribute to improved precipitation forecasts over complex terrain.

Furthermore, the observations obtained within this thesis and the RACLETS campaign can help to improve the process understanding of MPCs and the pathways of precipitation formation, since an extensive set of observations was combined. Parallel observations of aerosol, cloud and precipitation allow studying the entire life cycle of ice crystals, from ice initiation through primary ice nucleation on INPs, to ice multiplication through secondary ice production processes, to ice growth through riming, aggregation and the WBF process to precipitation-sized particles, and finally to the glaciation of MPCs. An accurate representation and understanding of MPCs and in particular of the microphysical pathways of precipitation formation can improve the reliability of regional precipitation forecasts.

List of symbols and abbreviations

λ	wavelength, page 10
ϕ_p	phase shift of the received signal, page 12
C_R	radar constant, page 10
F_{impinger}	flow rate of impinger, page 62
Fr	Froude number, page 54
G	gain of the antenna, page 10
h	height, page 54
K^2	complex index of refraction, page 10
P_r	power received by the antenna, page 10
P_t	transmitted power by the antenna, page 10
p_{ambient}	ambient pressure, page 62
p_{ref}	reference pressure, page 62
s	shear, page 64
T_{ambient}	ambient temperature, page 62
T_{ref}	reference temperature, page 62
t_{sample}	sampling time, page 62
U	wind speed perpendicular to the mountain barrier, page 54
V_a	volume of an individual aliquot, page 62
V_R	radial velocity, page 12
V_{liquid}	end volume of the liquid, page 62
v_{max}	maximum Doppler velocity, page 80
w_{l_ad}	adiabatic liquid water content, page 26
w_s	saturation mixing ratio, page 26
Z	radar reflecitivity, page 10
Z_e	equivalent reflectivity factor, page 10
Z_{max}	maximum radar reflectivity, page 80
Z_{min}	minimum radar reflectivity, page 80
2D-C	2D Cloud probe, page 9
2D-P	2D Precipitation probe, page 9
2D-S	2D Stereo probe, page 9
APS	Aerodynamic Particle Sizer, page 22
CCN	cloud condensation nucleus, page 3
CDNC	cloud droplet number concentration, page 25
CDNC$^{\text{a}}$	anomaly of the cloud droplet number concentration, page 27

CFAD	Contour frequency by altitude diagram, page 44
CIP	cloud imaging probe, page 9
CPI	cloud particle imager, page 9
$D_{res,lens}$	optical resolution of a lens system, page 21
$D_{res,obs}$	measured optical resolution, page 21
$D_{res,pixel}$	optical resolution of the pixel pitch, page 21
$D_{res,rec}$	optical resolution of the reconstruction, page 21
DAV	Davos, page 38
DRINCZ	DRoplet Ice Nuclei Counter Zurich, page 62
fps	frames per second, page 20
GC	generating cell, page 69
GOT	Gotschnagrat, page 38
HOLIMO	HOLographic Imager for Microscopic Objects, page 13
HOLIMO 3B	The newly developed HOLIMO for the tethered balloon system HoloBalloon, page 18
HOLIMO 3G	Third version of a HOLIMO with an open path configuration. HOLIMO 3G is deployed on a cable car, page 20
HVPS	high-volume precipitation spectrometer, page 9
ICNC	ice crystal number concentration, page 4
INP	ice nucleating particle, page 3
IWC	ice water content, page 64
IWV	integrated water vapor content, page 37
LDR	linear depolarization ratio, page 11
Lidar	Light detection and Ranging, page 12
LINDA	LED-based Ice Nucleation Detection Apparatus, page 62
LWC	liquid water content, page 24
LWP	liquid water path, page 37
MAP	Mesoscale Alpine Programm, which took place in the Alpine region, page 35
MASC	Multi-Angle Snowflake Camera, page 37
MOCCHA	Microbiology-Ocean-Cloud-Coupling in the High Arctic campaign, page 86
MPC	mixed-phase cloud, page 3
MW	Mischwolken, page v
NWP	numerical weather prediction models, page 16
PBL	planetary boundary layer, page 16
PIP	precipitation imaging probe, page 9
RACLETS	Role of Aerosols and CLouds Enhanced by Topography on Snow campaign, which took place in the region around Davos in the Swiss Alps during February and March 2019, page 14
Radar	Radar detection and ranging, page 10
RHI	Range Height Indicator scans, page 37
RHR	radiative heating rate, page 73

SIP	secondary ice production, page 59
TBS	tethered balloon system, page 16
TKE	turbulent kinetic energy, page 46
TWC	total water content, page 64
VOAG	Vibrating Orifice Aerosol Generator, page 22
WBF	Wegener-Bergeron-Findeisen process, page 4
WFJ	Weissfluhjoch, page 38

List of Figures

List of Tables

Bibliography

Aikins, J., Friedrich, K., Geerts, B., and Pokharel, B.: Role of a cross-barrier jet and turbulence on winter orographic snowfall, Monthly Weather Review, 144, 3277–3300, 2016.

Amsler, P., Stetzer, O., Schnaiter, M., Hesse, E., Benz, S., Moehler, O., and Lohmann, U.: Ice crystal habits from cloud chamber studies obtained by in-line holographic microscopy related to depolarization measurements, Applied optics, 48, 5811–5822, 2009.

Ansmann, A., Tesche, M., Althausen, D., Müller, D., Seifert, P., Freudenthaler, V., Heese, B., Wiegner, M., Pisani, G., Knippertz, P., et al.: Influence of Saharan dust on cloud glaciation in southern Morocco during the Saharan Mineral Dust Experiment, Journal of Geophysical Research: Atmospheres, 113, 2008.

Bacon, N. J., Swanson, B. D., Baker, M. B., and Davis, E. J.: Breakup of levitated frost particles, Journal of Geophysical Research: Atmospheres, 103, 13 763–13 775, 1998.

Bader, M. and Roach, W.: Orographic rainfall in warm sectors of depressions, Quarterly Journal of the Royal Meteorological Society, 103, 269–280, 1977.

Bailey, M. P. and Hallett, J.: A comprehensive habit diagram for atmospheric ice crystals: Confirmation from the laboratory, AIRS II, and other field studies, Journal of the Atmospheric Sciences, 66, 2888–2899, 2009.

Baker, B. A.: Turbulent entrainment and mixing in clouds: A new observational approach, Journal of the atmospheric sciences, 49, 387–404, 1992.

Bartok, J., Bott, A., and Gera, M.: Fog prediction for road traffic safety in a coastal desert region, Boundary-layer meteorology, 145, 485–506, 2012.

Baumgardner, D. and Korolev, A.: Airspeed corrections for optical array probe sample volumes, Journal of Atmospheric and Oceanic Technology, 14, 1224–1229, 1997.

Baumgardner, D., Jonsson, H., Dawson, W., O'Connor, D., and Newton, R.: The cloud, aerosol and precipitation spectrometer: a new instrument for cloud investigations, Atmospheric research, 59, 251–264, 2001.

Baumgardner, D., Brenguier, J., Bucholtz, A., Coe, H., DeMott, P., Garrett, T., Gayet, J., Hermann, M., Heymsfield, A., Korolev, A., et al.: Airborne instruments to measure atmospheric aerosol particles, clouds and radiation: A cook's tour of mature and emerging technology, Atmospheric Research, 102, 10–29, 2011.

Beals, M. J., Fugal, J. P., Shaw, R. A., Lu, J., Spuler, S. M., and Stith, J. L.: Holographic measurements of inhomogeneous cloud mixing at the centimeter scale, Science, 350, 87–90, 2015.

Beck, A.: Observing the Microstructure of Orographic Clouds with HoloGondel, Ph.D. thesis, ETH Zurich, 2017.

Beck, A., Henneberger, J., Schöpfer, S., Fugal, J., and Lohmann, U.: HoloGondel: in situ cloud observations on a cable car in the Swiss Alps using a holographic imager, Atmospheric Measurement Techniques, 10, 459–476, 2017.

Beck, A., Henneberger, J., Fugal, J. P., David, R. O., Lacher, L., Lohmann, U., and Möhler, O.: Impact of surface and near-surface processes on ice crystal concentrations measured at mountain-top research stations., Atmospheric Chemistry & Physics, 18, 2018.

Bendix, J.: A satellite-based climatology of fog and low-level stratus in Germany and adjacent areas, Atmospheric Research, 64, 3–18, 2002.

Bennartz, R.: Global assessment of marine boundary layer cloud droplet number concentration from satellite, J. Geophys. Res.: Atmospheres, 112, https://doi.org/10.1029/2006JD007547, 2007.

Bergeron, T.: On the physics of clouds and precipitation, Proc. 5th Assembly UGGI, Lisbon, Portugal, 1935, pp. 156–180, 1935.

Bergeron, T.: On the low-level redistribution of atmospheric water caused by orography, in: Suppl. Proc. Int. Conf. Cloud Phys., Tokyo, 1965, pp. 96–100, 1965.

Bergot, T.: Small-scale structure of radiation fog: a large-eddy simulation study, Quarterly Journal of the Royal Meteorological Society, 139, 1099–1112, 2013.

Bergot, T., Terradellas, E., Cuxart, J., Mira, A., Liechti, O., Mueller, M., and Nielsen, N. W.: Intercomparison of single-column numerical models for the prediction of radiation fog, Journal of applied meteorology and climatology, 46, 504–521, 2007.

Boose, Y., Welti, A., Atkinson, J., Ramelli, F., Danielczok, A., Bingemer, H. G., Ploetze, M., Sierau, B., Kanji, Z. A., and Lohmann, U.: Heterogeneous ice nucleation on dust particles sourced from nine deserts worldwide–Part 1: Immersion freezing, Atmospheric Chemistry and Physics, 16, 15 075–15 095, 2016.

Borrmann, S., Jaenicke, R., and Neumann, P.: On spatial distributions and inter-droplet distances measured in stratus clouds with in-line holography, Atmospheric research, 29, 229–245, 1993.

Borys, R. D., Lowenthal, D. H., and Mitchell, D. L.: The relationships among cloud microphysics, chemistry, and precipitation rate in cold mountain clouds, Atmospheric Environment, 34, 2593–2602, 2000.

Borys, R. D., Lowenthal, D. H., Cohn, S. A., and Brown, W. O.: Mountaintop and radar measurements of anthropogenic aerosol effects on snow growth and snowfall rate, Geophysical Research Letters, 30, 2003.

Boucher, O., Randall, D., Artaxo, P., Bretherton, C., Feingold, G., Forster, P., Kerminen, V.-M., Kondo, Y., Liao, H., Lohmann, U., et al.: Clouds and aerosols, in: Climate change 2013: the physical science basis. Contribution of Working Group I to the Fifth Assessment Report of the Intergovernmental Panel on Climate Change, pp. 571–657, Cambridge University Press, 2013.

Brenguier, J.-L.: Observations of cloud microstructure at the centimeter scale, Journal of Applied Meteorology, 32, 783–793, 1993.

Brenguier, J.-L., Bachalo, W. D., Chuang, P. Y., Esposito, B. M., Fugal, J., Garrett, T., Gayet, J.-F., Gerber, H., Heymsfield, A., Kokhanovsky, A., et al.: In situ measurements of cloud and

precipitation particles, Airborne Measurements for Environmental Research: Methods and Instruments, pp. 225–301, 2013.

Bühl, J., Seifert, P., Myagkov, A., and Ansmann, A.: Measuring ice-and liquid-water properties in mixed-phase cloud layers at the Leipzig Cloudnet station, 2016.

Bühl, J., Seifert, P., Radenz, M., Baars, H., and Ansmann, A.: Ice crystal number concentration from lidar, cloud radar and radar wind profiler measurements., Atmospheric Measurement Techniques, 12, 2019.

Cantrell, W. and Heymsfield, A.: Production of ice in tropospheric clouds: A review, Bulletin of the American Meteorological Society, 86, 795–808, 2005.

Canut, G., Couvreux, F., Lothon, M., Legain, D., Piguet, B., Lampert, A., Maurel, W., and Moulin, E.: Turbulence fluxes and variances measured with a sonic anemometer mounted on a tethered balloon, Atmospheric Measurement Techniques, 9, 4375–4386, 2016.

Carvalho, E., Sindt, C., Verdier, A., Galan, C., O'Donoghue, L., Parks, S., and Thibaudon, M.: Performance of the Coriolis air sampler, a high-volume aerosol-collection system for quantification of airborne spores and pollen grains, Aerobiologia, 24, 191–201, 2008.

Cermak, J., Eastman, R. M., Bendix, J., and Warren, S. G.: European climatology of fog and low stratus based on geostationary satellite observations, Q. J. R. Meteorol. Soc.: A journal of the atmospheric sciences, applied meteorology and physical oceanography, 135, 2125–2130, 2009.

Chen, C. and Cotton, W. R.: The physics of the marine stratocumulus-capped mixed layer, Journal of the atmospheric sciences, 44, 2951–2977, 1987.

Colle, B. A., Smith, R. B., and Wesley, D. A.: Theory, observations, and predictions of orographic precipitation, in: Mountain Weather Research and Forecasting, pp. 291–344, Springer, 2013.

Connolly, P., Emersic, C., and Field, P.: A laboratory investigation into the aggregation efficiency of small ice crystals, Atmospheric Chemistry and Physics, 12, 2055–2076, 2012.

Conway, B., Caughey, S., Bentley, A., and Turton, J.: Ground-based and airborne holography of ice and water clouds, Atmospheric Environment (1967), 16, 1193–1207, 1982.

Cotton, R., Osborne, S., Ulanowski, Z., Hirst, E., Kaye, P. H., and Greenaway, R.: The ability of the Small Ice Detector (SID-2) to characterize cloud particle and aerosol morphologies obtained during flights of the FAAM BAe-146 research aircraft, Journal of Atmospheric and Oceanic Technology, 27, 290–303, 2010.

Crawford, I., Bower, K., Choularton, T., Dearden, C., Crosier, J., Westbrook, C., Capes, G., Coes, H., Connolly, P., Dorsey, J., et al.: Ice formation and development in aged, wintertime cumulus over the UK: observations and modelling, Atmospheric Chemistry and Physics, 12, 4963–4985, 2012.

Creamean, J. M., Primm, K. M., Tolbert, M. A., Hall, E. G., Wendell, J., Jordan, A., Sheridan, P. J., Smith, J., and Schnell, R. C.: HOVERCAT: a novel aerial system for evaluation of aerosol-cloud interactions., Atmospheric Measurement Techniques, 11, 2018.

Crewell, S. and Lohnert, U.: Accuracy of boundary layer temperature profiles retrieved with multifrequency multiangle microwave radiometry, IEEE Transactions on Geoscience and Remote Sensing, 45, 2195–2201, 2007.

Cronce, M., Rauber, R. M., Knupp, K. R., Jewett, B. F., Walters, J. T., and Phillips, D.: Vertical motions in precipitation bands in three winter cyclones, Journal of Applied Meteorology and Climatology, 46, 1523–1543, 2007.

Crosier, J., Bower, K., Choularton, T., Westbrook, C. D., Connolly, P., Cui, Z., Crawford, I., Capes, G., Coe, H., Dorsey, J., et al.: Observations of ice multiplication in a weakly convective cell embedded in supercooled mid-level stratus, Atmospheric Chemistry and Physics, 11, 257–273, 2011.

Crosier, J., Choularton, T., Westbrook, C., Blyth, A., Bower, K., Connolly, P., Dearden, C., Gallagher, M., Cui, Z., and Nicol, J.: Microphysical properties of cold frontal rainbands, Quarterly Journal of the Royal Meteorological Society, 140, 1257–1268, 2014.

David, R., Cascajo-Castresana, M., Brennan, K., Rösch, M., Els, N., Werz, J., Weichlinger, V., Boynton, L., Bogler, S., Borduas-Dedekind, N., et al.: Development of the DRoplet Ice Nuclei Counter Zurich (DRINCZ): validation and application to field-collected snow samples, Atmospheric Measurement Techniques, 12, 6865–6888, 2019a.

David, R. O., Marcolli, C., Fahrni, J., Qiu, Y., Sirkin, Y. A. P., Molinero, V., Mahrt, F., Brühwiler, D., Lohmann, U., and Kanji, Z. A.: Pore condensation and freezing is responsible for ice formation below water saturation for porous particles, Proceedings of the National Academy of Sciences, 116, 8184–8189, 2019b.

De Boer, G., Morrison, H., Shupe, M., and Hildner, R.: Evidence of liquid dependent ice nucleation in high-latitude stratiform clouds from surface remote sensors, Geophysical Research Letters, 38, 2011.

DeMott, P. J., Prenni, A. J., Liu, X., Kreidenweis, S. M., Petters, M. D., Twohy, C. H., Richardson, M., Eidhammer, T., and Rogers, D.: Predicting global atmospheric ice nuclei distributions and their impacts on climate, Proceedings of the National Academy of Sciences, 107, 11 217–11 222, 2010.

Deng, M., Mace, G. G., Wang, Z., and Lawson, R. P.: Evaluation of several A-Train ice cloud retrieval products with in situ measurements collected during the SPARTICUS campaign, Journal of applied meteorology and climatology, 52, 1014–1030, 2013.

Desai, N., Glienke, S., Fugal, J., and Shaw, R.: Search for microphysical signatures of stochastic condensation in marine boundary layer clouds using airborne digital holography, Journal of Geophysical Research: Atmospheres, 124, 2739–2752, 2019.

Donat, M. G., Lowry, A. L., Alexander, L. V., O'Gorman, P. A., and Maher, N.: More extreme precipitation in the world's dry and wet regions, Nature Climate Change, 6, 508–513, 2016.

Dong, Y., Oraltay, R. G., and Hallett, J.: Ice particle generation during evaporation, Atmospheric research, 32, 45–53, 1994.

Dorsi, S., Shupe, M., Persson, P., Kingsmill, D., and Avallone, L.: Phase-specific characteristics of wintertime clouds across a midlatitude mountain range, Monthly Weather Review, 143, 4181–4197, 2015.

Doviak, R. J. and Zrnić, D. S.: 8 - Precipitation Measurements, in: Doppler Radar and Weather Observations (Second Edition), edited by Doviak, R. J. and Zrnić, D. S., pp. 209 – 279, Academic Press, San Diego, second edition edn., https://doi.org/https://doi.

org/10.1016/B978-0-12-221422-6.50013-9, URL http://www.sciencedirect.com/science/article/pii/B9780122214226500139, 1993.

Durran, D. R.: Mountain waves and downslope winds, in: Atmospheric processes over complex terrain, pp. 59–81, Springer, 1990.

Eirund, G. K., Possner, A., and Lohmann, U.: Response of Arctic mixed-phase clouds to aerosol perturbations under different surface forcings, Atmospheric Chemistry and Physics, 19, 9847–9864, 2019.

Elston, J., Argrow, B., Stachura, M., Weibel, D., Lawrence, D., and Pope, D.: Overview of small fixed-wing unmanned aircraft for meteorological sampling, Journal of Atmospheric and Oceanic Technology, 32, 97–115, 2015.

Engelmann, R., Kanitz, T., Baars, H., Heese, B., Althausen, D., Skupin, A., Wandinger, U., Komppula, M., Stachlewska, I. S., Amiridis, V., et al.: The automated multiwavelength Raman polarization and water-vapor lidar PollyXT: the neXT generation, Atmospheric Measurement Techniques, 9, 1767–1784, 2016.

Evans, A. G., Locatelli, J. D., Stoelinga, M. T., and Hobbs, P. V.: The IMPROVE-1 storm of 1–2 February 2001. Part II: Cloud structures and the growth of precipitation, Journal of the atmospheric sciences, 62, 3456–3473, 2005.

Fabbian, D., de Dear, R., and Lellyett, S.: Application of artificial neural network forecasts to predict fog at Canberra International Airport, Weather and forecasting, 22, 372–381, 2007.

Field, P. and Heymsfield, A.: Importance of snow to global precipitation, Geophysical Research Letters, 42, 9512–9520, 2015.

Field, P., Wood, R., Brown, P., Kaye, P. H., Hirst, E., Greenaway, R., and Smith, J.: Ice particle interarrival times measured with a fast FSSP, Journal of Atmospheric and Oceanic Technology, 20, 249–261, 2003.

Field, P. R., Lawson, R. P., Brown, P. R., Lloyd, G., Westbrook, C., Moisseev, D., Miltenberger, A., Nenes, A., Blyth, A., Choularton, T., et al.: Secondary ice production: Current state of the science and recommendations for the future, Meteorological Monographs, 58, 7–1, 2017.

Findeisen, W.: Kolloid-meteorologische Vorgänge bei Neiderschlags-bildung, Meteor. Z, 55, 121–133, 1938.

Fraser, A. B., Easter, R. C., and Hobbs, P. V.: A theoretical study of the flow of air and fallout of solid precipitation over mountainous terrain: Part I. Airflow model, Journal of the Atmospheric Sciences, 30, 801–812, 1973.

Frei, C. and Schär, C.: A precipitation climatology of the Alps from high-resolution rain-gauge observations, International Journal of Climatology: A Journal of the Royal Meteorological Society, 18, 873–900, 1998.

Fu, Q. and Liou, K. N.: Parameterization of the radiative properties of cirrus clouds, Journal of the Atmospheric Sciences, 50, 2008–2025, 1993.

Fugal, J. P. and Shaw, R. A.: Cloud particle size distributions measured with an airborne digital in-line holographic instrument, Atmospheric Measurement Techniques, 2, 259–271, 2009.

Fugal, J. P., Schulz, T. J., and Shaw, R. A.: Practical methods for automated reconstruction and characterization of particles in digital in-line holograms, Measurement Science and Technology, 20, 075 501, 2009.

Fukuta, N. and Takahashi, T.: The growth of atmospheric ice crystals: A summary of findings in vertical supercooled cloud tunnel studies, Journal of the atmospheric sciences, 56, 1963–1979, 1999.

Garcıa-Garcıa, F., Virafuentes, U., and Montero-Martınez, G.: Fine-scale measurements of fog-droplet concentrations: A preliminary assessment, Atmospheric research, 64, 179–189, 2002.

Garrett, T., Fallgatter, C., Shkurko, K., and Howlett, D.: Fall speed measurement and high-resolution multi-angle photography of hydrometeors in free fall, Atmospheric Measurement Techniques, 5, 2625–2633, 2012.

Geerts, B., Miao, Q., Yang, Y., Rasmussen, R., and Breed, D.: An airborne profiling radar study of the impact of glaciogenic cloud seeding on snowfall from winter orographic clouds, Journal of the atmospheric sciences, 67, 3286–3302, 2010.

Geerts, B., Miao, Q., and Yang, Y.: Boundary layer turbulence and orographic precipitation growth in cold clouds: Evidence from profiling airborne radar data, Journal of the atmospheric sciences, 68, 2344–2365, 2011.

Geerts, B., Pokharel, B., and Kristovich, D. A.: Blowing snow as a natural glaciogenic cloud seeding mechanism, Monthly Weather Review, 143, 5017–5033, 2015.

Gerber, H., Frick, G., Malinowski, S., Brenguier, J., and Burnet, F.: Holes and entrainment in stratocumulus, Journal of the atmospheric sciences, 62, 443–459, 2005.

Glen, A. and Brooks, S.: A new method for measuring optical scattering properties of atmospherically relevant dusts using the Cloud and Aerosol Spectrometer with Polarization (CASPOL), 1foldr Import 2019-10-08 Batch 7, 2013.

Glienke, S., Kostinski, A., Fugal, J., Shaw, R., Borrmann, S., and Stith, J.: Cloud droplets to drizzle: Contribution of transition drops to microphysical and optical properties of marine stratocumulus clouds, Geophysical Research Letters, 44, 8002–8010, 2017.

Glienke, S., Kostinski, A. B., Shaw, R. A., Larsen, M. L., Fugal, J. P., Schlenczek, O., and Borrmann, S.: Holographic observations of centimeter-scale nonuniformities within marine stratocumulus clouds, Journal of the Atmospheric Sciences, 77, 499–512, 2020.

Görsdorf, U., Lehmann, V., Bauer-Pfundstein, M., Peters, G., Vavriv, D., Vinogradov, V., and Volkov, V.: A 35-GHz polarimetric Doppler radar for long-term observations of cloud parameters—Description of system and data processing, Journal of Atmospheric and Oceanic Technology, 32, 675–690, 2015.

Grazioli, J., Lloyd, G., Panziera, L., Hoyle, C. R., Connolly, P. J., Henneberger, J., and Berne, A.: Polarimetric radar and in situ observations of riming and snowfall microphysics during CLACE 2014, Atmospheric Chemistry and Physics, 15, 13 787–13 802, 2015.

Gultepe, I., Tardif, R., Michaelides, S., Cermak, J., Bott, A., Bendix, J., Müller, M. D., Pagowski, M., Hansen, B., Ellrod, G., et al.: Fog research: A review of past achievements and future perspectives, Pure and Applied Geophysics, 164, 1121–1159, 2007.

Hallett, J. and Mossop, S.: Production of secondary ice particles during the riming process, Nature, 249, 26, 1974.

Harrington, J. Y., Reisin, T., Cotton, W. R., and Kreidenweis, S. M.: Cloud resolving simulations of Arctic stratus: Part II: Transition-season clouds, Atmospheric Research, 51, 45–75, 1999.

Hartmann, D. L., Ockert-Bell, M. E., and Michelsen, M. L.: The effect of cloud type on Earth's energy balance: Global analysis, Journal of Climate, 5, 1281–1304, 1992.

Hauf, T. and Schröder, F.: Aircraft icing research flights in embedded convection, Meteorology and Atmospheric Physics, 91, 247–265, 2006.

Henneberger, J., Fugal, J., Stetzer, O., and Lohmann, U.: HOLIMO II: a digital holographic instrument for ground-based in situ observations of microphysical properties of mixed-phase clouds, Atmospheric Measurement Techniques, 6, 2975–2987, 2013.

Hill, F., Browning, K., and Bader, M.: Radar and raingauge observations of orographic rain over south Wales, Quarterly Journal of the Royal Meteorological Society, 107, 643–670, 1981.

Hobbs, P. V. and Rangno, A. L.: Ice particle concentrations in clouds, Journal of the atmospheric sciences, 42, 2523–2549, 1985.

Hogan, R. J., Field, P., Illingworth, A., Cotton, R., and Choularton, T.: Properties of embedded convection in warm-frontal mixed-phase cloud from aircraft and polarimetric radar, Quarterly Journal of the Royal Meteorological Society: A journal of the atmospheric sciences, applied meteorology and physical oceanography, 128, 451–476, 2002.

Hoose, C. and Möhler, O.: Heterogeneous ice nucleation on atmospheric aerosols: a review of results from laboratory experiments, Atmos. Chem. Phys, 12, 9817–9854, 2012.

Houze Jr, R. A.: Orographic effects on precipitating clouds, Reviews of Geophysics, 50, 2012.

Houze Jr, R. A.: Cloud dynamics, Academic press, 2014.

Houze Jr, R. A. and Medina, S.: Turbulence as a mechanism for orographic precipitation enhancement, Journal of the atmospheric sciences, 62, 3599–3623, 2005.

Houze Jr, R. A., Rutledge, S. A., Matejka, T. J., and Hobbs, P. V.: The mesoscale and microscale structure and organization of clouds and precipitation in midlatitude cyclones. III: Air motions and precipitation growth in a warm-frontal rainband, Journal of the Atmospheric Sciences, 38, 639–649, 1981.

Ikeda, K., Rasmussen, R. M., Hall, W. D., and Thompson, G.: Observations of freezing drizzle in extratropical cyclonic storms during IMPROVE-2, Journal of the Atmospheric Sciences, 64, 3016–3043, 2007.

Jiang, H., Cotton, W. R., Pinto, J. O., Curry, J. A., and Weissbluth, M. J.: Cloud resolving simulations of mixed-phase Arctic stratus observed during BASE: Sensitivity to concentration of ice crystals and large-scale heat and moisture advection, Journal of the atmospheric sciences, 57, 2105–2117, 2000.

Jiang, Q.: Moist dynamics and orographic precipitation, Tellus A: Dynamic Meteorology and Oceanography, 55, 301–316, 2003.

Jiang, Q. and Smith, R. B.: Cloud timescales and orographic precipitation, Journal of the atmospheric sciences, 60, 1543–1559, 2003.

Kanji, Z. A., Ladino, L. A., Wex, H., Boose, Y., Burkert-Kohn, M., Cziczo, D. J., and Krämer, M.: Overview of ice nucleating particles, Meteorological Monographs, 58, 1–1, 2017.

Keeler, J. M., Jewett, B. F., Rauber, R. M., McFarquhar, G. M., Rasmussen, R. M., Xue, L., Liu, C., and Thompson, G.: Dynamics of cloud-top generating cells in winter cyclones. Part II: Radiative and instability forcing, Journal of the Atmospheric Sciences, 73, 1529–1553, 2016.

Kirshbaum, D. J., Adler, B., Kalthoff, N., Barthlott, C., and Serafin, S.: Moist orographic

convection: Physical mechanisms and links to surface-exchange processes, Atmosphere, 9, 80, 2018.

Knight, C. A.: Ice growth from the vapor at- 5° C, Journal of the atmospheric sciences, 69, 2031–2040, 2012.

Knollenberg, R.: Techniques for probing cloud microstructure, in: In: Clouds-Their formation, optical properties, and effects; Proceedings of the Symposium, Williamsburg, VA, May 13, 14, 1980.(A82-12426 02-47) New York, Academic Press, 1981, p. 15-89; Discussion, p. 90, 91., pp. 15–89, 1981.

Knollenberg, R. G.: The optical array: An alternative to scattering or extinction for airborne particle size determination, Journal of Applied Meteorology, 9, 86–103, 1970.

Köhler, C., Steiner, A., Saint-Drenan, Y.-M., Ernst, D., Bergmann-Dick, A., Zirkelbach, M., Bouallègue, Z. B., Metzinger, I., and Ritter, B.: Critical weather situations for renewable energies–Part B: Low stratus risk for solar power, Renewable Energy, 101, 794–803, 2017.

Kollias, P., Miller, M. A., Luke, E. P., Johnson, K. L., Clothiaux, E. E., Moran, K. P., Widener, K. B., and Albrecht, B. A.: The Atmospheric Radiation Measurement Program cloud profiling radars: Second-generation sampling strategies, processing, and cloud data products, Journal of Atmospheric and Oceanic Technology, 24, 1199–1214, 2007.

Korolev, A.: Limitations of the Wegener–Bergeron–Findeisen mechanism in the evolution of mixed-phase clouds, Journal of the Atmospheric Sciences, 64, 3372–3375, 2007.

Korolev, A. and Isaac, G.: Phase transformation of mixed-phase clouds, Quarterly Journal of the Royal Meteorological Society: A journal of the atmospheric sciences, applied meteorology and physical oceanography, 129, 19–38, 2003.

Korolev, A. and Isaac, G. A.: Relative humidity in liquid, mixed-phase, and ice clouds, Journal of the atmospheric sciences, 63, 2865–2880, 2006.

Korolev, A. and Leisner, T.: Review of experimental studies on secondary ice production, Atmospheric Chemistry and Physics Discussions, 2020, 1–42, https://doi.org/10.5194/acp-2020-537, URL `https://www.atmos-chem-phys-discuss.net/acp-2020-537/`, 2020.

Korolev, A. and Mazin, I.: Zones of increased and decreased droplet concentration in stratiform clouds, Journal of Applied Meteorology, 32, 760–773, 1993.

Korolev, A., Isaac, G., and Hallett, J.: Ice particle habits in Arctic clouds, Geophysical research letters, 26, 1299–1302, 1999.

Korolev, A., Emery, E., Strapp, J., Cober, S., Isaac, G., Wasey, M., and Marcotte, D.: Small ice particles in tropospheric clouds: Fact or artifact? Airborne Icing Instrumentation Evaluation Experiment, Bulletin of the American Meteorological Society, 92, 967–973, 2011.

Korolev, A., Khain, A., Pinsky, M., and French, J.: Theoretical study of mixing in liquid clouds–Part 1: Classical concepts, Atmos. Chem. Phys, 16, 2016, 2016.

Korolev, A., McFarquhar, G., Field, P. R., Franklin, C., Lawson, P., Wang, Z., Williams, E., Abel, S. J., Axisa, D., Borrmann, S., et al.: Mixed-phase clouds: Progress and challenges, Meteorological Monographs, 58, 5–1, 2017.

Korolev, A., Heckman, I., Wolde, M., Ackerman, A. S., Fridlind, A. M., Ladino, L. A., Lawson, R. P., Milbrandt, J., and Williams, E.: A new look at the environmental conditions favorable to secondary ice production, Atmospheric Chemistry and Physics, 20, 1391–1429,

https://doi.org/10.5194/acp-20-1391-2020, URL https://www.atmos-chem-phys.net/20/1391/2020/, 2020.

Korolev, A. V. and Mazin, I. P.: Supersaturation of water vapor in clouds, Journal of the atmospheric sciences, 60, 2957–2974, 2003.

Korolev, A. V., Isaac, G. A., Cober, S. G., Strapp, J. W., and Hallett, J.: Microphysical characterization of mixed-phase clouds, Quarterly Journal of the Royal Meteorological Society: A journal of the atmospheric sciences, applied meteorology and physical oceanography, 129, 39–65, 2003.

Kozikowska, A., Haman, K., and Supronowicz, J.: Preliminary results of an investigation of the spatial distribution of fog droplets by a holographic method, Quarterly Journal of the Royal Meteorological Society, 110, 65–73, 1984.

Kumjian, M. R., Rutledge, S. A., Rasmussen, R. M., Kennedy, P. C., and Dixon, M.: High-resolution polarimetric radar observations of snow-generating cells, Journal of Applied Meteorology and Climatology, 53, 1636–1658, 2014.

Lamb, D. and Verlinde, J.: Physics and chemistry of clouds, Cambridge University Press, 2011.

Lance, S., Brock, C., Rogers, D., and Gordon, J. A.: Water droplet calibration of the Cloud Droplet Probe (CDP) and in-flight performance in liquid, ice and mixed-phase clouds during ARCPAC, Atmospheric Measurement Techniques, 3, 1683, 2010.

Langham, E. and Mason, B. J.-N.: The heterogeneous and homogeneous nucleation of supercooled water, Proceedings of the Royal Society of London. Series A. Mathematical and Physical Sciences, 247, 493–504, 1958.

Larsen, M. L. and Shaw, R. A.: A method for computing the three-dimensional radial distribution function of cloud particles from holographic images, Atmospheric Measurement Techniques, 11, 4261–4272, 2018.

Larsen, M. L., Shaw, R. A., Kostinski, A. B., and Glienke, S.: Fine-scale droplet clustering in atmospheric clouds: 3D radial distribution function from airborne digital holography, Physical review letters, 121, 204 501, 2018.

Lauber, A., Kiselev, A., Pander, T., Handmann, P., and Leisner, T.: Secondary ice formation during freezing of levitated droplets, Journal of the Atmospheric Sciences, 75, 2815–2826, 2018.

Lawson, P., Gurganus, C., Woods, S., and Bruintjes, R.: Aircraft observations of cumulus microphysics ranging from the tropics to midlatitudes: Implications for a "new" secondary ice process, Journal of the Atmospheric Sciences, 74, 2899–2920, 2017.

Lawson, R. and Cormack, R.: Theoretical design and preliminary tests of two new particle spectrometers for cloud microphysics research, Atmospheric research, 35, 315–348, 1995.

Lawson, R. P., Stewart, R. E., and Angus, L. J.: Observations and numerical simulations of the origin and development of very large snowflakes, Journal of the atmospheric sciences, 55, 3209–3229, 1998.

Lawson, R. P., Baker, B. A., Schmitt, C. G., and Jensen, T.: An overview of microphysical properties of Arctic clouds observed in May and July 1998 during FIRE ACE, Journal of Geophysical Research: Atmospheres, 106, 14 989–15 014, 2001.

Lawson, R. P., O'connor, D., Zmarzly, P., Weaver, K., Baker, B., Mo, Q., and Jonsson, H.:

The 2D-S (stereo) probe: Design and preliminary tests of a new airborne, high-speed, high-resolution particle imaging probe, Journal of Atmospheric and Oceanic Technology, 23, 1462–1477, 2006.

Lawson, R. P., Stamnes, K., Stamnes, J., Zmarzly, P., Koskuliks, J., Roden, C., Mo, Q., Carrithers, M., and Bland, G. L.: Deployment of a tethered-balloon system for microphysics and radiative measurements in mixed-phase clouds at Ny-Ålesund and South Pole, Journal of Atmospheric and Oceanic Technology, 28, 656–670, 2011.

Liou, K.-N.: An introduction to atmospheric radiation, Elsevier, 2002.

Liu, Y., Shupe, M. D., Wang, Z., and Mace, G.: Cloud vertical distribution from combined surface and space radar-lidar observations at two Arctic atmospheric observatories, Atmos. Chem. Phys., 17, 5973–5989, 2017.

Lloyd, G., Choularton, T., Bower, K., Gallagher, M., Connolly, P., Flynn, M., Farrington, R., Crosier, J., Schlenczek, O., Fugal, J., et al.: The origins of ice crystals measured in mixed-phase clouds at the high-alpine site Jungfraujoch, Atmospheric Chemistry and Physics, 15, 12 953–12 969, 2015.

Loescher, K. A., Young, G. S., Colle, B. A., and Winstead, N. S.: Climatology of barrier jets along the Alaskan coast. Part I: Spatial and temporal distributions, Monthly weather review, 134, 437–453, 2006.

Löffler-Mang, M. and Joss, J.: An optical disdrometer for measuring size and velocity of hydrometeors, Journal of Atmospheric and Oceanic Technology, 17, 130–139, 2000.

Lohmann, U., Henneberger, J., Henneberg, O., Fugal, J., Bühl, J., and Kanji, Z. A.: Persistence of orographic mixed-phase clouds, Geophysical Research Letters, 43, 10–512, 2016a.

Lohmann, U., Lüönd, F., and Mahrt, F.: An introduction to clouds: From the microscale to climate, Cambridge University Press, 2016b.

Löhnert, U. and Crewell, S.: Accuracy of cloud liquid water path from ground-based microwave radiometry 1. Dependency on cloud model statistics, Radio Science, 38, 2003.

Löhnert, U., Schween, J., Acquistapace, C., Ebell, K., Maahn, M., Barrera-Verdejo, M., Hirsikko, A., Bohn, B., Knaps, A., O'connor, E., et al.: JOYCE: Jülich observatory for cloud evolution, Bulletin of the American Meteorological Society, 96, 1157–1174, 2015.

Lowenthal, D., Hallar, A. G., McCubbin, I., David, R., Borys, R., Blossey, P., Muhlbauer, A., Kuang, Z., and Moore, M.: Isotopic fractionation in wintertime orographic clouds, Journal of Atmospheric and Oceanic Technology, 33, 2663–2678, 2016.

Lowenthal, D. H., Borys, R. D., Cotton, W., Saleeby, S., Cohn, S. A., and Brown, W. O.: The altitude of snow growth by riming and vapor deposition in mixed-phase orographic clouds, Atmospheric environment, 45, 519–522, 2011.

Lowenthal, D. H., Hallar, A., David, R. O., McCubbin, I. B., Borys, R. D., and Mace, G. G.: Mixed-phase orographic cloud microphysics during StormVEx and IFRACS, Atmospheric Chemistry and Physics, 19, 5387–5401, 2019.

Lu, J., Fugal, J. P., Nordsiek, H., Saw, E. W., Shaw, R. A., and Yang, W.: Lagrangian particle tracking in three dimensions via single-camera in-line digital holography, New Journal of Physics, 10, 125 013, 2008.

Magono, C. and Lee, C. W.: Meteorological classification of natural snow crystals, Journal of the Faculty of Science, Hokkaido University. Series 7, Geophysics, 2, 321–335, 1966.

Maletto, A., McKendry, I., and Strawbridge, K.: Profiles of particulate matter size distributions using a balloon-borne lightweight aerosol spectrometer in the planetary boundary layer, Atmospheric Environment, 37, 661–670, 2003.

Marchand, R., Mace, G. G., Ackerman, T., and Stephens, G.: Hydrometeor detection using CloudSat—An Earth-orbiting 94-GHz cloud radar, J. Atmos. Ocean. Technol., 25, 519–533, 2008.

Marcolli, C.: Deposition nucleation viewed as homogeneous or immersion freezing in pores and cavities, Atmospheric Chemistry and Physics, 14, 2071–2104, 2014.

Marshall, J. S. and Langleben, M. P.: A theory of snow-crystal habit and growth, Journal of Meteorology, 11, 104–120, 1954.

Marwitz, J. D.: The kinematics of orographic airflow during Sierra storms, Journal of the atmospheric sciences, 40, 1218–1227, 1983.

Mason, B. and Maybank, J.: The fragmentation and electrification of freezing water drops, Quarterly Journal of the Royal Meteorological Society, 86, 176–185, 1960.

Matrosov, S. Y., Mace, G. G., Marchand, R., Shupe, M. D., Hallar, A. G., and McCubbin, I. B.: Observations of ice crystal habits with a scanning polarimetric W-band radar at slant linear depolarization ratio mode, Journal of Atmospheric and Oceanic Technology, 29, 989–1008, 2012.

Matus, A. V. and L'Ecuyer, T. S.: The role of cloud phase in Earth's radiation budget, Journal of Geophysical Research: Atmospheres, 122, 2559–2578, 2017.

Mazzola, M., Busetto, M., Ferrero, L., Viola, A. P., and Cappelletti, D.: AGAP: an atmospheric gondola for aerosol profiling, Rendiconti Lincei, 27, 105–113, 2016.

Medina, S. and Houze, R. A.: Air motions and precipitation growth in Alpine storms, Quarterly Journal of the Royal Meteorological Society: A journal of the atmospheric sciences, applied meteorology and physical oceanography, 129, 345–371, 2003.

Medina, S. and Houze Jr, R. A.: Small-scale precipitation elements in midlatitude cyclones crossing the California Sierra Nevada, Monthly Weather Review, 143, 2842–2870, 2015.

Medina, S., Smull, B. F., Houze Jr, R. A., and Steiner, M.: Cross-barrier flow during orographic precipitation events: Results from MAP and IMPROVE, Journal of the atmospheric sciences, 62, 3580–3598, 2005.

Medina, S., Sukovich, E., and Houze Jr, R. A.: Vertical structures of precipitation in cyclones crossing the Oregon Cascades, Monthly weather review, 135, 3565–3586, 2007.

Melchionna, S., Bauer, M., and Peters, G.: A new algorithm for the extraction of cloud parameters using multipeak analysis of cloud radar data–first application and preliminary results, Meteorologische Zeitschrift, 17, 613–620, 2008.

Mellado, J. P.: Cloud-top entrainment in stratocumulus clouds, Annual Review of Fluid Mechanics, 49, 145–169, 2017.

Miles, N. L., Verlinde, J., and Clothiaux, E. E.: Cloud droplet size distributions in low-level stratiform clouds, Journal of the atmospheric sciences, 57, 295–311, 2000.

Mitchell, D. L.: Use of mass-and area-dimensional power laws for determining precipitation particle terminal velocities, Journal of the atmospheric sciences, 53, 1710–1723, 1996.

Mitchell, D. L., Zhang, R., and Pitter, R. L.: Mass-dimensional relationships for ice particles and the influence of riming on snowfall rates, Journal of applied meteorology, 29, 153–163, 1990.

Morrison, H., Zuidema, P., Ackerman, A. S., Avramov, A., De Boer, G., Fan, J., Fridlind, A. M., Hashino, T., Harrington, J. Y., Luo, Y., et al.: Intercomparison of cloud model simulations of Arctic mixed-phase boundary layer clouds observed during SHEBA/FIRE-ACE, Journal of Advances in Modeling Earth Systems, 3, 2011.

Morrison, H., De Boer, G., Feingold, G., Harrington, J., Shupe, M. D., and Sulia, K.: Resilience of persistent Arctic mixed-phase clouds, Nature Geoscience, 5, 11–17, 2012.

Mossop, S.: The influence of drop size distribution on the production of secondary ice particles during graupel growth, Quarterly Journal of the Royal Meteorological Society, 104, 323–330, 1978.

Müller, M. D., Masbou, M., and Bott, A.: Three-dimensional fog forecasting in complex terrain, Quarterly Journal of the Royal Meteorological Society, 136, 2189–2202, 2010.

Mülmenstädt, J., Sourdeval, O., Delanoë, J., and Quaas, J.: Frequency of occurrence of rain from liquid-, mixed-, and ice-phase clouds derived from A-Train satellite retrievals, Geophysical Research Letters, 42, 6502–6509, 2015.

Murray, B., O'sullivan, D., Atkinson, J., and Webb, M.: Ice nucleation by particles immersed in supercooled cloud droplets, Chemical Society Reviews, 41, 6519–6554, 2012.

Myagkov, A., Seifert, P., Wandinger, U., Bühl, J., and Engelmann, R.: Relationship between temperature and apparent shape of pristine ice crystals derived from polarimetric cloud radar observations during the ACCEPT campaign, 2016.

Neiman, P. J., Ralph, F. M., White, A., Kingsmill, D., and Persson, P.: The statistical relationship between upslope flow and rainfall in California's coastal mountains: Observations during CALJET, Monthly Weather Review, 130, 1468–1492, 2002.

Neiman, P. J., Martin Ralph, F., Persson, P. O. G., White, A. B., Jorgensen, D. P., and Kingsmill, D. E.: Modification of fronts and precipitation by coastal blocking during an intense landfalling winter storm in southern California: Observations during CALJET, Monthly weather review, 132, 242–273, 2004.

North, G. R., Pyle, J. A., and Zhang, F.: Encyclopedia of atmospheric sciences, vol. 1, Elsevier, 2014.

Olson, J. B. and Colle, B. A.: Three-dimensional idealized simulations of barrier jets along the southeast coast of Alaska, Monthly weather review, 137, 391–413, 2009.

Olson, J. B., Colle, B. A., Bond, N. A., and Winstead, N.: A comparison of two coastal barrier jet events along the southeast Alaskan coast during the SARJET field experiment, Monthly weather review, 135, 2973–2994, 2007.

Oraltay, R. and Hallett, J.: Evaporation and melting of ice crystals: A laboratory study, Atmospheric research, 24, 169–189, 1989.

Overland, J. E. and Bond, N. A.: Observations and scale analysis of coastal wind jets, Monthly Weather Review, 123, 2934–2941, 1995.

Pagowski, M., Gultepe, I., and King, P.: Analysis and modeling of an extremely dense fog event in southern Ontario, Journal of applied meteorology, 43, 3–16, 2004.

Pinsky, M. and Khain, A.: Some effects of cloud turbulence on water–ice and ice–ice collisions, Atmospheric research, 47, 69–86, 1998.

Pinsky, M., Khain, A., Korolev, A., and Magaritz-Ronen, L.: Theoretical investigation of mixing in warm clouds–Part 2: Homogeneous mixing, Atmospheric Chemistry and Physics, 16, 9255–9272, 2016a.

Pinsky, M., Khain, A., Korolev, A., and Magaritz-Ronen, L.: Theoretical investigation of mixing in warm clouds–Part 2: Homogeneous mixing, Atmospheric Chemistry and Physics (Online), 16, 2016b.

Pinto, J. O.: Autumnal mixed-phase cloudy boundary layers in the Arctic, Journal of the atmospheric sciences, 55, 2016–2038, 1998.

Pinto, J. O., Curry, J. A., and Intrieri, J. M.: Cloud-aerosol interactions during autumn over Beaufort Sea, Journal of Geophysical Research: Atmospheres, 106, 15 077–15 097, 2001.

Plummer, D. M., McFarquhar, G. M., Rauber, R. M., Jewett, B. F., and Leon, D. C.: Structure and statistical analysis of the microphysical properties of generating cells in the comma head region of continental winter cyclones, Journal of the Atmospheric Sciences, 71, 4181–4203, 2014.

Plummer, D. M., McFarquhar, G. M., Rauber, R. M., Jewett, B. F., and Leon, D. C.: Microphysical properties of convectively generated fall streaks within the stratiform comma head region of continental winter cyclones, Journal of the Atmospheric Sciences, 72, 2465–2483, 2015.

Possner, A., Ekman, A. M., and Lohmann, U.: Cloud response and feedback processes in stratiform mixed-phase clouds perturbed by ship exhaust, Geophysical Research Letters, 44, 1964–1972, 2017.

Protat, A., Delanoë, J., Bouniol, D., Heymsfield, A., Bansemer, A., and Brown, P.: Evaluation of ice water content retrievals from cloud radar reflectivity and temperature using a large airborne in situ microphysical database, Journal of applied meteorology and climatology, 46, 557–572, 2007.

Pruppacher, H. R. and Klett, J. D.: Microphysics of clouds and precipitation, Nature, 284, 88–88, 1980.

Radenz, M., Bühl, J., Seifert, P., Griesche, H., and Engelmann, R.: peakTree: a framework for structure-preserving radar Doppler spectra analysis., Atmospheric Measurement Techniques, 12, 2019.

Ramelli, F., Beck, A., Henneberger, J., and Lohmann, U.: Using a holographic imager on a tethered balloon system for microphysical observations of boundary layer clouds, Atmospheric Measurement Techniques, 13, 925–939, https://doi.org/10.5194/amt-13-925-2020, URL `https://www.atmos-meas-tech.net/13/925/2020/`, 2020.

Randall, D., Coakley Jr, J., Fairall, C., Kropfli, R., and Lenschow, D.: Outlook for research on subtropical marine stratiform clouds, Bulletin of the American Meteorological Society, 65, 1290–1301, 1984.

Rasmussen, R. M., Geresdi, I., Thompson, G., Manning, K., and Karplus, E.: Freezing drizzle

formation in stably stratified layer clouds: The role of radiative cooling of cloud droplets, cloud condensation nuclei, and ice initiation, Journal of the atmospheric sciences, 59, 837–860, 2002.

Rauber, R. M. and Grant, L. O.: The characteristics and distribution of cloud water over the mountains of northern Colorado during wintertime storms. Part II: Spatial distribution and microphysical characteristics, Journal of climate and applied meteorology, 25, 489–504, 1986.

Rauber, R. M. and Tokay, A.: An explanation for the existence of supercooled water at the top of cold clouds, Journal of the Atmospheric Sciences, 48, 1005–1023, 1991.

Rauber, R. M., Plummer, D. M., Macomber, M. K., Rosenow, A. A., McFarquhar, G. M., Jewett, B. F., Leon, D., Owens, N., and Keeler, J. M.: The role of cloud-top generating cells and boundary layer circulations in the finescale radar structure of a winter cyclone over the Great Lakes, Monthly Weather Review, 143, 2291–2318, 2015.

Raupach, S., Vössing, H., Curtius, J., and Borrmann, S.: Digital crossed-beam holography for in situ imaging of atmospheric ice particles, Journal of Optics A: Pure and Applied Optics, 8, 796, 2006.

Reinking, R. F., Snider, J. B., and Coen, J. L.: Influences of storm-embedded orographic gravity waves on cloud liquid water and precipitation, Journal of Applied Meteorology, 39, 733–759, 2000.

Roach, W., Brown, R., Caughey, S., Garland, J., and Readings, C.: The physics of radiation fog: I–a field study, Quarterly Journal of the Royal Meteorological Society, 102, 313–333, 1976.

Roe, G. H.: Orographic precipitation, Annu. Rev. Earth Planet. Sci., 33, 645–671, 2005.

Rogers, D. C. and Vali, G.: Ice crystal production by mountain surfaces, Journal of climate and applied meteorology, 26, 1152–1168, 1987.

Rogers, R. R. and Yau, M. K.: A short course in cloud physics, Pergamon, 1989.

Román-Cascón, C., Steeneveld, G., Yagüe, C., Sastre, M., Arrillaga, J., and Maqueda, G.: Forecasting radiation fog at climatologically contrasting sites: evaluation of statistical methods and WRF, Quarterly Journal of the Royal Meteorological Society, 142, 1048–1063, 2016.

Rose, T., Crewell, S., Löhnert, U., and Simmer, C.: A network suitable microwave radiometer for operational monitoring of the cloudy atmosphere, Atmospheric Research, 75, 183–200, 2005.

Rosenow, A. A., Plummer, D. M., Rauber, R. M., McFarquhar, G. M., Jewett, B. F., and Leon, D.: Vertical velocity and physical structure of generating cells and convection in the comma head region of continental winter cyclones, Journal of the Atmospheric Sciences, 71, 1538–1558, 2014.

Rotunno, R. and Ferretti, R.: Mechanisms of intense Alpine rainfall, Journal of the atmospheric sciences, 58, 1732–1749, 2001.

Rotunno, R. and Houze, R. A.: Lessons on orographic precipitation from the Mesoscale Alpine Programme, Quarterly Journal of the Royal Meteorological Society: A journal of the atmospheric sciences, applied meteorology and physical oceanography, 133, 811–830, 2007.

Saleeby, S. M., Cotton, W. R., Lowenthal, D., Borys, R. D., and Wetzel, M. A.: Influence of cloud condensation nuclei on orographic snowfall, Journal of Applied Meteorology and Climatology, 48, 903–922, 2009.

Saleeby, S. M., Cotton, W. R., and Fuller, J. D.: The cumulative impact of cloud droplet

nucleating aerosols on orographic snowfall in Colorado, Journal of Applied Meteorology and Climatology, 50, 604–625, 2011.

Saleeby, S. M., Cotton, W. R., Lowenthal, D., and Messina, J.: Aerosol impacts on the microphysical growth processes of orographic snowfall, Journal of Applied Meteorology and Climatology, 52, 834–852, 2013.

Sampurno Bruijnzeel, L., Eugster, W., and Burkard, R.: Fog as a hydrologic input, Encyclopedia of hydrological sciences, 2006.

Sassen, K., Mace, G. G., Wang, Z., Poellot, M. R., Sekelsky, S. M., and McIntosh, R. E.: Continental stratus clouds: A case study using coordinated remote sensing and aircraft measurements, Journal of the atmospheric sciences, 56, 2345–2358, 1999.

Scherrer, S. C. and Appenzeller, C.: Fog and low stratus over the Swiss Plateau- a climatological study, International journal of climatology, 34, 678–686, 2014.

Schlenczek, O.: Airborne and Ground-based Holographic Measurement of Hydrometeors in Liquid-phase, Mixed-phase and Ice Clouds, Ph.D. thesis, Universitätsbibliothek Mainz, 2018.

Schlenczek, O., Fugal, J. P., Lloyd, G., Bower, K. N., Choularton, T. W., Flynn, M., Crosier, J., and Borrmann, S.: Microphysical properties of ice crystal precipitation and surface-generated ice crystals in a High Alpine environment in Switzerland, Journal of Applied Meteorology and Climatology, 56, 433–453, 2017.

Schrod, J., Weber, D., Drücke, J., Keleshis, C., Pikridas, M., Ebert, M., Cvetković, B., Nickovic, S., Marinou, E., Baars, H., et al.: Ice nucleating particles over the Eastern Mediterranean measured by unmanned aircraft systems, Atmospheric Chemistry and Physics, 17, 4817, 2017.

Shupe, M. D., Kollias, P., Matrosov, S. Y., and Schneider, T. L.: Deriving mixed-phase cloud properties from Doppler radar spectra, Journal of Atmospheric and Oceanic Technology, 21, 660–670, 2004.

Shupe, M. D., Matrosov, S. Y., and Uttal, T.: Arctic mixed-phase cloud properties derived from surface-based sensors at SHEBA, Journal of the atmospheric sciences, 63, 697–711, 2006.

Siebert, H., Wendisch, M., Conrath, T., Teichmann, U., and Heintzenberg, J.: A new tethered balloon-borne payload for fine-scale observations in the cloudy boundary layer, Boundary-layer meteorology, 106, 461–482, 2003.

Siebert, H., Franke, H., Lehmann, K., Maser, R., Saw, E. W., Schell, D., Shaw, R. A., and Wendisch, M.: Probing finescale dynamics and microphysics of clouds with helicopter-borne measurements, Bulletin of the American Meteorological Society, 87, 1727–1738, 2006.

Sikand, M., Koskulics, J., Stamnes, K., Hamre, B., Stamnes, J., and Lawson, R.: Estimation of mixed-phase cloud optical depth and position using in situ radiation and cloud microphysical measurements obtained from a tethered-balloon platform, Journal of the Atmospheric Sciences, 70, 317–329, 2013.

Smith, R. B.: The influence of mountains on the atmosphere, in: Advances in geophysics, vol. 21, pp. 87–230, Elsevier, 1979.

Smith, R. B.: 100 Years of Progress on Mountain Meteorology Research, Meteorological Monographs, 59, 20–1, 2019.

Spuler, S. M. and Fugal, J.: Design of an in-line, digital holographic imaging system for airborne measurement of clouds, Applied optics, 50, 1405–1412, 2011.

Stark, D., Colle, B. A., and Yuter, S. E.: Observed microphysical evolution for two East Coast winter storms and the associated snow bands, Monthly Weather Review, 141, 2037–2057, 2013.

Steeneveld, G., Ronda, R., and Holtslag, A.: The challenge of forecasting the onset and development of radiation fog using mesoscale atmospheric models, Boundary-Layer Meteorology, 154, 265–289, 2015.

Stoelinga, M. T., Locatelli, J. D., and Woods, C. P.: The occurrence of "irregular" ice particles in stratiform clouds, Journal of the atmospheric sciences, 64, 2740–2750, 2007.

Stoelinga, M. T., Stewart, R. E., Thompson, G., and Thériault, J. M.: Microphysical processes within winter orographic cloud and precipitation systems, in: Mountain Weather Research and Forecasting, pp. 345–408, Springer, 2013.

Stopelli, E., Conen, F., Zimmermann, L., Alewell, C., and Morris, C. E.: Freezing nucleation apparatus puts new slant on study of biological ice nucleators in precipitation, Atmospheric measurement techniques, 7, 129–134, 2014.

Sullivan, S., Hoose, C., and Nenes, A.: Investigating the contribution of secondary ice production to in-cloud ice crystal numbers, Journal of Geophysical Research: Atmospheres, 122, 9391–9412, 2017.

Sun, Z. and Shine, K. P.: Studies of the radiative properties of ice and mixed-phase clouds, Quarterly Journal of the Royal Meteorological Society, 120, 111–137, 1994.

Takahashi, T., Nagao, Y., and Kushiyama, Y.: Possible high ice particle production during graupel–graupel collisions, Journal of the atmospheric sciences, 52, 4523–4527, 1995.

Tan, I., Storelvmo, T., and Zelinka, M. D.: Observational constraints on mixed-phase clouds imply higher climate sensitivity, Science, 352, 224–227, 2016.

Tardif, R.: The impact of vertical resolution in the explicit numerical forecasting of radiation fog: A case study, in: Fog and Boundary Layer Clouds: Fog Visibility and Forecasting, pp. 1221–1240, Springer, 2007.

Thompson, B. J.: Holographic particle sizing techniques, Journal of Physics E: Scientific Instruments, 7, 781, 1974.

Tokay, A., Wolff, D. B., and Petersen, W. A.: Evaluation of the new version of the laser-optical disdrometer, OTT Parsivel2, Journal of Atmospheric and Oceanic Technology, 31, 1276–1288, 2014.

Touloupas, G., Lauber, A., Henneberger, J., Beck, A., Hofmann, T., and Lucchi, A.: A Convolutional Neural Network for Classifying Cloud Particles Recorded by Imaging Probes, Atmos. Meas. Tech. Discuss., pp. 1–32, https://doi.org/10.5194/amt-2019-206, 2019.

Turner, D., Shupe, M., and Zwink, A.: Characteristic atmospheric radiative heating rate profiles in Arctic clouds as observed at Barrow, Alaska, Journal of Applied Meteorology and Climatology, 57, 953–968, 2018.

Ulanowski, Z., Kaye, P. H., Hirst, E., Greenaway, R., Cotton, R. J., Hesse, E., and Collier, C. T.: Incidence of rough and irregular atmospheric ice particles from Small Ice Detector 3 measurements, Atmospheric Chemistry and Physics Discussions, 2013.

Vali, G.: Revisiting the differential freezing nucleus spectra derived from drop-freezing experiments: methods of calculation, applications, and confidence limits, Atmospheric Measure-

ment Techniques, 12, 1219–1231, https://doi.org/10.5194/amt-12-1219-2019, URL https://www.atmos-meas-tech.net/12/1219/2019/, 2019.

van der Linden, R., Fink, A. H., and Redl, R.: Satellite-based climatology of low-level continental clouds in southern West Africa during the summer monsoon season, J. Geophys. Res.: Atmospheres, 120, 1186–1201, 2015.

Vardiman, L.: The generation of secondary ice particles in clouds by crystal–crystal collision, Journal of the Atmospheric Sciences, 35, 2168–2180, 1978.

Verlinde, J., Harrington, J. Y., McFarquhar, G., Yannuzzi, V., Avramov, A., Greenberg, S., Johnson, N., Zhang, G., Poellot, M., Mather, J. H., et al.: The mixed-phase Arctic cloud experiment, Bulletin of the American Meteorological Society, 88, 205–222, 2007.

Walter, B., Huwald, H., Gehring, J., Bühler, Y., and Lehning, M.: Radar measurements of blowing snow off a mountain ridge, The Cryosphere, 14, 1779–1794, https://doi.org/10.5194/tc-14-1779-2020, URL https://tc.copernicus.org/articles/14/1779/2020/, 2020.

Wanner, H. and Furger, M.: The bise—climatology of a regional wind north of the Alps, Meteorology and Atmospheric Physics, 43, 105–115, 1990.

Warren, G., Hahn, J., London, J., Chervin, M., and Jenne, L.: Global distribution of total cloud cover and cloud type amounts over land, 1986.

Warren, S. G., Hahn, C. J., London, J., Chervin, R. M., and Jenne, R. L.: Global distribution of total cloud cover and cloud type amounts over the ocean, Tech. rep., USDOE Office of Energy Research, Washington, DC (USA). Carbon Dioxide Research Div.; National Center for Atmospheric Research, Boulder, CO (USA), 1988.

Wegener, A.: Thermodynamik der atmosphäre, JA Barth, 1911.

Westbrook, C. D. and Illingworth, A. J.: Evidence that ice forms primarily in supercooled liquid clouds at temperatures>- 27° C, Geophysical research letters, 38, 2011.

Yano, J.-I., Phillips, V. T., and Kanawade, V.: Explosive ice multiplication by mechanical break-up in ice–ice collisions: a dynamical system-based study, Quarterly Journal of the Royal Meteorological Society, 142, 867–879, 2016.

Yu, C.-K. and Smull, B. F.: Airborne Doppler observations of a landfalling cold front upstream of steep coastal orography, Monthly Weather Review, 128, 1577–1603, 2000.

Yuter, S. E. and Houze Jr, R. A.: Three-dimensional kinematic and microphysical evolution of Florida cumulonimbus. Part II: Frequency distributions of vertical velocity, reflectivity, and differential reflectivity, Monthly weather review, 123, 1941–1963, 1995.

Yuter, S. E., Kingsmill, D. E., Nance, L. B., and Löffler-Mang, M.: Observations of precipitation size and fall speed characteristics within coexisting rain and wet snow, Journal of Applied Meteorology and Climatology, 45, 1450–1464, 2006.

Zinke, J., Salter, M., Leck, C., Lawler, M. J., Porter, G., Adams, M., Brooks, I., Murray, B., and Zieger, P.: A miniaturised balloon-borne cloud water sampler and its deployment in the high Arctic, 2020.

Acknowledgments

The successful completion of this PhD project would not have been possible without the contribution and support of many people. Specifically, I would like to thank:

- Ulrike Lohmann for providing me the opportunity to work on this unique research project, for giving me the scientific freedom to follow up on my own ideas and for her guidance and enthusiasm throughout this thesis.
- Jan Henneberger for his technical and scientific support, for many fruitful discussions, for all the night shifts during campaign time and for being a great supervisor and motivator throughout this PhD project.
- Susanne Crewell for agreeing to be my external co-examiner and for her constructive feedback.
- Hannes Wydler for his technical support and expertise and in particular for his work on the HOLIMO 3B electronics and software.
- Michael Rösch, Peter Isler and Marco Vecellio for manufacturing parts of HOLIMO 3B and of the HoloBalloon platform, sometimes on very short notice.
- Peter Isler and Hans-Heini Vogel for helping me with my computer related requests and issues and for exchanging my battery three times.
- Eva Choffat for dealing with all the administrative tasks and for maintaining the overview of the campaign receipts.
- The RACLETS team for the organization of the campaign, for technical and scientific support and for great collaborations. In particular, I would like to thank Jan, Annika, Julie, Jörg, Claudia, Alex, Lucie, Bettina and Mario for enjoyable and fun weeks in Davos and for many raclette and fondue nights.
- The staff of the Kieswerk Aarwangen for access to the measurement site, for their technical support during the first field campaign and for their help with the wheel loaders.
- The Federal Office of Civil Aviation and in particular Jeroen Kroese and Judith Baumann for their excellent assistance in getting the flight permit.
- The whole Atmospheric Physics group at IAC for the scientific and moral support, for a very friendly atmosphere and for all the fun activities outside of ETH.

- The HoloSuite community for many valuable discussions and inputs during our meetings.
- Patric Seifert and Johannes Bühl from TROPOS for answering my questions related to remote sensing instrumentation and helping in the interpretation of the data.
- Rob, Alex, Annika, Julie and Jörg for proofreading manuscripts and parts of this thesis, for their scientific input and constructive feedback.
- Annika, Katty and Saskia for having been such great office mates and for having made O 15.1 such a nice working environment.
- Gesa, Monika and Anina for always having an open ear for me, for all the sport sessions at ASVZ and for the nice cooking evenings.
- Annika, Steffen, Ole, Bernat, Kristian, David and Julie for many lively discussions during the lunch and coffee breaks.
- Gesa, Cameron, Steffen and Rob for all hikes and ski trips in the Swiss Alps and many relaxing BBQ-afternoons around the 'smoky-mountain'. Thank you also for introducing me into Skat and for many fun game nights at BQM and Alehouse.
- Fabian, Jan, Kristian, Beni and Iselin and the whole Stolzewiese-group for fun football games on Thursday.
- All my friends and colleagues at IAC for making my PhD a great and memorable time.
- My flatmates Andrina, Laura and Julia and all my friends for many 'cloud-free' hours.
- Rob for supporting and encouraging me over the last years and for all the fun adventures.
- My parents, Daniela and Eliano, and my sister, Selina, for their encouragement and support throughout my way. Thank you for having supported me all these years!